ACTIVE DUST DEVILS ON MARS:

A COMPARISON OF SIX SPACECRAFT LANDING SITES

by

Devin Waller

A Thesis Presented in Partial Fulfillment
of the Requirements for the Degree
Master of Science

Approved April 2011 by the
Graduate Supervisory Committee:

Ronald Greeley, Chair
Philip Christensen
Randall Cerveny

ARIZONA STATE UNIVERSITY

May 2011

ABSTRACT

Dust devils have proven to be commonplace on Mars, although their occurrence is unevenly distributed across the surface. They were imaged or inferred by all six successful landed spacecraft: the Viking 1 and 2 Landers (VL-1 and VL-2), Mars Pathfinder Lander, the Mars Exploration Rovers Spirit and Opportunity, and the Phoenix Mars Lander. Comparisons of dust devil parameters were based on results from optical and meteorological (MET) detection campaigns. Spatial variations were determined based on comparisons of their frequency, morphology, and behavior. The Spirit data spanning three consecutive martian years is used as the basis of comparison because it is the most extensive on this topic. Average diameters were between 8 and 115 m for all observed or detected dust devils. The average horizontal speed for all of the studies was roughly 5 m/s. At each site dust devil densities peaked between 09:00 and 17:00 LTST during the spring and summer seasons supporting insolation-driven convection as the primary formation mechanism. Seasonal number frequency averaged ~1 dust devils/ km^2/sol and spanned a total of three orders of magnitude. Extrapolated number frequencies determined for optical campaigns at the Pathfinder and Spirit sites accounted for temporal and spatial inconsistencies and averaged ~19 dust devils/km^2/sol. Dust fluxes calculated from Pathfinder data ($5x10^{-4}$ kg/m^2/s and $7x10^{-5}$ kg/m^2/s) were well with in the ranges calculated from Spirit data ($4.0x10^{-9}$ to $4.6x10^{-4}$ kg/m^2/s for Season One, $5.2x10^{-7}$ to $6.2x10^{-5}$ kg/m^2/s during Season Two, and $1.5x10^{-7}$ to $1.6x10^{-4}$ kg/m^2/s during Season Three). Based on the results a campaign is written for improvements in dust devil

detection at the Mars Science Laboratory's (MSL) site. Of the four remaining candidate MSL sites, the dusty plains of Gale crater may potentially be the site with the highest probability of dust devil activity.

DEDICATION

I dedicate this accomplishment to my mother, Linda Watts, who has stood by my side every step of this process. Without her love, understanding, endless support, and guidance this journey would have been significantly more difficult. I thank her for leading by example and always reminding me to stay positive. Thanks to her I've remained steadfast in my persistence to finish my graduate degree. I look forward to a very bright future.

ACKNOWLEDGMENTS

It is my pleasure to thank those who made this thesis possible. I owe my deepest gratitude to Ronald Greeley who has served as my professor, advisor, and chairman of my supervisory committee. I thank him for the academic opportunities he has provided, for the guidance and advice that he has given, and for the many discussions we have had that have assisted me throughout this process. I especially thank him for allowing me the opportunity to work in active mission operations as a geology theme lead on the Mars Exploration Rover project. I am grateful to my committee members Phil Christensen and Randy Cervany for their insightful discussions that have helped improve my general understanding of aeolian processes that occur on Mars and Earth. The foundation of this thesis would not have been possible without the hours of discussion had with my colleagues Shane Thompson, Lynn Neakrase and Patrick Whelley. I would also like to thank Charles Bradbury whose technical assistance and advice were invaluable. I would like to acknowledge my fellow Planetary Geology Group members and graduate students for their support and advice throughout this process. Last, but certainly not least, I am grateful for my family and friends who were always there for me during the writing of this thesis.

TABLE OF CONTENTS

Page

LIST OF TABLES

LIST OF FIGURES

CHAPTER 1 INTRODUCTION

1.1 Background

1.1.1 Dust in the Martian Atmosphere

The planetary boundary layer (PBL) is the lower part of the atmosphere that interacts directly with planetary surfaces and is influenced by surface roughness and solar heating. PBL processes on Mars have remained a major topic of speculation for over two centuries since surface changes caused by the movement of dust were mistaken for seasonal changes associated with vegetation growth (Lowell, 1906; Slipher, 1938; Sinton, 1959). It is now understood that albedo and color changes as seen from Earth-based telescopes and from orbit are caused mainly by dust lifted during Mars' warm southern spring and summer seasons; while, water clouds and frost during the cold seasons also cause visible seasonal changes. Aeolian processes are regarded as the primary geological process currently altering the martian surface; however, it is unclear how wind-related activity varies with location. Dust lifted into suspension and lofted through the atmosphere creates the perpetual haze that enshrouds the *Red Planet*. Dust is categorized as a sediment size that travels in suspension and is carried by turbulent air (Bagnold, 1941). These extremely small grains (< 3 μm in diameter on Mars; Pollack et al., 1977, 1979, 1995; Smith et al., 1997; Tomasko et al., 1999; Wolff et al., 2006) have very large surface area-to-mass ratios so the resistance (atmospheric drag) which acts opposite the direction of the particle's motion through the atmosphere is capable of supporting their weight, thereby keeping them aloft for long periods of time. Observations of evolving

martian dust storms have shown that the tiniest grains can remain suspended for over 150 days (Pollack et al., 1979) before settling onto the surface.

Dust plays an important role in altering global circulation patterns on Mars (Haberle et al., 1993). Mars' low-pressure atmosphere (typically ~6-10 mbar) allows for the rapid formation of a midday superadiabatic layer with large near-surface (~100-200 m above the surface) thermal gradients. Superadiabatic lapse rates (> 9.8 K/km) develop as a result of vertical instability in the lower atmosphere and are necessary for the formation of convective wells in the bottom layers of the PBL (Leovy, 1979). Convection under Mars' present atmospheric conditions cannot transport sufficient heat from the surface to higher elevations allowing for stable dry adiabatic conditions (~ 9.8 K/km). These unstable conditions allow intense convection to persist between mid-morning and late afternoon when solar heating of the surface is strongest. Low ambient wind shear limits vertical mixing. Atmospheric CO_2 (~95% of the total composition) is inferior to dust at absorbing incoming visible (400-600 nm) solar radiation. As more dust is entrained, less direct visible light reaches the surface and causes a decrease in surface heating. Atmospheric dust then reradiates the visible radiation back into the PBL at longer thermal infrared (IR) wavelengths, releasing energy in the form of heat. Changes in the thermal gradient associated with radiation from heated dust grains affects PBL convection and can alter Mars' global climate (Kahn et al., 1992).

The entrainment of dust into the atmosphere is a complex process that requires overcoming large interparticle forces (cohesion, static charges, van der

Waals force, etc.) among the dust grains. The physics of setting sediment into motion from rest is highly dependent on grain size and was first described by Bagnold in his observations of windblown sand in the Egyptian deserts (Bagnold, 1941). These principles were later expanded and adapted to describe particle motion on Mars (Iversen et al., 1976; Greeley et al., 1980; Iversen and White, 1982; Greeley and Iversen, 1985; Greeley et al., 2003). Wind shear (or friction) velocity (u_*) is related to the surface shear stress (τ) by:

$$u_* = \sqrt{\frac{\tau}{\rho}} \tag{1.1}$$

where ρ is the density of air. The friction velocity cannot be measured directly in the field but can be derived from wind profiles where wind speed is plotted as a function of elevation. It was found that there is a semi-logarithmic pattern demonstrating an increase in speed with elevation and u_* is the inverse of the slope of the line.

Dust grains tend to collect in small spaces between larger course grains and are typically submerged within the atmospheric laminar sublayer where flow is streamlined. It is subjected to large interparticle forces because of its large surface area-to-mass ratios. It therefore, requires stronger horizontal surface shear to initiate movement compared to larger grains. Threshold velocity curves (Greeley et al., 1980; ***figure 1.1***) produced from past laboratory experiments show that fine sand on Earth (~ 75 μm) and Mars (~115μm) is the easiest particle size to set into motion from PBL winds (Greeley and Iversen, 1985). In laboratory studies, Greeley et al., (1980) found that the minimum wind speed required to

move particles of a given size is roughly ten times larger at low martian-like atmospheric temperatures and pressures (~210 K, 6.5 mbar) than under Earth-like atmospheric conditions (~ 288 K, 1 bar). Under typical martian conditions, as measured by landed spacecraft, horizontal PBL winds are not strong enough to lift dust and therefore, consequent hypotheses were proposed about the possible entrainment mechanisms that were responsible for helping maintain the atmospheric dust haze (Greeley et al., 1977, 1992, 2003; Greeley, 2002).

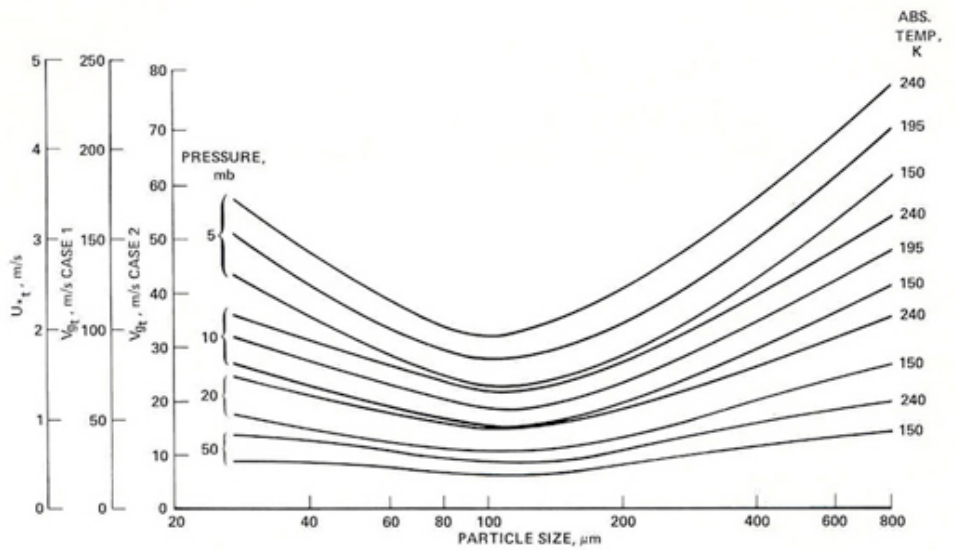

Figure 1.1 Particle threshold curves as a function of particle size for martian surface pressures (5 and 10 mbar) and for representative martian temperatures (150, 195, and 240 K) from laboratory studies by Greeley et al., 1980. CASE1 represents free stream velocity at the top of the PBL for winds blowing over a flat surface of erodible grains; CASE 2 is for a similar surface with cobbles and boulders.

Dust storms make major contributions to the lifting of large amounts of dust and other fine-grained sediment into the martian atmosphere where it can be redistributed, sometimes very long distances from its source (Leovy and Zurek, 1979; Cantor et al., 2002). Local and regional dust storm activity is common during the warm seasons but is strongest and most frequent during late southern spring when Mars is at perihelion (a planet's closest orbital approach to the Sun).

Roughly 78% of the dust storms observed during a 1999 orbital study (Cantor et al., 2001) occurred between late southern winter (L_s 161º; where L_s is the aerocentric longitude of the Sun in degrees where 0º is defined as the Mars' northern spring equinox) and mid southern summer (L_s 326º). *In*cident *sol*ar radi*ation* (insolation) is defined as a measure of solar radiation received on a given surface area in a given amount of time. Increased insolation causes increased turbulence and wind speeds that are capable of lifting sediment from the surface. Planet-encircling dust storms (referred commonly as *global* dust storms) create global obscuration of the surface from suspended dust are relatively infrequent, occurring every 2-3 martian years (Cantor et al, 2001). However, annual observations of martian temperatures and aerosol optical depth (a dimensionless measure of atmospheric dust opacity) indicate that it is impossible to attribute the perpetually hazy atmosphere dust load solely to storm activity. Saltation impact (Greeley, 2002) and strong wind gusts (Sullivan et al., 2008) also contribute to lifting dust, although these local events may be infrequent. Fueled by past predictions, the detection of convective thermal vortices by landed spacecraft (Ryan and Lucich, 1983), and the discovery of active dust devils seen in Viking Orbiter images (Thomas and Gierasch, 1985), the last five decades has seen analyses from optical observations, meteorological detection, and analytical and high-resolution computer modeling. The results have shown that active dust devils are ubiquitous on the martian surface. They are capable of lifting large amounts of dust into suspension, making them significant contributors to the overall martian atmospheric dust load. Thus vortices are an important mechanism

for lifting large amounts of dust even in the absence of strong horizontal wind shear and they help maintain the atmospheric haze when dust storm activity is low.

1.1.2 Formation of Dust Devils on Mars

Atmospheric vortices (spinning masses of fluid) are a common type of aeolian process that forms as a result of convective heating above warm planetary surfaces. Dust devils (central dust-laden columns of convective vortices) are powered by insolation in the presence of atmospheric instability (Sinclair, 1966, 1973; Metzger et al., 1999). The formation of convective vortices and the mechanisms that allow them to entrain dust to become dust devils is important on Earth and Mars (reviewed by Balme and Greeley, 2006). They have proven to be commonplace on Mars, although their occurrence is unevenly distributed across the surface (Cantor et al., 2001, 2006; Whelley and Greeley, 2008). Dust devils are generated in the martian PBL (Ryan, 1964; Gierasch and Goody, 1973) and have been observed over a large range of elevations and latitudes (Cantor et al., 2006). The study of dust devils as a significant dust entrainment mechanism on Mars is important for understanding global feedbacks between climate, atmospheric circulation and dust loading.

A convective vortex is a vertically rotating thermal air column generated by rising air parcels that are heated from contact with the warm midday surface (Sinclair, 1966, 1969, 1973; Ryan and Carroll, 1970; Rennó et al., 1998, Metzger et al., 1999). Insolation is the primary source of energy for the developing vortex, which transfers heat to air parcels that are lifted into the low-pressure core. If PBL

conditions are appropriate for the generation of convective vortices and ample unconsolidated fine-grained sediment is present on the surface over which a vortex passes, then the vortex can become a dust devil. Dust devils are only seen when sediment is lifted into the swirling column but vortices can persist even when loose sediment is unavailable.

The structure of a martian dust devil is similar to its terrestrial counter-part (Metzger, 1999; Balme and Greeley, 2006; ***figure 1.2***). To conserve mass, warm air parcels move radially inward along the surface and then are raised from the surface around the low-pressure core of the vortex (Ryan & Carroll, 1970; Ferri et al., 2003; Greeley et al., 2003). As warm buoyant parcels of air rise to cooler areas, they expand to accommodate decreasing atmospheric pressure. As the air parcels expand, they lose internal energy and their temperature decreases. However, the heat transferred into the column from the relatively warm grains lifted from the surface, further bolsters the dust devil's energy. Local atmospheric eddies generated from turbulent air masses interacting with uneven surface roughness elements and the conservation of angular momentum within the dust devil column induces local vorticity (a tendency for a fluid to "spin"; in fluid dynamics, it is the curl of the fluid velocity) and causes the mass to rotate (Sinclair, 1966; Ryan and Carroll, 1970; Carroll and Ryan, 1970; Rennó et al., 2000). As more air moves inward to fill the void left by the rising parcels, the bulk mass surrounding the rotational axis increases, which further intensifies its vorticity (Rennó et al., 1998) and adds strength to the column.

In a terrestrial study using a meteorological tower to measure winds speeds of a passing dust devil at three heights, Sinclair (1966) found three distinct regions that comprise the dust devil structure. Region 1 ($0 \text{ m} < z < 2 \text{ m}$), the near-surface region, makes up the "vortex boundary layer" and is most concentrated with sediment. Region 2 ($2 \text{ m} < z < 10 \text{ m}$), the main part of the dust devil, is the region with negligible mass transfer between the near-vertical column and the surrounding air. Region 3 ($z > 10 \text{ m}$), the top of the dust devil, is the area where rotation decays and there is a net release of dust into the ambient flow. The three heights that were analyzed were based solely on the restrictions of the equipment and are not necessarily the only divisions in a dust devil (Sinclair, 1966).

Figure 1.2 Dust devils imaged on Earth and Mars. (a) Dust devil imaged in Arizona desert, Earth on 8 June 2005 (image credit: NASA/ U. of Michigan) and (b) dust devil imaged by MER Spirit in plains of Gusev crater, Mars on sol 581 (image credit: NASA/JPL/Cornell).

The sustainability of a dust devil on Earth and Mars favors (1) clear skies for maximum and frequent insolation (2) a calm and arid environment so that cooling and cohesion from moisture are negligible (3) the development of strong near-surface convection (4) local impediments to wind flow as to produce wake eddies and (5) ample unconsolidated sediment on the surface (reviewed by Balme and Greeley, 2006). The detection of convective vortices on Earth and Mars indicates that superadiabatic atmospheric conditions are being generated in the PBL. It also indicates that local eddies are being produced in turbulent winds. The development of dust devils implies that there is ample locally derived, unconsolidated dust to be lifted. Laboratory experiments have shown that vortex threshold is analogous to PBL shear for sand-sized particles at Earth (~1 bar at sea level) pressures, making horizontal velocity one of the primary mechanisms for sand lifting (Greeley et al., 2003). Terrestrial dust devils are inferior to boundary layer winds at lifting and transporting dust (Balme and Greeley, 2006). Dust on

Mars, however, is very difficult to move solely by boundary layer winds. Laboratory studies (Greeley et al., 2003) have shown that the low-pressure core of a dust devil is more influential than boundary layer winds at overcoming interparticle and gravitational forces between dust grains. The low-pressure core of a dust devil relative to the higher-pressure ambient conditions (referred to as the *Δ-P effect*) is thought to create a "vacuum cleaner" effect that lifts grains into the flow (***figure 1.3***).

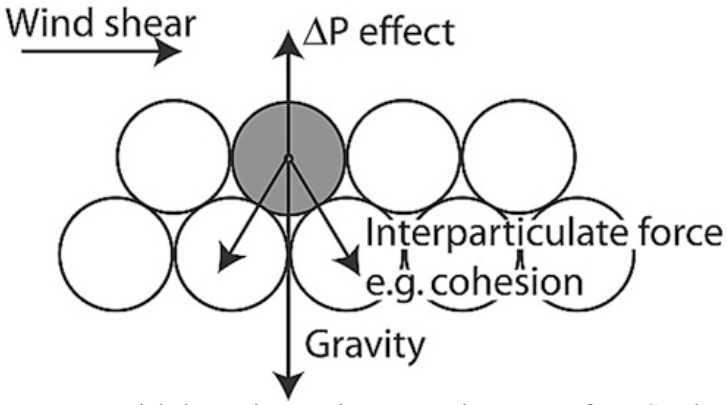

Figure 1.3. Forces on a particle beneath a passing convective vortex; from Greeley et al. 2003.

Vortices are governed by three internal wind components, tangential velocity *U*, radial velocity *V*, and vertical velocity *W* (reviewed by Balme and Greeley, 2006). Past terrestrial studies have shown that the tangential wind component approximates a Rankine vortex model (Faber, 1995) for most dust devils. Horizontal winds increase linearly from zero at the dust devil core to the maximum speed (V_p; peak velocity) at the dust-laden boundary (R_v; radius of the vortex) and then decreases with a $1/r$ relationship (where r is the radial distance out from the core) from the column boundary out to the edge of influence (***figure 1.4***). Sinclair (1973) found that for the terrestrial dust devils the wind speed model is closer to $r^{-1/2}$ than $1/r$ for the portion of the dust devil closest to the surface.

Balme and Greeley (2006) attributed this difference to the nonconservation of angular momentum caused by frictional loses due to contact with the surface. Horizontal speed, made up of the radial and tangential components of internal wind, is given by

$$V_h = (V^2 + U^2)^{1/2}. \quad (1.2)$$

Balme and Greeley (2006) found that vertical flow dominates the center of a typical dust devil, vertical and tangential flow dominate the area within the column, and radial and tangential flow dominate the area outside of the column.

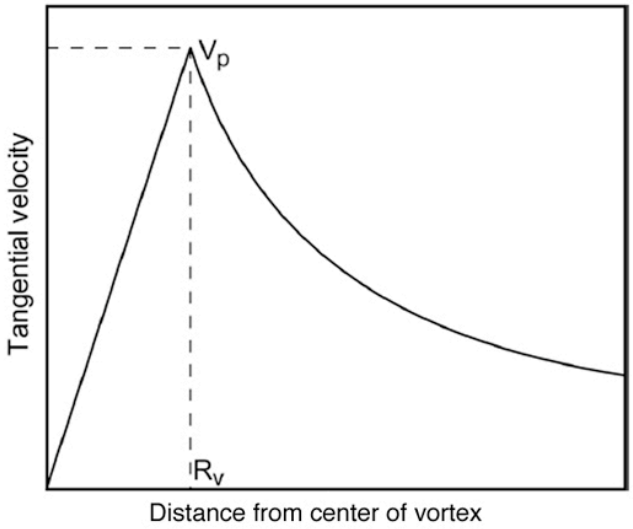

Figure 1.4. Rankine model for the tangential velocity structure of a vortex; the central region of the vortex is in solid rotation and tangential velocity rises as a linear function of radius to a peak (V_p) at the column boundary (R_v); the exterior region of the vortex decreases as the inverse of the distance from the vortex center; from Balme and Greeley, 2006.

1.1.3 Detection of Dust Devils with Landed Spacecraft

In order to make sense of seasonal variations in PBL processes, atmospheric monitoring from the surface needs to be spatially and temporally consistent (Metzger et al., 1999; Rennó et al., 2000). Ideally, a global array of landed MET instruments capable of measuring diurnal variations in temperature,

pressure, the prevailing wind vector, and the depth of the PBL are necessary to fully describe near-surface atmospheric conditions. The internal wind components (tangential, radial, and vertical winds) can be measured for each passing vortex depending on sensor capability. Simultaneous optical imaging would provide a means to put into context MET sensor data and to provide ground truth. Even though global atmospheric measurements are currently unavailable, landed spacecraft have provided a means to make inferences about local atmospheric thermal instability and near-surface convection. Despite resource limitations and degradation of landed spacecraft, dust devils were imaged by optical cameras or inferred from MET instruments at all six successful Mars landing sites: Viking 1 and 2 (VL-1 and VL-2); Mars Pathfinder; Mars Exploration Rovers *Spirit* and *Opportunity*; and the Phoenix Mars Lander sites; ***figure 1.5***. These data provide a unique opportunity to compare dust devils at six distinct latitudes in terms of size, speed, frequency, dust flux, and dust loading. These comparisons will provide information about the unstable and turbulent nature of each landing site and the amount of dust that is being lifted due solely to dust devil activity. Direct comparisons among the landed spacecraft are difficult because of differences in seasonal patterns at each location, instrument type, resolution, and sampling rate. Therefore, spatial and temporal normalization was necessary for comparisons to be made among data sets.

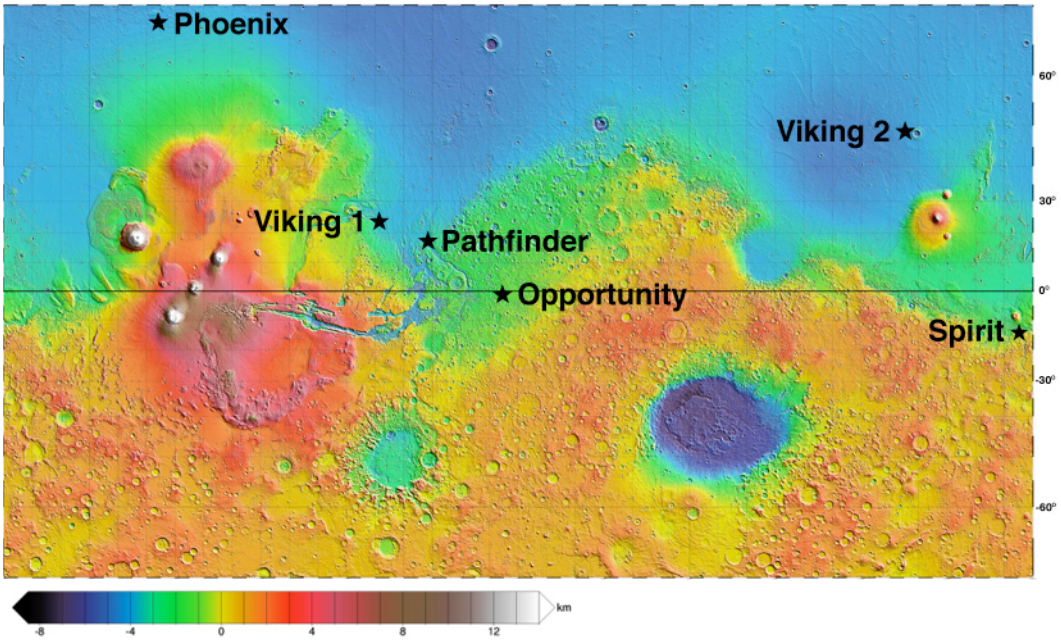

Figure 1.5 Colorized MOLA elevation map showing approximate locations of spacecraft landing sites.

Hundreds of active dust devils have been imaged by landed and orbiting spacecraft (Thomas and Gierasch, 1985; Metzger et al., 1999; Ferri et al., 2003; Ellehoj et al., 2010; Fisher et al., 2005; Cantor et al., 2006; Greeley et al., 2006, 2010; Stanzel et al., 2006, 2008; Towner, 2009). When multiple images are taken within a short amount of time from the surface, changes in dust devil morphology, vertical speeds of dust within the column, and the horizontal speed at which the vortex is moved by ambient winds can be estimated, allowing dust fluxes and loading to be calculated. Orbital analysis of active dust devils and tracks created as dust devils remove surface dust has been used to infer their frequency, size and shape (Greeley et al., 2004; Fisher et al., 2005; Drake et al., 2006; Cantor et al., 2006; Verba et al., 2010). Since their discovery in Viking Orbiter (VO) images (Thomas and Gierasch, 1985), tens of thousands of dust devils have been imaged by orbiting cameras (Fisher et al., 2005; Drake et al., 2006; Cantor et al., 2006;

Stanzel et al., 2006, 2008; Towner, 2009). Due to limitations in spatial resolution, dust devils imaged from orbit were biased towards the largest sizes. Past studies of the global distribution of tracks and assumptions on the amount of dust removed to form a visible track indicate that dust devils can entrain nearly half the amount of dust as lifted during dust storms (Whelley and Greeley, 2008). However, it is not well understood why only some dust devils leave a track in their wake. Results from orbital analyses of active dust devils estimate that only 14% of them leave tracks, likely due to the track not having sufficient contrast to the adjacent terrain (Cantor et al., 2006; Whelley and Greeley, 2008). Also, it is unclear whether the width of the dust devil track represents the visible diameter of the dusty column or is representative of the larger area of disturbance. Orbital observations of dust devils and track surveys are important to gauge the spatial and temporal extent of their activity. However, spacecraft orbital trajectories inhibit frequent monitoring of any single area other than at the poles. Therefore, this study focused solely on comparing active dust devils detected or imaged from the surface due to more frequent and consistent sampling.

The majority of terrestrial and martian pressure, temperature and wind measurements have been made in situ because of the insufficient resolution of remote sensing techniques. Typical temperature and pressure perturbation measured within terrestrial dust devils are 4 to 8 K and 2.0 to 7.0 mbar (Sinclair, 1964, 1973). Dust-laden vortices are inferred from sudden atmospheric pressure drops accompanied by temperature increases and changes in the local wind vector by MET instruments onboard landed spacecraft (Ryan and Lucich, 1983; Murphy

and Nelli, 2002; Ringrose et al., 2003; Ferri et al., 2003; Ellehoj et al., 2010; ***figure 1.6***). When passing vortices move across landed MET instruments with lateral speeds that exceed threshold (~25-30 m/s; Greeley and Iversen, 1985) predicted to lift fine sand (the easiest grain size moved by horizontal winds) from the surface, they have been inferred to be dust laden. However, without simultaneous optical imaging, it is unknown whether the tangential component of wind within a vortex plays a significant role in initiating dust movement. Therefore, the true number of dust-laden vortices from MET studies remains unknown.

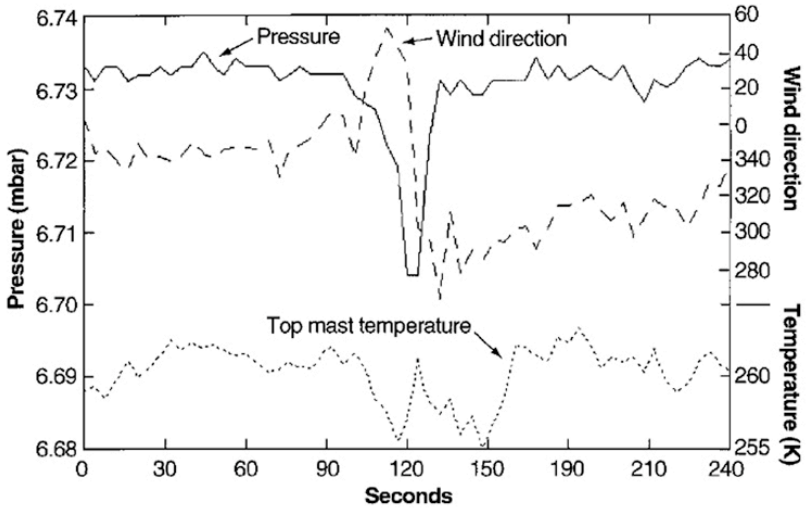

Figure 1.6. Best documented vortex detected MET instruments on Sol 25 of the Pathfinder mission at 1415 LST showing an abrupt pressure drop due to core passage, and a simultaneous 360º wind rotation and embedded temperature increase; from Schofield et al. (1997).

1.2 Objective of Study

The objective of this research is to compare dust devils at the six sites in order to determine spatial variations in frequency, morphology and behavior. Spirit's data are used as the basis of comparison because they are the most extensive compilation on this topic, spanning three consecutive martian years of

analysis (Greeley et al., 2006, 2010). A dust devil *season* is defined as the period when the frequency of activity was large and continuous (Greeley et al., 2010). At the Spirit site, dust devil seasons were periods when dust devils were active for consecutive days without breaks in activity. Inter- and intra-seasonal variations in the Spirit data were investigated prior to making comparisons to the dust devils detected at the other five sites. For each of the landing sites different methods of detecting dust devil activity were used. All results were therefore spatially and temporally normalized, similar to the methods used in the Greeley et al. (2006, 2010) papers before direct comparisons to the Spirit data were made. Dust devil sizes, speeds, frequency, and dust fluxes at the six landing sites are compared when the listed parameter is available. Finally, potential dust devil activity at the four remaining candidate landing sites for the 2011 Mars Science Laboratory (MSL) is discussed and ideas for an effective, future dust devil detection campaign are outlined.

CHAPTER 2 LANDING SITE OVERVIEW

2.1 Chapter Overview

In order to compare dust devil parameters measured and derived at each of the six landing sites (***figure 1.5***) it is important to outline each detection campaign and the methods by which the data collected were processed and synthesized. This chapter outlines the instruments used by each of the six spacecraft in dust devil and vortex detection. Then, each mission is described in terms of general objectives, landing site morphology, climate predictions and/or observed weather conditions during the period corresponding to each dust devil study, and a description of the detection campaigns carried out for each site. The six spacecraft are described in order by landing date (***table 2.1***).

	Dates of Operation	Sols in Operation	Site Location	Site Coordinates
Viking 1	20 July 1976 - 13 November 1982	2245	Chryse Planitia	(310.03ºE, 22.48ºN, -3623m)
Viking 2	3 September 1976 - 11 April 1980	1281	Utopia Planitia	(134.01ºE, 48.27ºN, -4509m)
Pathfinder	4 July 1997 - 27 September 1997	83	Ares Vallis	(326.45ºE, 19.33ºN,-3695m)
Spirit	4 January 2004 - present	active	Gusev Crater	(175.47ºE, 14.57ºS,-1942m)
Opportunity	25 January 2004 - present	active	Meridiani Planum	(354.47ºE, 1.95ºS, -1369m)
Phoenix	25 May 2008 - 2 November 2008	152	Martian Arctic	(234.25ºE, 68.22ºN, -4124m)

Table 2.1. Dates and number of sols (martian days) in operation, site location, and coordinates of landed Martian spacecraft; The last communication with Spirit was on 22 March 2010 but continuing efforts to elicit a response from the rover are still underway before NASA's Jet Propulsion Laboratory will switch to single rover operations.

2.2 Instruments Used in Dust Devil and Vortex Detection

Each spacecraft was equipped with a unique instrument payload suited to meet individual mission goal requirements. ***Tables 2.2*** and ***2.3*** list the optical camera systems and MET instruments used in aeolian campaigns to image dust devils and detect vortices along with the number of features reported at each site. The term *vortex* will refer to dust devils that were only detected by MET sensors

because without simultaneous optical imaging there is no way to determine if they were dust-laden. Dust devils are imaged in optical camera systems and are most easily resolved using frame enhancement and subtraction techniques. Dust devils are most easily imaged against the horizon because concentrated dust within the column appears darker than the brighter less concentrated atmospheric dust and brighter against the darker substrate below the horizon (Metzger et al., 1999). Image subtraction and contrast enhancement techniques work best to resolve faint dust devils. Convective vortices are identified by abrupt pressure drops as their low-pressure cores move across stationary MET sensors (Sinclair, 1973). Abrupt increases in temperature and wind speed and an 180º shift in wind direction are also indications that a vortex has passed over MET sensors. Small-scale temperature and wind vector fluctuations occur naturally in turbulent PBL environments in the absence of vortices and do not always accompany vortex-induced pressure drops, making it more difficult to identify vortex activity based solely on these detections. To confirm the presence of a dust devil from MET data, optical imaging is necessary to verify that dust has been lifted into the vortex column. However, some MET studies made inferences about the passage of dust-laden vortices from the tangential speeds at which vortices over the sensors. As stated in Chapter One, this assumption does not take into account the Δ-P effect of the vortex's low-pressure core, only tangential speeds as a necessary entrainment mechanism to overcome interparticle forces and gravity.

Table 2.2

Optical Instruments Used in Dust Devil Detection and Number of Dust Devils Observed at Each Site

	Total dust devils (#)	Detector(s)	Height above surface (m)	Camera Type	Stereo Baseline (m)	Field of View (FOV)	Angular Resolution at center of FOV	Spatial Resolution at 100-m distance (cm/pix)
Viking 1	0[a]	VL Camera [e]	1.3	Facsimile	0.80	2.5º (horizontal) x 10º (vertical)	0.70 mrad/pix high-resolution monochrome 2.1 mrad/pix low-resolution color/near IR	7.0/20
Viking 2	0[a]	VL Camera [e]	1.3	Facsimile	0.80	2.5º (horizontal) x 10º (vertical)	0.70 mrad/pix high-resolution monochrome 2.1 mrad/pix low-resolution color/near-IR	7.0/20
Pathfinder	14[b]	Imager for Mars Pathfinder [f]	1.75	512x512 CCD	0.15	14.4º (horizontal) x 14.0º (vertical)	0.98 mrad/pix	9.8
Spirit	706[c]	Pancam [g]	1.54	1024x1024 CCD	0.30	16º x 16º	0.28 mrad/pix	2.8
		Navcam [h]	1.54	1024x1024 CCD	0.20	45º x 45º	0.82 mrad/pix	8.2
		Front/Rear Hazcam [h]	0.52/0.51	1024x1024 CCD	0.10	124º x 124º	2.1 mrad/pix	21
Opportunity	1	Pancam [g]	1.54	1024x1024 CCD	0.30	16º x 16º	0.28 mrad/pix	2.8
Phoenix	76[d]	Surface Stereo Imager [j]	1.84	1024x1024 CCD	0.15	14º x 14º	0.24 mrad/pix	2.4

[a] Ryan and Lucich, 1983
[b] Metzger et al., 1999; Ferri et al., 2003
[c] Greeley et al., 2006, 2010
[d] Ellehoj et al., 2010
[e] Huck et al., 1975; Patterson et al., 1977
[f] Smith et al., 1997
[g] Bell et al., 2003
[h] Maki et al., 2003
[j] Lemmon et al., 2008

Table 2.3

MET Instruments Used in Vortex Detection and Number of Vortices Detected at Each Site

	Total vortices (#)	Experiment	Detectors	Height above surface (m)	Sampling Rate
			Pressure Sensor	0.81	
		Viking Meteorology [e]	Temperature Sensor	1.6	Pressure sampled once every 17 min; Temperature and wind vector
Viking 1	40[a]	Instrument System	Wind Sensors	1.6	sampling ranged between 1.2-112 sec, with most measurements
			Pressure Sensor	0.81	between 32-64 sec
		Viking Meteorology [e]	Temperature Sensor	1.6	
Viking 2	116[a,b]	Instrument System	Wind Sensors	1.6	
					Pressure, temperature and winds sampled in 51 equally spaced MET
			Pressure Sensor	0.10	sessions lasting 3 mins at 4-sec intervals with interspersed 15-min and
		Atmospheric Structure/ [f]	Temperature Sensors	0.25, 0.50, 1.00 *	1 hour sessions of 1-sec sampling; five 24-hour MET sessions at 4-sec
Pathfinder	79[c]	Meteorology Experiment	Wind Sensor	1.1	intervals; Wind socks were imaged by IMP for 100-sec duration, in 12
			Wind socks	0.33, 0.62, 0.92 *	images, run 1-4 times a sol
Spirit		n/a			
Opportunity		n/a			
			Pressure Sensor	1.0	Pressure and temperature sampled every 2 sec; Telltale was imaged in
			Temperature Sensors	0.25, 0.50, 1.00 **	3-100 SSI frames with intervals down to 50 sec; Lidar pulsed at rate of
		Meteorology [g]	Telltale wind assembly	0.75 **	100 Hz and acquired profiles in 20.48 sec, operated 3 times a sol btw 15
Phoenix	502[d]	Experiment	Lidar	1.0	min and 1 hour

[a] Ryan and Lucich, 1983
[b] Ringrose et al., 2003
[c] Murphy and Nelli, 2002; Ferri et al., 2003
[d] Ellehoj et al., 2010
[e] Chamberlain et al., 1976
[f] Seiff et al., 1997
[g] Taylor et al., 2008; Gunnlaugsson et al., 2008; Whiteway et al., 2008

* height above solar panel (1 meter above surface)
** height above lander petal (~5 cm thick)

Viking Lander Instruments

VL-1 and VL-2 were equipped with a pair of facsimile cameras (100 mm resolution) each with an array of 12 silicon photodiodes and six spectral bands (ranging from 0.4-1.0 μm) for color and near-infrared (IR) imaging (Huck et al., 1975). At a height of 1.3 m above the surface, and assuming a spherical Mars, the VL cameras were capable of imaging the horizon 3.0 km away (Binder et al., 1977). Hundreds of thousands of low- and high-resolution black and white, color and IR images were taken of the surrounding terrain, but no dust devils were resolved in any optical frames (Ryan and Lucich, 1983). Poor camera resolution and sparse temporal sampling are a likely reason why no dust devils were imaged at either site.

Hundreds of vortices were, however, detected with the landers' temperature and wind vector sensors. Diurnal patterns of wind, temperature and pressure were recorded by both landers with the Viking Meteorology Instrument System (VMIS) (Chamberlain et al., 1976; ***figure 2.1***). An ambient pressure sensor (stressed-diaphragm variable reluctance transducer) mounted underneath the VL deck (0.81 m above the surface) provided consistent measurements at both landing sites; however, pressure was sampled at a rate too slow (roughly once every 17 minutes; Ryan and Lucich, 1983) to detect the rapid passage of a vortex's low-pressure core and was not used in dust devil studies. The ambient temperature sensor consisted of a three Chromel-Constantan thermocouples mounted 1.6 m above the surface on the end of the Meteorology Sensor Assembly mast (MSA). They were capable of measuring the entire range of predicted

martian temperatures with an accuracy of 1.5ºC (Hess et al., 1977). Fluctuations in the ambient wind vector were recorded with a pair of mast-mounted hot film anemometers mounted orthogonally and maintained at 100ºC above the ambient gas temperature as measured by a reference temperature sensor. The wind sensors measured the total wind speed (tangential, radial and vertical components) and true horizontal flow could not be separated (Ryan and Lucich, 1983) for independent analysis. Accuracies of 10% were determined for wind speeds in the range 2-150 m/s, but were shown to degrade for very light winds (Hess et al., 1977). A quadrant sensor provided an independent wind direction measurement orthogonal to the pair of anemometers. It consisted of a heated cylinder surrounded by four thermocouple junctions at equal angles and identified the quadrant from which the wind was blowing within an accuracy of about 10º. All vortices detected at the VL landing sites were inferred from abrupt increases in the ambient temperature and wind speed and a 360º rotation in wind direction (Ryan and Lucich, 1983; Ringrose et al., 2003). Wind and temperature measurements were sampled night and day in intervals ranging between 1.2 and 112 seconds (Chamberlain et al., 1976; Ryan and Lucich, 1983) with most measurements sampled every 32 and 64 seconds during the daytime hours (1000-1700 LST) when dust devils are most active.

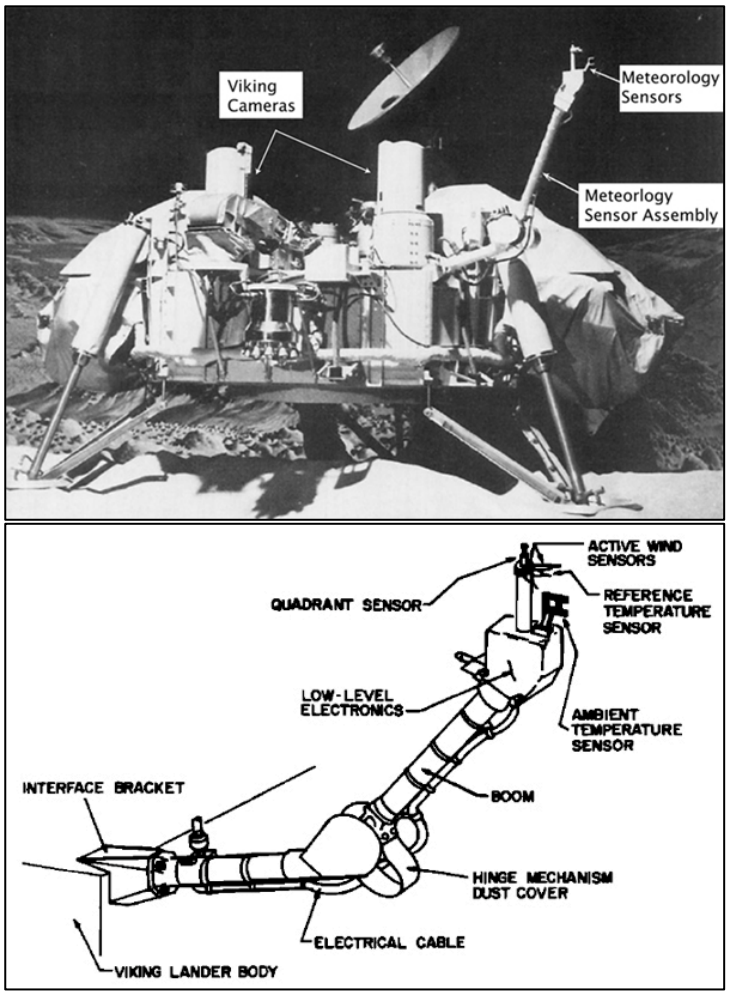

Figure 2.1. (Top) Schematic of Viking Lander showing location of Viking cameras, MET mast, and MET instruments; (Bottom) diagram of Meteorology Sensor Assembly and locations of temperature and wind sensors; both from Chamberlain et al., 1976.

It must be noted that although the instruments performed very well, there were two anomalies that affected the VL MET data early in the mission (Hess et al., 1977). First, on sol 45 of the VL-1 mission the quadrant heater experienced erratic behavior and was no longer producing accurate wind direction readings. Due to partial instrument failures, most of the wind data from VL-1 could not be used. Second, on sol 25 of the VL-2 mission the ambient temperature sensor exhibited a temperature-dependent error. A correction was applied, however the

reference temperature sensor was used to measure the ambient temperature throughout most of the primary mission.

Mars Pathfinder Lander Instruments

Pathfinder provided the first images of dust devils from the surface (Metzger et al., 1999) in frames taken with the Imager for Mars Pathfinder (IMP). The IMP was a mast-mounted, multispectral (440 to 1000 nm), stereoscopic camera that utilized the first CCD on the surface of Mars (Smith et al., 1997; ***figure 2.2***), deriving its heritage from the descent imager/spectral radiometer (Tomasko et al., 1996) that operated on the Cassini Mission's Huygens Probe. From its vantage point 1.75 m above the surface, the horizon was calculated to be roughly 3.4 km away at 3.4 m/pixel resolution (Smith et al., 1997). The IMP served many purposes during the 83-sol mission; it provided high resolution images of the surrounding terrain in a range of wavelengths from visible to near IR, provided spectral contrast of surface features to determine the mineralogy, determined the atmospheric aerosol optical depth, measured the abundance of water vapor, monitored activities of the Sojourner rover, and imaged the windsock experiment. The IMP windsock experiment allowed measurements to be made of near-surface wind speeds as a function of height from the ground based on the deflection angle from vertical and the azimuth of windsocks (Sullivan et al., 2000). Analysis of the windsocks mounted at 33.1, 62.4, and 91.6 cm above the solar petal allowed for the first time near-surface wind profiles to be measured on Mars from which the aerodynamic roughness length and wind friction speeds were determined.

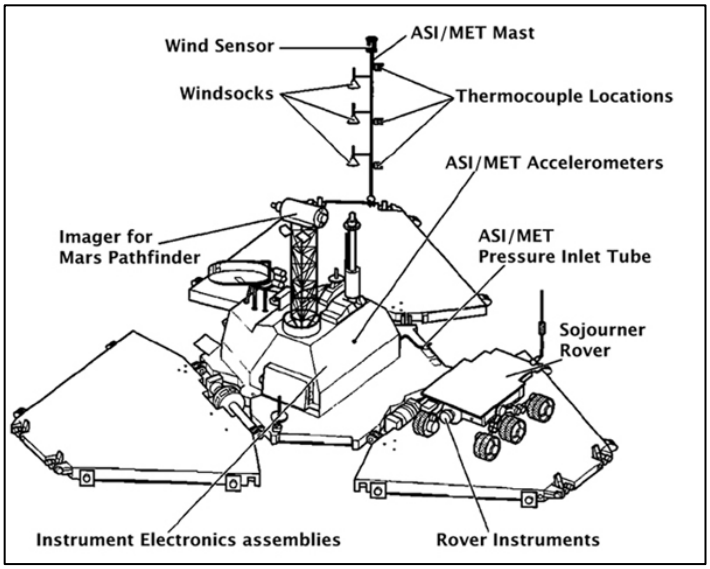

Figure 2.2. The Pathfinder Lander as it was deployed on Mars with locations of MET instruments and optical camera; from Seiff et al., 1977.

The Pathfinder atmospheric structure investigation/meteorology (ASI/MET) experiment measured vertical atmospheric density, ambient pressure and temperature, and the ambient wind vector (Seiff et al., 1997; ***figure 2.2***). The pressure sensor was similar to that used on the VL, a deflecting diaphragm variable reluctance transducer, but with a sensitivity 100 times greater (Hess et al., 1977; Seiff et al., 1997). Ambient pressure measurements were made through a 1-m inlet tube mounted on the lander petal within 10 cm on the ground. With a sampling rate averaging a few seconds, pressure data was primarily used to detect passing vortices that passed over the Pathfinder lander (Murphy and Nelli, 2002; Ferri et al., 2003). The design of the temperature sensors on Pathfinder were also similar to those used on the Viking Landers, however, unlike the single thermocouple mounted on the VL MSA mast, three Chromel-Constantan thermocouples were mounted at three different locations (0.25, 0.50, and 1.00 m above the lander petal which was ~ 5 cm thick) on the Pathfinder MET mast

(Seiff et al., 1997). Wind speed and direction were measured by multiple hot-wire anemometers mounted at a single location 1.2 m above the ground. They were capable of measuring wind speed to within ~1 m/s at low speeds and within ~4 m/s for speeds over 20 m/s. During the 30-sol primary mission phase, 51 equally spaced MET sessions were made to analyze diurnal fluctuations. All MET sensors were measured at the same frequency. Sessions lasted 3 minutes and each instrument sampled the atmosphere at 4-second intervals. PBL variations were measured with interspersed sessions lasting 15 minutes to an hour with 1 second sampling. After the primary mission ended MET sampling was mainly performed during the daylight hours. Five sols (25, 32, 38, 55, and 68), referred to a the Presidential MET Sessions, were devoted to collecting MET data continuously for a complete sol at 4 second intervals.

Mars Exploration Rovers Instruments

To conserve total spacecraft mass and mission cost, neither MER Athena payload was equipped with MET instruments capable of directly measuring the ambient wind vector and atmospheric pressure (Squyres et al., 2003). PBL temperature profiles were measured throughout the MER mission with the rovers' miniature Thermal Emission Spectrometers (Mini-TES; Christensen et al., 2003). Mini-TES thermal IR sensors are located in the rover's Warm Electronics Box (WEB) and view the terrain through an internal telescope that transfers information reflected onto a set of mirrors mounted at the top the Pancam Mast Assembly (PMA; 1.54 m above the surface). Mini-TES collected high-resolution (10 cm^{-1}) spectra over the wavelengths 5-29.5 μm and recorded subtle

temperature perturbations caused by the convective and turbulent near-surface (up to 2 km from the surface) environment. But due to risk of aerosol contamination to the spectrometer the Mini-TES shroud was closed during very windy, dusty periods causing measurements of thermal profiles to be inconsistent during the warm spring and summer seasons when dust devils were most active (Smith et al., 2006). Mini-TES atmospheric integration average roughly 7 minutes making it improbable that Mini-TES was pointed in the direction of a passing dust devil while it took measurements. To date, no thermal measurements of active dust devils have been made with either MER Mini-TES.

Dust devils at the MER Spirit and Opportunity sites were resolved in optical images using frame subtraction and contrast enhancement techniques to enhance fine detail (Greeley et al., 2006, 2010). Four optical cameras were used in detection (***figure 2.3***): the Panoramic camera (Pancam; Bell et al., 2003), Navigation camera (Navcam; Maki et al., 2003), and the Front and Rear Hazard Avoidance cameras (Hazcams; Maki et al., 2003). Pancam consists of a pair of PMA-mounted, multispectral, stereoscopic science cameras used to image the surface terrain in high resolution (0.28 mrad/pix) and in color. It also monitored the atmospheric aerosol optical depth from direct imaging of the Sun and sky multiple times a sol. The Pancam has three times the spatial resolution compared to the Pathfinder IMP and VL cameras. Navcam is a PMA-mounted, monochromatic, engineering stereo pair used primarily to support the operation of MER by providing images that aid in traverse planning and pointing for the Pancam and Mini-TES. The Front and Rear Hazcams are two pair of forward- and

aft-facing body-mounted engineering cameras. They provide protection from navigation hazards that are hidden by the solar panels from Navcam view and aid in positioning of the Instrument Deployment Device (IDD) onto targets of interest for more detailed examination.

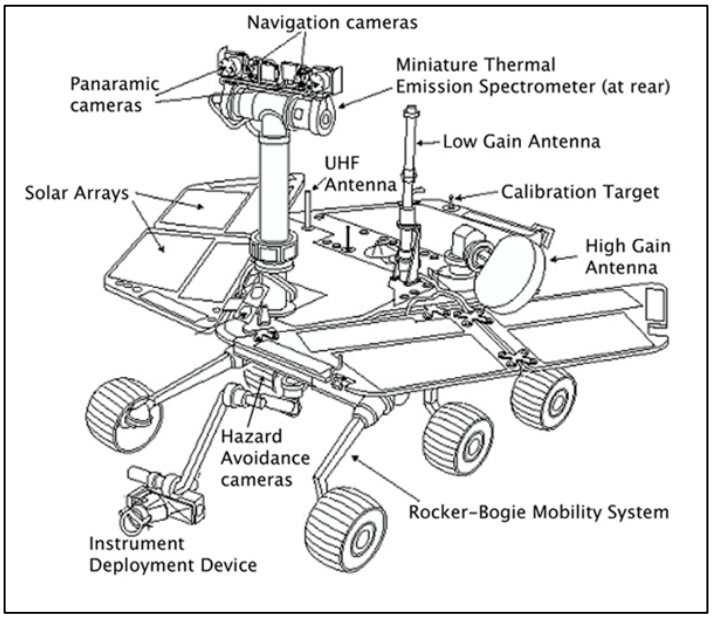

Figure 2.3. Schematic of a Mars Exploration Rover showing the locations of the optical cameras and other instruments; from Squyres et al., 2003.

Phoenix Mars Lander Instruments

Dust devil and vortex detection campaigns during the Phoenix mission were carried out using the Surface Stereo Imager (SSI), the lander's primary imaging system, and the MET weather station (***figure 2.4***). The SSI is a mast-mounted, multispectral, stereo pair used to image the landing site terrain in high-resolution and in color (Lemmon et al., 2008) and supported a large variety of scientific investigations. The Phoenix SSI was mechanically similar to the Pathfinder IMP (Smith et al., 1997) and the failed Mars Polar Lander's SSI (Smith et al., 2001) and supported calibration similar to the IMP and MER

Pancam (Bell et al., 2003). The images of the surrounding terrain were primarily used to generate digital terrain maps that were used to guide the placement of the lander's Robotic Arm (RA) for accurate sampling. The SSI aided in atmospheric studies by measuring the optical depth through frequent solar and sky imaging, observing blowing dust and passing clouds, and by monitoring the movement of the mast-mounted Telltale, a passive wind sensor, mounted at the top of the 1-m MET mast to document local wind conditions (Lemmon et al., 2008; Gunnlaugsson et al., 2008; Smith et al., 2008; Moores et al., 2010).

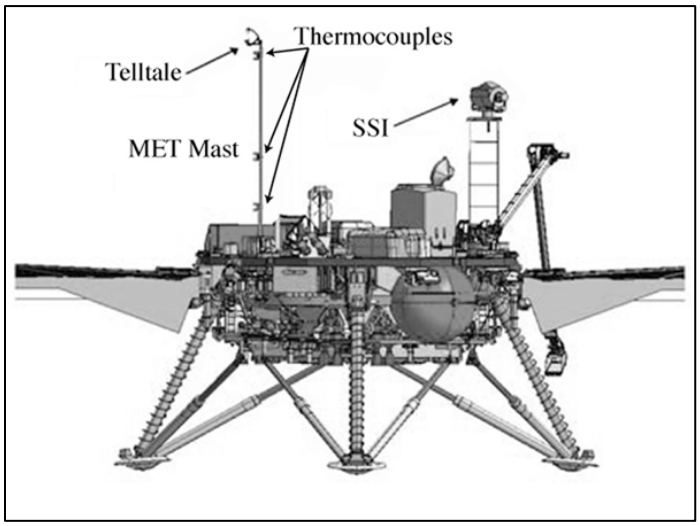

Figure 2.4. Schematic of the Phoenix Lander showing locations of Telltale, Thermocouples, and SSI; from Holstein-Rathlou et al., 2010.

The Phoenix MET package included instruments capable of measuring the ambient temperature, pressure, wind vector, and atmospheric optical depth (Gunnlaugsoon et al., 2008; Whiteway et al., 2008; Taylor et al., 2008; Smith et al., 2008). The temperature sensors consist of three Constantan-Chromel fine-wire thermocouples mounted 0.25, 0.5 and 1.0 m on the top of the lander solar panel (located ~1 m above the surface). Pressure is detected via a silicon diaphragm sensor with a sampling rate of a few seconds, capable of detecting pressure drops

from passing vortices. Due to limitations in total mission budget and mass constraints, Phoenix was not equipped with a hot film anemometer (Taylor et al., 2008) unlike the Pathfinder and VL MET packages. Late in the mission-planning phase, the decision was made to include the Telltale, a mechanical wind indicator that required no direct power or data transmission facilities to operate. Unlike the Pathfinder wind sock experiment that was designed to evaluate surface roughness and wind friction speeds (Sullivan et al., 2000), the Phoenix Telltale was incorporated into the payload primarily to monitor the direction and speed of ambient winds 2 meters above the surface (Gunnlaugsson et al., 2008). To measure wind direction and magnitude, observable deflections in horizontal winds were animated with the Telltale wind assembly and imaged with the SSI. It was designed so that low energy winds deflected the Telltale in the wind direction proportional to the magnitude of the horizontal wind component. At higher wind speeds the Telltale would oscillate until winds exceed 10 m/s where it reached its maximum deflection angle and lose its wind speed/deflection correlation.

2.3 Landing Sites

2.3.1 Viking Lander 1

The Mars Viking Mission involved four spacecraft, consisting of a pair of orbiters (VO-1 and VO-2) and a pair of landers (VL-1 and VL-2). Primary mission goals for VL-1 and VL-2 included characterizing the structure and composition of the atmosphere and surface terrain surrounding the landers and searching for evidence of past and present organic biology. VL-1 and VL-2 performed the first successful soft landing on the martian surface in July and

September 1976 respectively and confirmed the feasibility of using a parachute and retrorockets to slow the spacecraft down in the thin atmosphere (~6 mbar) during EDL. Because VL-1 and VL-2 were powered by radioisotopic thermoelectric generators (RTGs), which create electricity from heat given off by the natural decay of plutonium, they were operational during the day and night.

VL-1 landed in southwest Chryse Planitia (Thomas Mutch Memorial Station; 22.48ºN, 310.03ºE; ***figure 2.5***) in the martian subtropics on 20 July 1976 in the early northern martian summer (L_s 98º). Early in Chryse Planitia's evolution, flood basalts are thought to have filled the low-lying basin followed by subsequent cooling and erosion (Binder et al., 1977; Greeley et al., 1977). Dominant features at the landing site were ridges and troughs and orbiter analysis indicates that VL-1 landed on a wrinkle ridge (Binder et al., 1977) that was chemically and mechanically eroded. The flat volcanic plains have been affected by past fluvial erosion (Greeley et al., 1977) theorized to have occurred at a time when the climate may have been hotter and wetter, and have subsequently been filled by channel deposits (Binder et al., 1977). The VL-1 landing (***figure 2.6***) site was characterized by a regular distribution of angular volcanic rocks (centimeter-to-meter in size), many pitted from aeolian erosion, exposed bedrock, and abundant drifts of fine-grained wind-blown sediment (Binder et al., 1977; Moore et al., 1977). There was a lack of sand-sized sediment in the vicinity of the lander but the terrain showed abundant finer-grained sediment (<100 μm) (Moore et al., 1977).

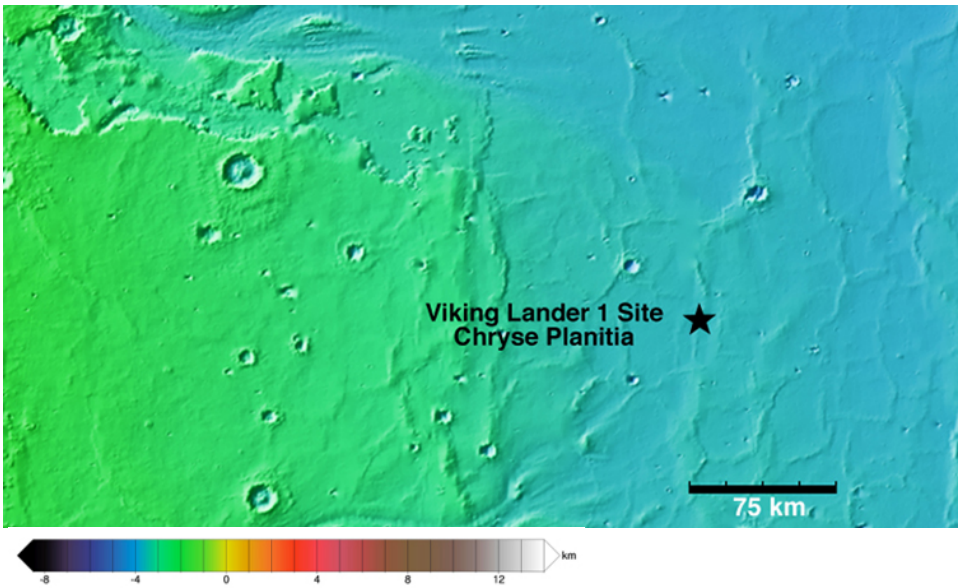

Figure 2.5. Colorized MRO Mars Orbiter Laser Altimeter elevation map showing location of Viking Lander 1 in Chryse Planitia

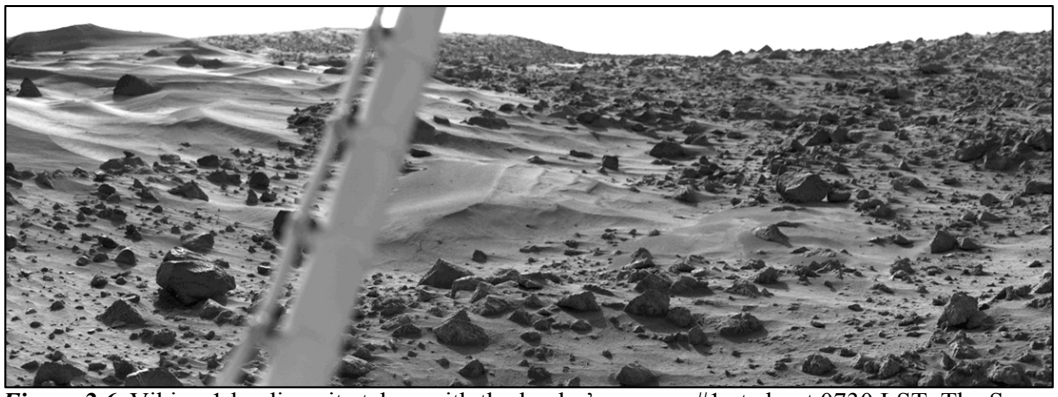

Figure 2.6. Viking 1 landing site taken with the lander's camera #1 at about 0730 LST. The Sun rose two hours earlier and is located about 30º above the horizon in the center of the image. The MET mast cuts across the left side of the image. Image credit: NASA/JPL PIA00393

Reconstructed near-surface wind data extracted from the partially failed VL-1 wind sensor indicated that diurnal wind patterns during the northern summer season were controlled by thermal effects induced by regional topography with little influence from global circulation (Murphy et al., 1990). The lander was positioned near the center of the Chryse Planitia basin, a structure roughly 300 km in diameter and 3 km at its deepest. Drainage winds tended to move downslope during the coldest times of the sol just before dawn and upslope

during the warmest times of the sol corresponding to the period of peak insolation and turbulence. Midday winds at the VL-1 site displayed a pattern of 360º counterclockwise rotation each sol with infrequent periods of clockwise rotation (Hess et al., 1977). Nighttime winds were light, generally less than 2 m/s. Wind speeds increased throughout the morning, reaching a maximum at about 1100 LST. During the summer season suspended dust in the atmosphere from local storms was the major source of opacity during the day (Pollack et al., 1977). As the summer season progressed there was a transition in local winds from being influenced by regional topography to one induced by global circulation (Hess et al., 1977). As the seasons progressed into northern fall and winter, a ground fog was detected to condense in the evenings and last throughout the night until sublimating shortly after sunrise. At both VL sites a seasonal pattern of decline was detected during the spring and summer seasons corresponding to the loss of atmospheric mass with the growth of the southern polar cap. Ambient pressure reached a minimum at L_s 149º (late northern summer) and increased with the sublimation of the southern polar cap as the southern hemisphere neared spring.

One detailed study was carried out to document dust devil activity near the VL-1 landing site. Ryan and Lucich (1983) analyzed temperature and wind sensor data for the first year of surface operations and isolated 47 sols out of the first three seasons after landing that provided valuable results (15 sols in the summer, 18 sols in the fall and 14 sols in the winter). To minimize bias, equal time intervals were chosen each season when MET data were optimal for vortex detection (consistent data with no data gaps or sampling rate limitations). Data

collected during the spring season wasn't used in the study due to anomalies that had not been resolved by the time their results were published. The ratio of the maximum horizontal wind speed along the track associated with the passing vortex (Δu_v) to the ambient horizontal wind speed (u_a) was used to identify an embedded vortex in the flow, where only situations in which $\Delta u_v/u_a > 1$ were regarded as possible vortices. A total of 40 vortices were detected: 23 in the summer, 12 in the fall, and 5 in the winter. The percentage of sols in each seasonal study that contained vortices was 60%, 33%, and 36%, respectively. The criteria used in identifying the signature of an embedded vortex was a rapid 360º rotation in the ambient wind vector, an abrupt rise in temperature if the core passed over the sensors, and an increase in wind speed as the vortex approached the lander followed by a minimum wind speed when the core reached the sensors.

Two major dust storms occurred within the first year of VL operations in 1977. The first (1977A) arrived at the VL-1 site during the early northern fall season (sols 209-222, L_s 207º-215º) and the second (1977B) arrived at the VL-1 site during the mid northern winter (sols 312-314, L_s 273º-275º) (Ryan and Henry, 1979). Both originated in the southern hemisphere and are centered about perihelion. The induced atmospheric dust during the storms caused significant increases in ambient pressure, wind speed, and aerosol optical depth and decrease in diurnal temperature amplitude. GCM data indicates that the fastest winds occur in the northern winter when Mars is at perihelion. Wind speeds during 1977A attained an hourly average of 17.7 m/s in the late evening and wind gusts as large as 25.6 m/s were recorded (Ryan and Henry, 1979). During 1977B wind speeds

reached a maximum average of 17.3 m/s with peak gusts recorded at 25.7 m/s. The speed of the largest gusts during each storm corresponds to a friction velocity of 2 m/s at 1.6 m, the height of the VL MET mast. Surface friction speeds to initiate erosion are 8 m/s for 10 μm dust-sized particles and only 2 m/s for 115 μm particles (Greeley and Iversen, 1985; White et al., 1997). It is probable that sediment was raised during the passage of either storm, and on surfaces where dust was exposed to the PBL winds it also may have been entrained. Dust optical depth at the VL-1 site remained over 2.0 for a period of 40 sols following 1977A and 60 sols following 1977B. During 1977A max wind speeds did not exceed 14 m/s (Ryan and Henry, 1979) at the VL-2 site. At that time the north polar cap had advanced to cover most of the area poleward of the landing site. Optical depth exceeded 2 for periods of 30 sols following 1977A and 50 sols following 1977B at the VL-2 site. Both VL sites experienced large wind speeds during the height of the storms and no vortices were detected at either site during periods when the largest wind speeds (> 20 m/s) were detected.

2.3.2 Viking Lander 2

VL-2 landed in Utopia Planitia (Gerald Soffen Memorial Station; 49.97ºN, 134.01ºE; ***figure 2.7***) on 3 September 1976 (44.5 sols after VL-1 landed in Chryse Planitia; L_s 120º early northern summer) just west of the large (~100 km diameter) Mie impact basin (Mutch et al., 1976, 1977). The flat terrain near the landing site displays very few craters, a shallow network of polygonal troughs not seen at the VL-1 site, and is covered in large boulders relatively uniform in shape, albedo, and texture (***figure 2.8***). VL-2 is thought to have landed on the distal part

of the Mie ejecta blanket. Rocks at the VL-2 site are regularly strewn about and displayed a bimodal size distribution of fine-grained (>100μm) aeolian sediment and large boulders (10-120 cm), indicating two distinct depositional events. The boulders contained numerous pits (few mm to few cm across) interpreted to be volcanic vesicles thought to have formed when the frothy volatile-rich part of a lava flow solidified and were later modified by aeolian abrasion. It has been theorized that either the boulders were emplaced as a poorly sorted debris flow as a result of the formation of Mie crater or represent an eroded lava flow that occurred after the formation of Mie crater (Carr et al., 1977; Mutch et al., 1977). Unlike the VL-1 site, there are no large drift deposits, very few wind streaks in the lee of rocks, and no exposed bedrock at the VL-2 site.

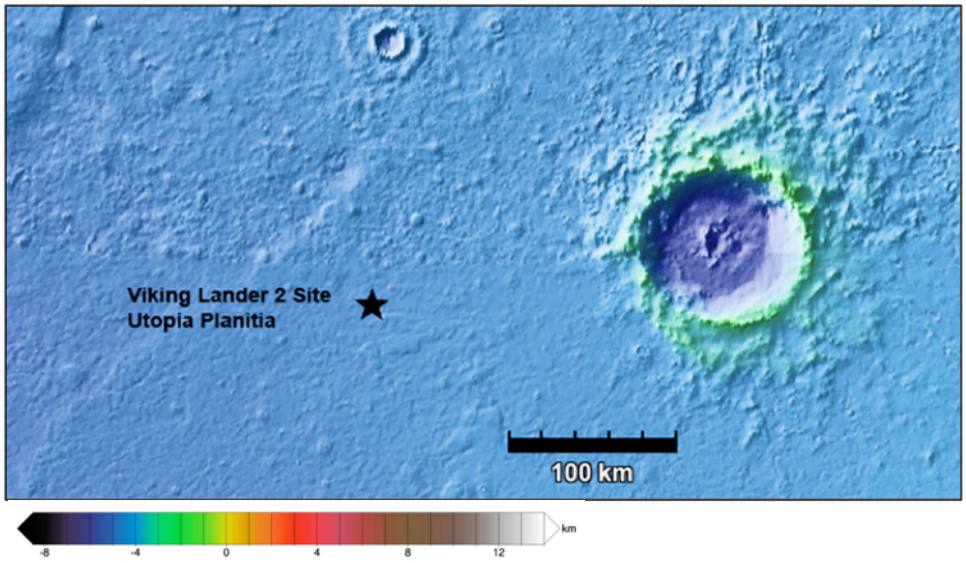

Figure 2.7 Colorized MRO Mars Orbiter Laser Altimeter elevation map showing location of Viking Lander 2 in Utopia Planitia

Figure 2.8. Viking 2 landing site taken with the lander's camera #2 in the afternoon. The apparent slope of the horizon is due to the 8-degree tilt of the spacecraft. Image credit: NASA/JPL PIA00364

Winds at the VL-2 site during the summer season were generally uniform with a 360º clockwise rotate during midday (Hess et al., 1977). The average wind speeds were somewhat higher in the morning than in the afternoon, but gusts had higher peaks in the afternoon (Hess et al., 1977; Anderson et al., 1977). During the summer season diurnal winds had a predictive pattern. Because VL-2 landed at 26º north of VL-1, weather patterns were more variable as the season progressed into fall. In the northern fall and winter seasons at the VL-2 site the average atmospheric pressure increased due to passing high- and low- pressure storm systems (Tillman et al., 1979). A low-lying ground fog and high altitude condensate H_2O ice clouds (northern polar hood) were first detected in early northern fall (sol 161, L_s 205º) and passed north of the VL-2 site approximately every 3.3 sols. Dust opacity was very low during the winter season as the northern polar hood extended down to latitudes of 40º (Pollack et al., 1977). As average temperatures declined, CO_2 condensed onto suspended dust and water ice

particles and formed larger heavier aggregates that would fall gravitationally to the ground (Pollack et al., 1977).

Two independent studies were carried out using the VL-2 MET data to analyze dust devil activity (Ryan and Lucich, 1983; Ringrose et al., 2003). Ryan and Lucich (1983) analyzed a years worth of temperature and wind data and unlike the investigation using VL-1 data, all four seasons at the VL-2 site were included in the results. Similarly to what was done for VL-1 data to minimize bias, equal time intervals were chosen from each season and only consistent data with no gaps or sampling limitations were used in the study. A total of 151 sols were analyzed (55 sols during the summer season, 21 during the fall, 52 during the winter, and 23 during the spring) and from that 78 vortices were detected (41 during the summer, 7 during the fall, 5 during the winter, and 25 during the spring). The percentage of sols in each seasonal study in which vortices were detected were 58%, 19%, 8%, and 70% respectively.

The second study by Ringrose et al. (2003) analyzed MET data from only the first 60 sols after the VL-2 landing to limit the amount of bias from increased sampling rates after sol 60. Out of the 73 events identified in temperature and wind vector data, 38 were determined to be true convective vortices. The results were categorized by statistical confidence and intensity. The vortices were divided into three categories: (1) events where the core passed directly over the sensors (2) events where the core passed just outside the sensors but the sensors were still within the zone of influence and (3) events where instruments were far outside the core. Ringrose et al. (2003) used a method similar to the MATADOR

2001 terrestrial field campaign (Hecht et al., 2001). The technique compared a time-average mean in wind vector data to a specified threshold value (commonly called a *phase picker*: |STA-LTA| > threshold) where the short term mean (STA) was calculated using the running average of the three most recent wind vector samples and the long term mean (LTA) was calculated using the running average of the 50 most recent samples. The threshold values used in the study were 6 m/s for wind speed and 40º for wind direction.

2.3.3 Mars Pathfinder Lander

Pathfinder arrived at its landing site in Ares Vallis (Sagan Memorial Station; 19.28ºN, 326.45ºE; ***figure 2.9***) in southern region of Chryse Planitia on 4 July 1997 (Golombek et al., 1997; Golombek and Bridges, 1999). It was one of the first in a series of low-cost Discovery-class missions designed to test new innovative technologies since the Viking Landers two decades prior to its landing (Golombek, 1997). These technological upgrades would lay the foundation for an advanced suite of scientific instruments, new EDL descent maneuvers, and solar-powered engineering technologies for the MER mission. The most significant technological advancement of the Pathfinder mission involved autonomous deployment of inflated airbags during the descent phase of EDL to safely land the spacecraft onto the surface in a series of small bounces until it rolled to a stop (Golombek and Bridges, 1999). Pathfinder was the first mission to deploy a rover (*Sojourner*) to the surface to provide close-up chemical analysis of the terrain over hundreds of square meters in the landing area.

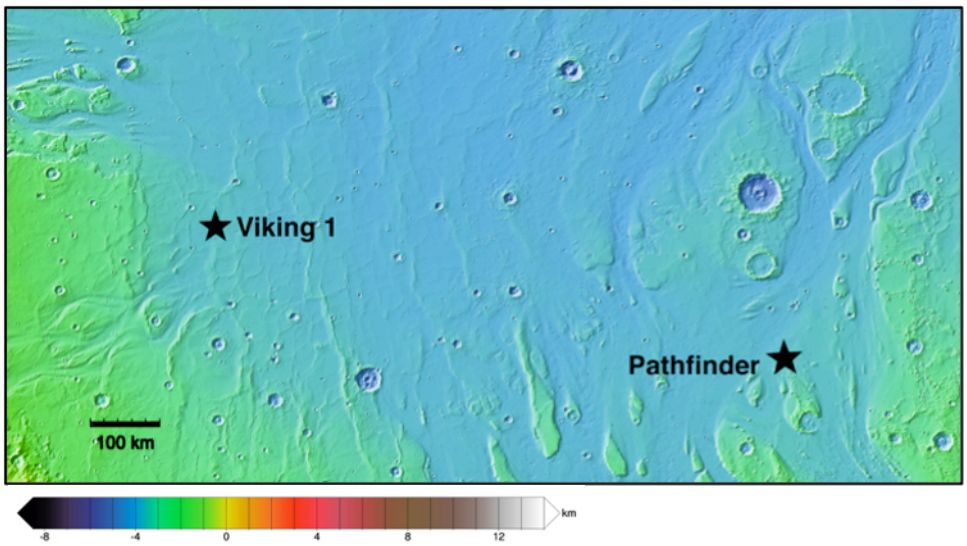

Figure 2.9. Colorized MRO Mars Orbiter Laser Altimeter elevation map showing the locations of the Viking Lander 1 in Chryse Planitia and Mars Pathfinder Lander in Ares Vallis

Located at the border of the northern equatorial lowlands, just a few hundred kilometers east of the VL-1 landing site, Ares Vallis is thought to be the remnant of an ancient flood plain complex (Ward et al., 1999). The landing site is characterized by a series of complex ridges and troughs, poorly sorted semi-rounded cobbles and boulders (ranging from few cms to 7 m in size), and fine-grained sediment (combination of soil deposits and aeolian dust) (***figure 2.10***). Aeolian features not previously seen at the VL sites, such as barchan-like bedforms and rocks abraided by wind surround the lander. Dust deposited by regional storm activity settled onto the Pathfinder solar petals over the coarse of the mission (Greeley et al., 1999). Wind tails ranging from less than a cm to 40 cm in length were the most common aeolian feature at the Pathfinder landing site. Smith et al. (1997) suggest that the materials at the landing site were deposited by the same catastrophic flooding events that created the deep incised outflow channels and streamlined islands found in the region.

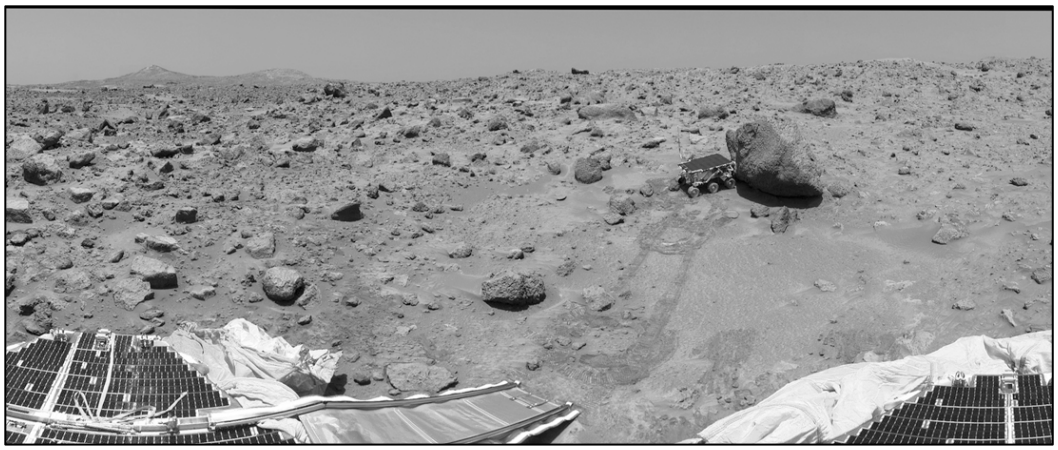

Figure 2.10. Mars Pathfinder landing site taken with the Imager for Mars Pathfinder part of the *Gallery Pan* taken on sols 8, 9, and 10. Lander solar panels, ramp and part of the deflated airbag can be seen in the foreground; the Sojourner rover can be see right of center analyzing a rock. The rover's wheel tracks were part of a soil mechanics experiment. Image credit NASA/JPL PIA01466

Pathfinder landed during the mid northern summer (L_s 142º) and remained operational into the early northern fall (L_s 183º) (Golombek et al., 1999) for a total of 83 sols. Large diurnal temperature gradients of ~ 60K driven by solar surface heating during the day and infrared cooling at night (Schofield et al., 1997) were detected. Rapid fluctuations in ambient pressure and temperature at midday indicated that the heated surface near the lander produced was convected upwards in small eddies. Ambient pressure measurements showed the same seasonal trends as was recorded by VL-1. The mean ambient pressure fell to a minimum (6.7 mbar) near L_s 153º corresponding to CO_2 condensation and sublimation in the polar regions (Schofield et al., 1997). Diurnal variations in the vertical temperature gradient were consistent from day to day. Schofield et al. (1997) note that early in the morning (~0630 LST) all three mast-mounted thermocouples measured nearly equal temperature measurements indicating that the near surface environment was neutrally stable and adiabatic. By about 0730 LST significant ground heat could not be transferred to the atmosphere through

conduction causing the atmosphere to become unstable and the thermal gradient to reverse. This signified the beginning of daytime convection and turbulence. In the evening (~1645 LST) as the surface cooled the thermal gradient was again neutral indicating convection had shut down near the lander. Cooling of the surface at night caused inversion in the atmosphere and stability to the PBL. A Mars Mesoscale Model (MMM5) was used to simulate the region covering Chryse Planitia and Ares Vallis (Tyler et al., 2002) during the northern summer season when VL-1 and Pathfinder landed. Similar to diurnal wind patterns measured by VL-1 in Chryse Planitia, diurnal patterns of wind flow in Ares Vallis were dominated by drainage winds flowing down Ares Vallis at night followed by a reversal of winds up Ares Vallis during the day (***figure 2.11***). Local topography and PBL conditions also influenced the ambient wind vector.

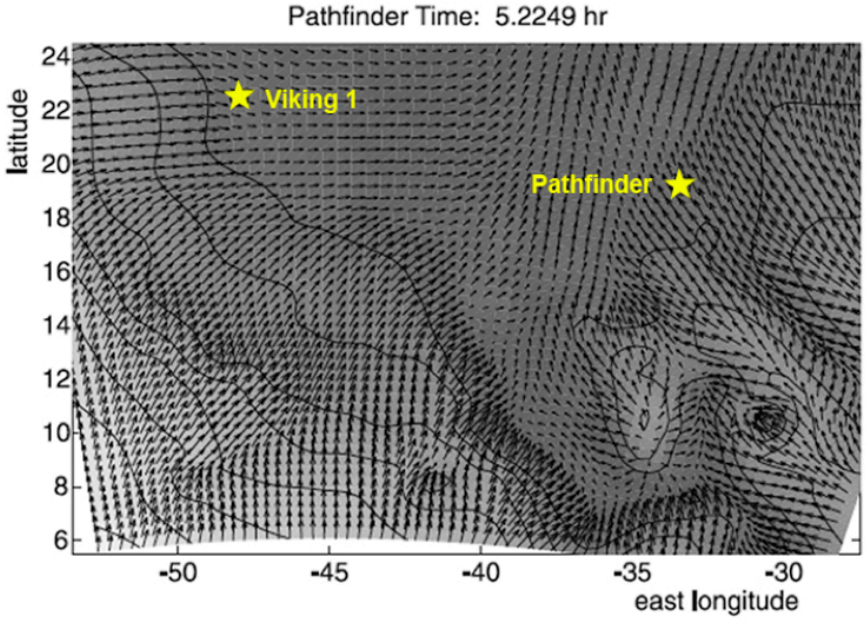

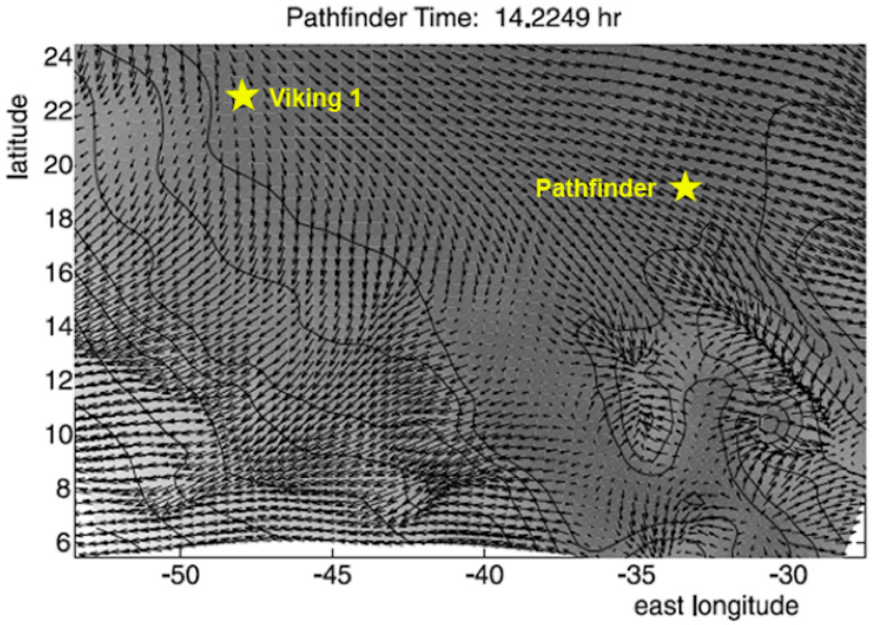

Figure 2.11. Mars Mesoscale Model 5 (MMM5) predicted surface winds (8-sol average) in the location for the Viking Lander 1 (Chryse Planitia) and Mars Pathfinder Lander (Ares Vallis) sites in the early morning (top) and midafternoon (bottom). Local time is referenced to the Pathfinder site during late northern summer. Maximum wind speeds are ~ 10m/s. Color and contour lines show topography at 500 m intervals; after Tyler et al., 2002.

Active dust devils were both imaged and detected in 3 separate studies (Metzger et al., 1999; Murphy and Nelli, 2002; Ferri et al., 2003). The first study by Metzger et al. (1999) resolved for the first time dust devils in optical images taken from the martian surface. Using spectral enhancement techniques and follow-up processing (consisting of filter ratios that created pseudocolor composites and analysis of single monochrome frames) five dust devils were resolved in IMP frames. As described by Metzger et al. (1999) dust devils appeared most strongly in visible blue images. All five dust devils were resolved in raw image frames from the Gallery Panorama sequence (panoramic frame numbers 164-165) taken on sols 10 and 11 of the Pathfinder mission. It was determined based on contrasts in pixel digital number (DN) between topographic features very far on the horizon that dust devils would only be resolved within 14

m of the lander and those dust devils must have diameters greater than 120 m to be resolved. 20 vortices were also detected from MET pressure and temperature fluctuations, but they did not elaborate on those detections.

The second study (Murphy and Nelli, 2002) focused on pressure sensor data and detected the passage of 79 vortices throughout the 83-sol mission. They relied on abrupt fluctuations in pressure measurements to identify vortices. The vortices were detected using a combination of a computer algorithm that identified large deviations from the average ambient pressure fluctuation and visual inspection of the pressure perturbations flagged.

In the third study Ferri et al. (2003) reviewed all MET and optical image data to search for additional dust devils overlooked by the previous studies. In total, Ferri et al. (2003) resolved 14 dust devils (including the 5 originally discovered by Metzger et al., 1999) in IMP frames using contrast enhancement and spectral differencing techniques. All dust devils except one imaged on sol 2 before the IMP mast was deployed were found in Gallery Panorama frames taken on sols 10 and 11 against the horizon. The 79 vortices discovered by Murphy and Nelli (2002) were reanalyzed and the durations of the Δ-P for 19 of the vortices were derived. Even though no simultaneous MET detection or optical imaging were available for verification, Ferri et al. (2003) noted that a sudden increase of ~ 0.1 in the measured atmospheric dust opacity (as measured by IMP imaging of the Sun in different filters) at 1100 LST on sol 14 suggested the potential passage of a dust devil over the lander. Schofield et al. (1997) also noted that the passage of a vortex on sol 62 was correlated with a short-lived reduction (~ 1.5%) in solar

power indicating that the dust concentrated column temporarily blocked incoming solar radiation from reaching the solar panels.

2.3.4 Mars Exploration Rover Spirit

The Mars Exploration Rovers (MER) Spirit and Opportunity are identical roving spacecraft that landed in two distinct equatorial regions in the southern tropics on 4 and 25 January 2004, respectively (Crisp et al., 2003). The MER mission was developed as part of NASA's Mars Exploration Program (MEP), which aims to determine whether conditions were at any time suitable for supporting life. NASA strives to answer this question by searching for evidence that liquid water was once stable and available on the martian surface through robotic exploration and intensive remote sensing. MER were primarily sent to Mars to seek clues to the history of liquid water in the surface geology at each landing site and find evidence for past or present habitable surface conditions (Golombek et al., 2003, Squyres et al., 2003). Engineering constraints required both MER landing sites to have low near-surface (few kilometers) PBL wind shear and mild turbulence to minimize the amount of horizontal drift experienced by the spacecraft during EDL (Golombek et al., 2003, 2005).

Spirit's landing site (Columbia Memorial Station; 14.57ºS, 175.47ºE; ***figure 2.12***) on the floor of Gusev crater (~160 km diameter impact basin) was chosen mainly because of an 800 km long sinuous channel, Ma'adim Vallis, that breached the crater's southern rim (Kuzmin et al., 2000; Cabrol et al., 2003; Golombek et al., 2003). It is theorized that liquid water carved the channel as it flowed into the crater and possibly pooled into an ancient lake, depositing fluvial

sediments at its mouth much like modern terrestrial delta systems (Arvidson et al., 2004). Subsequent low viscosity flood lavas, however, have covered any trace of ancient lakebed sediments in the cratered plains (Greeley et al., 2005) and left behind a surface comprised mainly of angular, olivine-rich, basaltic rock and impact-generated basaltic regolith, draped in a thin veneer of aeolian dust (McSween et al., 2004, Morris et al., 2004, Christensen et al., 2004, Grant et al., 2004; Arvidson et al., 2006; Greeley et al., 2004, 2005, 2006b). The low-relief cratered plains where Spirit landed contain many shallow, sediment-filled, circular depressions (commonly *hollows;* few meters to tens of meters in diameter) and inactive, dust-covered, indurated bedforms (Golombek et al., 2006).

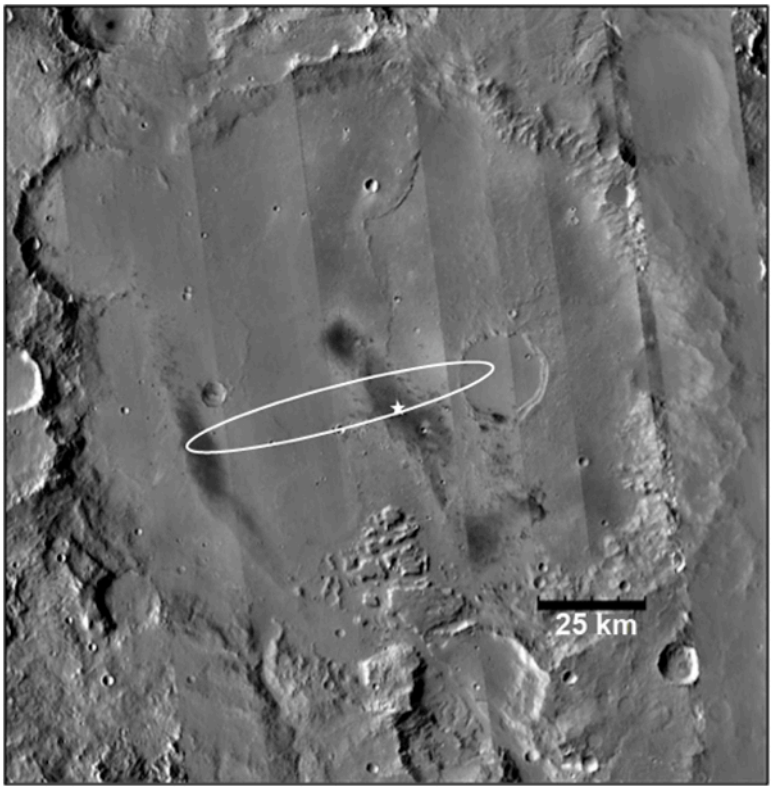

Figure 2.12. Mars Reconnaissance Orbiter Context camera images superposed onto Mars Odyssey THEMIS Daytime IR mosaic showing Spirit's landing ellipse (white oval) and landing site location (white star) in Gusev crater

Spirit landed in a relatively calm environment with smooth topography and moderate surface roughness. The plains were scientifically interesting with direct evidence for recently active near-surface convection and turbulent winds. Spirit landed in a portion of its landing ellipse covered with low albedo NW-SE trending tracks formed by the recent passage of dust devils (Squyres et al., 2004; ***figure 2.13***). Aeolian activity at the Spirit site was investigated prior to landing through analysis of features and the use of wind models (Greeley et al., 2003). The Mars Regional Atmospheric Modeling System (MRAMS; Rafkin et al., 2001, 2002) simulated the atmospheric circulation at both MER sites prior to landing at mesoscale resolution to emphasize complex topographic influences on local atmospheric motions (Rafkin and Michaels, 2003). The model uses nested grids (1/32º gridded MOLA data with 1.5 km spacing) and is capable of simulating high-resolution surface properties (Rafkin et al., 2001, 2002). MRAMS predictions (***figure 2.14***) for Spirit's landing site described a diurnal pattern of insolation-driven thermal circulations influenced by Gusev's shallow, flat-floored, bowl-shaped crater topography (Greeley et al., 2003; Rafkin and Michaels, 2003). Shortly after sunrise, winds generally flow radially outward from the center of the crater. In the evening as temperatures plummet, MRAMS predicted a general 180º reversal in flow direction of higher density katabatic winds from the crater rim, down the walls and back towards the center of the crater.

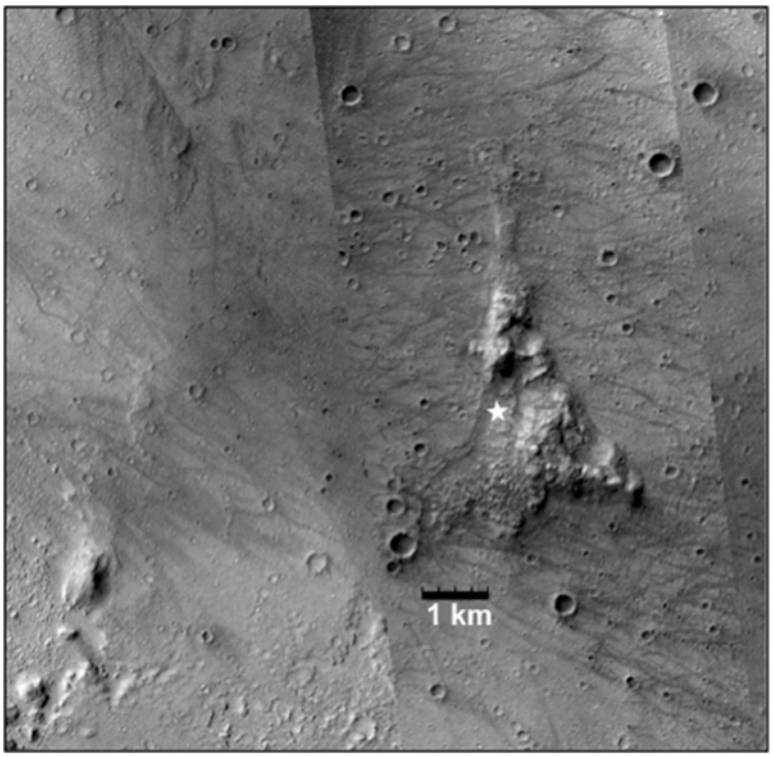

Figure 2.13. Mars Reconnaissance Orbiter High Resolution Imaging Science Experiment images superposed onto Context camera mosaic showing the cratered plains surrounding the MER Spirit landing site and the rover's current position (white star) in the Inner Basin of the Columbia Hills.

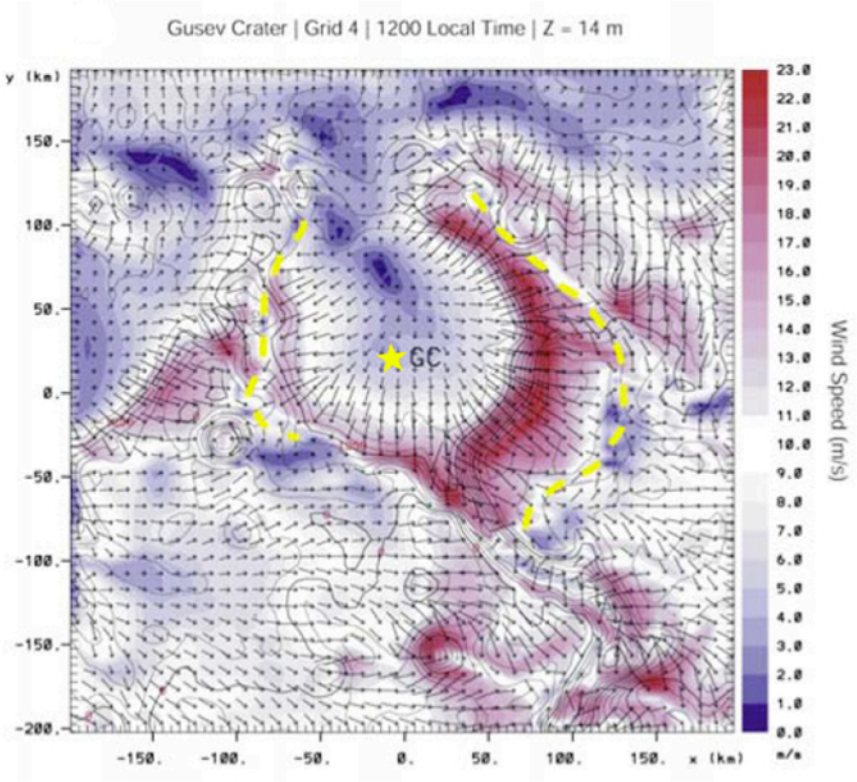

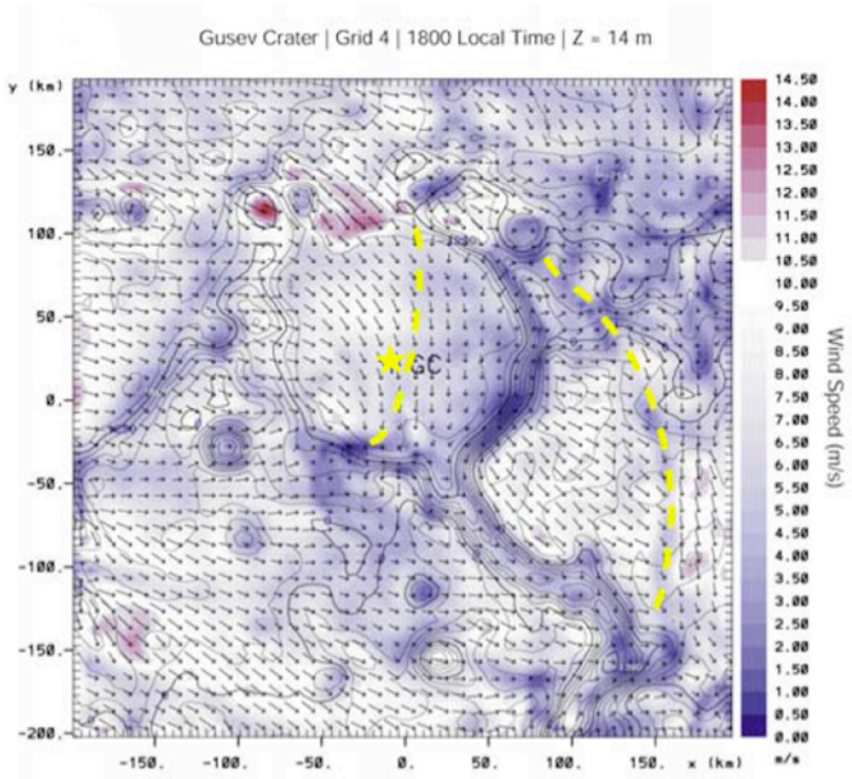

Figure 2.14. MRAMS predicted wind vectors surrounding the MER Spirit landing site (yellow stars) in Gusev crater at 1200 LST (top) and 1800 LST (bottom); atmospheric circulation is derived for elevation of 14 m above the surface; yellow dotted line represents the location of the main convergent wind boundaries; from Rafkin and Michaels, 2003.

Spirit's dust devil observations comprise the largest and most detailed data set on this topic and provide a great opportunity to study seasonal variations at the Gusev landing site location before comparing these results to other data sets. At the beginning of the warm, dusty southern seasons (spring and summer; L_s 180º-360º) when Spirit generally had the most power, activities specifically for dust devil detection became a regular remote sensing activity. To date, 761 dust devils have been identified and analyzed from pictures returned from the rover's optical cameras (Greeley et al., 2006, 2010). The locations of the dust devils were mapped onto Mars Reconnaissance Orbiter (MRO) High Resolution Image Science Experiment (HiRISE) images based on the identification of topographic

features and distinct landmarks (Greeley et al., 2006, 2010; ***figure 2.15***). The first step in comparing the Spirit data set was to determine the range of directions travelled by the dust devils within each season and from one season to the next. Dust devil movement is used to infer the movement of the local wind vector that pushed the dust devils across the plains. Due to limited rover resources, dust devil observations were not performed regularly and images containing the horizon were not always available. Because the location of the rover changed each time the rover was commanded to drive, the camera viewing geometry varied from one season to the next (described in Greeley et al., 2010). Consequently, most of the dust devils imaged by Spirit's cameras were during Season One. During this time the rover viewing geometry was favorable for detection. To adjust for the inconsistent spatial imaging, all seasonal data were normalized to account for infrequent imaging and then extrapolated both spatially and temporally to account for limitations in viewing geometry (Greeley et al., 2006, 2010).

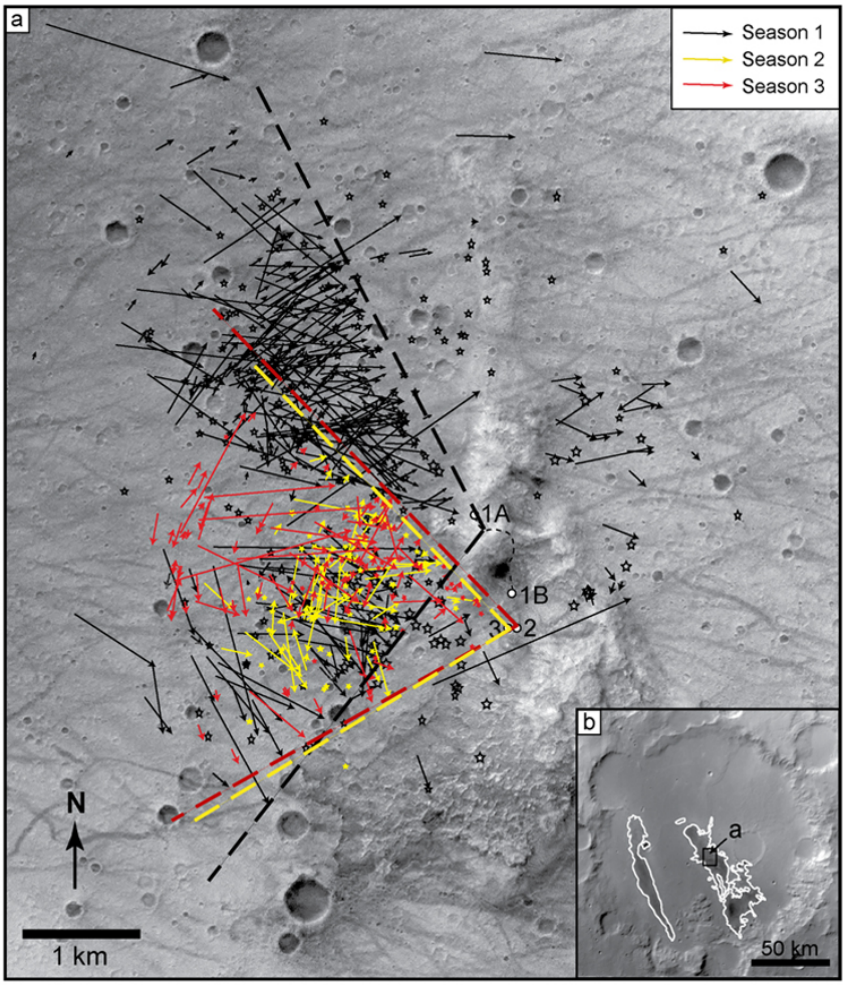

Figure 2.15. (a) Mosaic of MRO HiRISE images of Spirit's landing site in Gusev crater; vectors are dust devil paths for dust devils tracked in sequential frames and stars represent locations of active dust devils observed in a single frame (from Greeley et al., 2010). The black, red and yellow wedges represent the viewing geometry of the rover camera for the majority of each season. (b) MOC WA image R21-00168 inset of Gusev crater showing the low albedo zone (GLAZ; outlined) and the location of (a)

2.3.5 Mars Exploration Rover Opportunity

Opportunity landed on the flat, smooth, rippled plains of Meridiani Planum (Challenger Memorial Station; 354.47ºE, 1.95ºS; ***figure 2.16***) and, like its twin rover, Spirit, its primary objectives were to search for clues in the surface geology that its landing site environment may have supported liquid water in the past (Arvidson et al., 2003; Squyres et al., 2004). Dark fine-grained olivine-rich basaltic sands (~50-150 µm in diameter) cover the area surrounding the landing

site and are underlain by laminated sulfate-rich bedrock (Squyres et al., 2004). Opportunity's landing site in the Meridiani plains was chosen in large part because MGS TES (Christensen et al., 2000) revealed a ~15-20% (by fractional area) signature of gray crystalline hematite in a thick monolayer on the plains surface (Hynek and Phillips, 2001, Hynek et al., 2002, Arvidson et al., 2003; Golombek et al., 2003). After landing it was discovered that small (4 to 6 mm in diameter) spherical hematite concretions cover the basaltic soil as a thin lag deposit created from past deflationary episodes. Hematite forms by many different processes; the majority in the presence of liquid water.

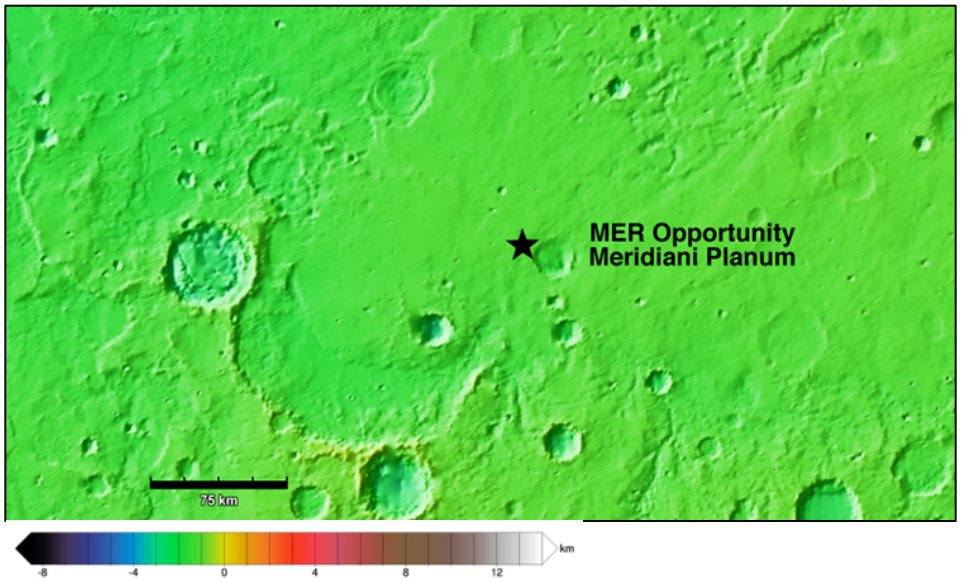

Figure 2.16. Colorized MRO Mars Orbiter Laser Altimeter elevation map showing the location of Opportunity in Meridiani Planum.

Like the Spirit landing site, aeolian activity has played a central role in reworking the Meridiani plains. This is evident by the presence of abraded outcropping bedrock, accumulations of loose sediment on crater floors, and abundant well-sorted course-grained sand ripples (~1 cm high) that formed from past episodes of saltation (Sullivan et al., 2005). Orbital observations reveal a low

albedo (~0.12) surface and Mini-TES analysis indicated that only a small amount of aeolian dust is present on the surface (Ruff and Christensen, 2002). Therefore, relatively high and frequent winds are assumed to be currently present at the landing site to remove airfall dust from the surface (Squyres et al., 2004).

MRAMS (Rafkin et al., 2001) and Martian Mesoscale Model Version 5 (Mars MM5; adapted to martian conditions by Toigo and Richardson, 2002 and run at resolutions of 10-100m to produce large eddy simulations) both predicted horizontal wind speeds of ~4 ± 2 m/s (Kass et al., 2003) at the time of landing. Mini-TES detected the presence of a superadiabatic layer during the warmest times of the day (9:30 to 16:30 LTST) and a deep inversion layer throughout the night (Smith et al., 2006). Short timescale (up to 60 sec) temperature fluctuations were recorded at the MER Opportunity site (Smith et al., 2006). These fluctuations were interpreted to be turbulent motions associated with near-surface convection as warm and cool parcels of air move with increasing insolation. Little temperature fluctuation was detected before 8:00 and after 17:00 LTST, indicating times when convection was shut off. Meridiani winds are much more variable than those at the Spirit site, however winds at the Spirit site were predicted to be stronger with elevated turbulence. MRAMS data showed erratic afternoon winds at the Meridiani site with the development of convective "cells" (Greeley and Thompson, 2003; ***figure 2.17***). Winds at the Meridiani site are dominated by upwellings and downwellings (Greeley and Thompson, 2003) making vertical winds random and robust (Rafkin and Michaels, 2003; Toigo and Richardson, 2003).

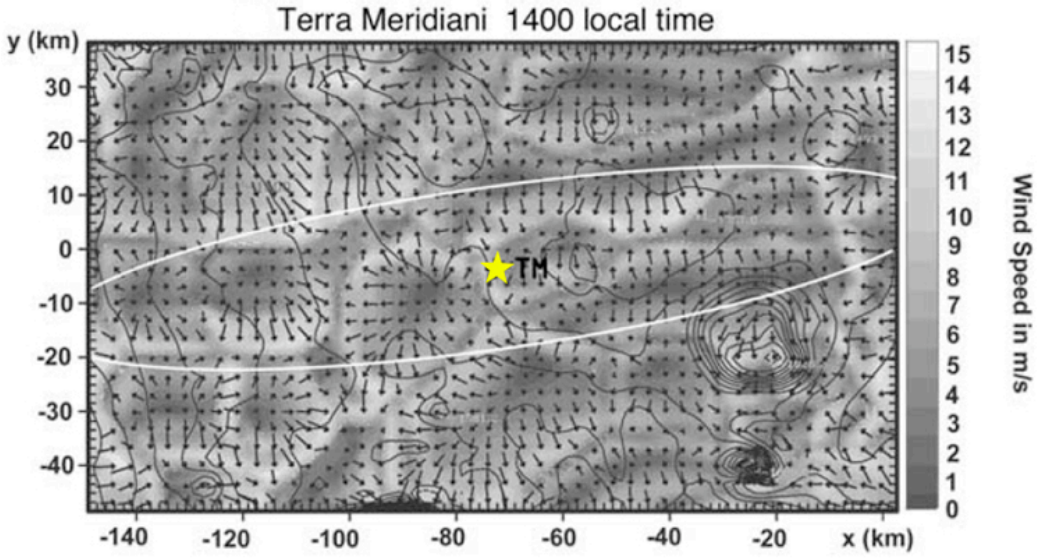

Figure 2.17. MRAMS predictions for local afternoon winds in the vicinity of the MER Opportunity landing site (yellow star) in Meridiani Planum show patterns of upwellings and downwellings (isolated convective cells); atmospheric circulations are derived for an elevation of 14.5m above the surface; from Greeley and Thompson, 2003.

Dust devil imaging campaigns were carried out early in the mission similar to those done at the Spirit site, however no dust devils were imaged during the times when the frequency of dust devil activity was predicted to be highest. After Spirit imaged its first complete dust devil season, it was determined that for unknown reasons the Opportunity site was not conducive to dust devil production. But on sol 2301 (15 July 2010), L_s 119º (mid southern winter) at 1401 LTST, Opportunity imaged its first and only (to date) dust devil in a Pancam image taken during a routine post-drive imaging campaign.

2.3.6 Phoenix Mars Lander

The northern arctic plains (68.22ºN, 234.25ºE***; figure 2.18***) were chosen as the landing site for the 2008 Phoenix Mars Lander, NASA's first Principal Investigator led Scout mission (Smith et al., 2008). Phoenix successfully demonstrated a soft landing using an autonomously powered descent engine to

land safely on the surface. On 25 May 2008 at 1620 LST, Phoenix landed on the distal deposit of the bowl-shaped 11.5 km-diameter Heimdel crater (Heet et al., 2009) in the Borealis basin on the northern flank of Alba Patera volcanic feature. The primary goals of the 151-sol mission (L_s 77º-148º; late northern spring to mid northern summer) were to investigate the presence of water ice in the near-surface soil with direct sampling, determine the history of water and possible habitability of the local environment, and monitor atmospheric variability in the high-latitude polar environment (Smith et al., 2008, 2009).

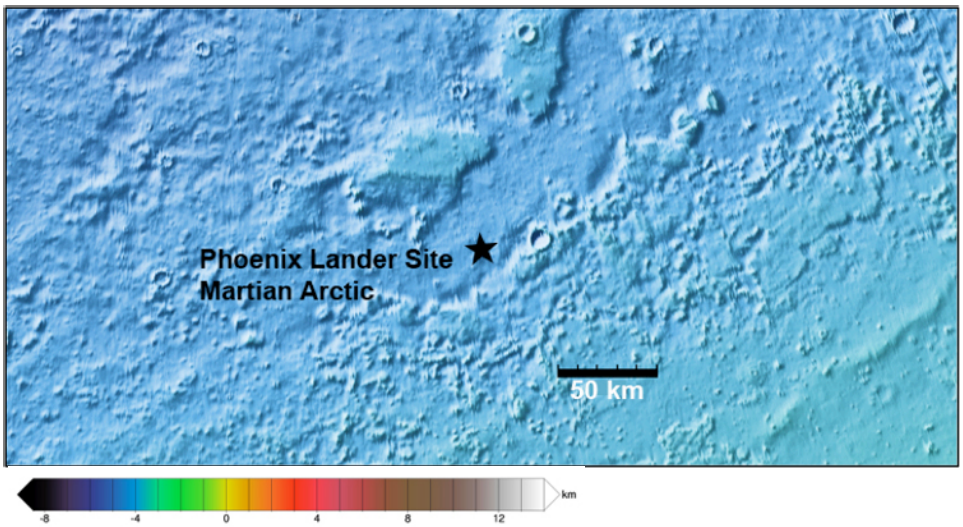

Figure 2.18. Colorized MRO Mars Orbiter Laser Altimeter elevation map showing the location of the Phoenix Mars Lander in the Martian arctic

The Phoenix landing site is characterized by a bimodal size distribution of polygonal troughs (~5 and 20 m), very few craters, and few rocks (Heet et al., 2009; ***figure 2.19***). The soil at the landing site is roughly 5 to 18 cm deep and covers a water ice-cemented soil with clay-silt as the dominant sediment size (Arvidson et al., 2009; Smith et al., 2009). Cryoturbation at the site is due to the repeated freezing and thawing of the soil and the formation of ice wedges that create the troughs. Crater counts from the Heimdal inner ejecta unit indicate that

Phoenix landed on the youngest martian landing site to date (~0.6 Ga). The lack of rocks of all sizes and craters at the landing site is attributed to the hyper-velocity speed impact that created Heimdal crater that may have entrained rocks in the debris flow and buried them far from the crater (Heet et al., 2009). The landing site has been subsequently differentially eroded by wind but there are no aeolian deposits or features near the lander.

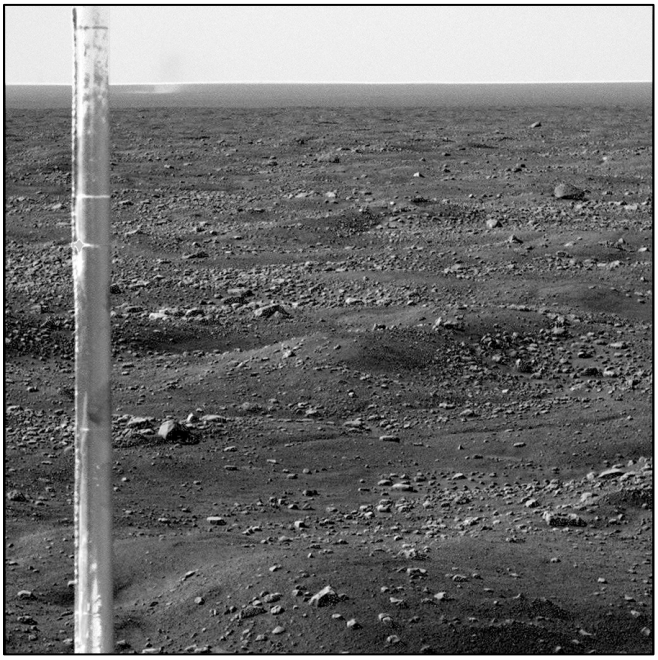

Figure 2.19. SSI image of flat plains surrounding the Phoenix landing site taken at 1116 LST on sol 104; MET Station mast dissects left side of the photo; a dust devil (few meters in diameter) can be seen to the right of the mast roughly 600-700 m from the lander; Credit: NASA/ JPL/ Univ. of Arizona/ Texas A&M University PIA11153.

Prior to the landing, MGS MOC Narrow Angle (NA) images were analyzed for evidence of dust devils and the density of dust devil tracks at the candidate landing site regions in four broad polar longitude bands (Drake et al., 2006). A very small percentage of active dust devils and wind streaks were seen in the region surrounding the Phoenix landing site and limited coverage of the arctic region did not allow rates of formation or erasure of aeolian features to be

calculated. Dust devil tracks were often seen around or within topographic features (Drake et al., 2006). Just 35 days prior to landing the MRO CTX imaged dust devils within the landing ellipse (Ellehoj et al., 2010).

A single study was conducted by Ellehoj et al. (2010) for activity at the Phoenix site. Convective vortices were inferred by abrupt (10-20 s) isolated pressure drops of about 0.3-1 Pa that were often accompanied by sudden increases in temperature. 502 vortices were detected with a pressure drop larger than 0.3 Pa in the raw data collected from the pressure sensor (Ellehoj et al., 2010). Of those 502 vortices, 197 had pressure drops larger than 0.5 Pa and 44 had pressure drops larger than 1 Pa. Activity detected from pressure measurements during the first 75 sols (L_s 77º - 111º; late northern spring to early northern summer) was less than 1.7 pressure perturbations per sol for Δ-P > 0.3. After L_s 111º the number of events per sol increases significantly with large short-term peaks and a general increase until the mission ends in L_s 148º. Due to the trend in increasing vortex activity, dust devil season probably continues after Phoenix stops operating on sol 151. There were 29 pressure perturbations recorded during the night (2100 to 0100 LMST) early in the mission with pressure drops > 0.3. They were attributed to local weather phenomena that occurred around midnight (turbulent air from Heimdal crater) and not passing vortices (Ellehoj et al., 2010; Holstein-Rathlou et al., 2010).

A total of 76 dust devils were imaged with the SSI. All dust devils were imaged within the last 46 sols of the mission (sols 104-151; L_s 125º-148º; mid northern summer). The initiation of the Phoenix dust devil season correlated with

increased regional storm related activity. After the first dust devils were discovered on sol 104 search campaigns similar to Spirit's Navcam dust devil movie sequences (Greeley et al., 2006, 2010) were frequently implemented into tactical plans to maximize detection.

CHAPTER 3 COMPARISONS AND RESULTS

3.1 Chapter Overview

Martian dust devils interact directly with landed spacecraft and have been imaged and/or detected at each of the six landing sites (***figure 1.5; table 2.1***). They are responsible for lifting large amounts of dust into the atmosphere; therefore, it is important to understand how they differ from one location to the next. Dust devils vary in morphology, speed, frequency, number density, and in the amount of dust they lift from the surface. There are many factors that control these parameters as dust devils develop and evolve, many of which are still poorly understood. In situ imaging and detection campaigns to monitor dust devil activity at each landing site reveals variations as a function of time of day, season, and due the type of terrain on which they form. This chapter compares landing site characteristics and dust devil parameters to provide a better understanding of the similarities and differences in dust devils as a function of these variables. Results have the potential to predict dust devil activity at future Mars landing sites, and elsewhere.

3.2 Landing Site Characteristics

Dust devils are PBL processes and are directly affected by surface variations. Moderate rock cover, little vegetation, and gentle slopes are favored for terrestrial dust devil formation (Brooks, 1960; Sinclair, 1969). On Earth, playas and riverbeds adjacent to freshly ploughed fields are prone to dust devils activity (Sinclair, 1969; Mattsson et al., 1993). Local topography and surface roughness elements are thought to be important for the generation of local eddies

that can induce vertical vorticity in a developing dust devil. Determining surface rock abundance is important for understanding the type of terrain best suited for dust devil formation. Rock abundance is the percentage of the field of view that is covered in material with a thermal inertia larger than that produced by consolidated material ~15 cm wide (~1250 $Jm^{-2}K^{-1}s^{-1/2}$; Christensen, 1986). Results from a field study in Nevada indicated that terrestrial dust devils are common on surfaces with rock abundances between 17-24% and are negligible on very rough and rocky surfaces with more than 40% rock cover (Metzger, 1999).

Rock abundances were determined for each of the Mars sites by analysis from orbit prior to landing to ensure safety during EDL. After the spacecraft landed rock abundances were estimated based on the analysis of landed images, providing ground truth to orbital observations (***table 3.1***). Thermal differencing techniques using the Viking Infrared Thermal Mapper (IRTM) and the MGS TES thermal inertia data were used to generate 1 m/pixel and 8 m/pixel (respectively) global rock abundance maps (Christensen, 1986; Nowicki and Christensen, 2007). Because nighttime emission is controlled by thermophysical properties, nighttime thermal surface observations are used to determine the areal fraction of rocks (Neugebauer et al., 1971; Kieffer et al., 1973; Christensen, 1986). The VL-1, VL-2, and Pathfinder surfaces were rockier than at the Spirit, Opportunity, and Phoenix sites (Golombek et al., 1997; Nowicki and Christensen, 2007; Heet et al., 2009). Rock abundance at the Spirit site is similar to the global mode of 8% (Golombek et al., 2005). Very low rock abundance (0-10% cumulative fractional area covered by rocks; Golombek et al., 2010) was found at the Phoenix site in

the martian arctic. Because dust devils were imaged or detected at each site, it can be determined that martian dust devils can persist on surfaces with rock abundances between 0-19%.

Landing Site	TES Rock Abundance	IRTM Rock Abundance	Lander Observations
Viking 1	8 ± 5	16	16
Viking 2	13 ± 4	17	16
Pathfinder	12 ± 4	19	19
Spirit	11 ± 4	8	7
Opportunity	NA (9 ± 6)	5	≤5

Table 3.1. Estimates of landing site rock abundances from orbital thermal differencing techniques and lander observations; after Nowicki and Christensen, 2007.

Aerodynamic surface roughness (z_0), a theoretical length that is determined by extrapolating the curve in a logarithmic wind profile down to a wind speed of zero (Bagnold, 1941), is another parameter that is important in quantifying the surface. Based on spectral analysis of high-frequency PBL measurements, a roughness of ~ 1cm was calculated for the boulder-strewn VL-2 site (Tillman et al., 1994). Surface roughness estimates made from direct measurements of ambient winds at multiple heights produced an estimate of ~ 3cm at the Pathfinder (Sullivan et al., 2000). Surface roughness was not calculated at either MER site due to the lack of instruments capable of measuring the local ambient wind vector. Surface roughness was estimated to be 5-6 mm at the Phoenix site (Heet et al., 2009).

Typical martian surfaces seen in orbiter and ground-based images are covered with sediment of sizes ranging from boulders to dust. Landing site surfaces with mixed sediment sizes and compositions display a large range of surface temperatures (Kieffer et al., 1977; Christensen, 1982) due to variations in

surface thermal inertia, a measure of how responsive a surface material is to diurnal temperature changes. Thermal inertia depends on particle size, composition, and rock abundance on the surface (Christensen and Moore, 1992). Surfaces that are mantled with loose dust typically have lower thermal inertia and higher albedo, and surfaces with exposed rock or duricrust have higher thermal inertia. TES-derived thermal inertia values for each of the landing sites were determined from spectral and bolometric surface temperatures. TES thermal inertias and albedos for the six landing sites are shown in ***table 3.2***.

	TES Thermal Inertia ($Jm^{-2}K^{-1}s^{-1/2}$)	TES Albedo
Viking 1	283 ± 14 [a]	0.216 [a]
Viking 2	234 ± 11 [a]	0.238 [a]
Pathfinder	386 ± 10 [a]	0.186 [a]
Spirit	315 [b] (mini-TES 150-430 [c])	0.19 [b]
Opportunity	200 [b] (mini-TES 225 [d])	0.12 [b]
Phoenix	310 (day)/ 260 (night)[e]	0.20 [e]

[a] Putzig et al., 2005
[b] Golombek et al., 2005
[c] Christensen et al., 2004
[d] Christensen et al., 2004b
[e] Zent et al., 2010

Table 3.2. Average TES thermal inertias and albedos determined for each of the six landing sites.

Thermal inertia at the Spirit site is typical for a surface made up of a lag deposit of cohesionless sand and granules overlaying exposed bedrock (Presley and Christensen, 1997; Golombek et al., 1997). Spirit's low albedo surface is due to the dark tracks where dust devils removed the top layer of loose surface dust. Opportunity's site has a low thermal inertia and low albedo attributed to a composition of fairly uniform fine sand and very little bright surface dust (Ruff and Christensen, 2002). The Viking Lander sites have high thermal inertia and intermediate albedo attributed to a rocky surface composed of cohesive fine-grained material and some loose dust (Putzig et al., 2005). The very rocky Pathfinder site has the highest thermal inertia of all the past landing sites with an

albedo equivalent to the Spirit and Phoenix sites. Low albedo surfaces may trigger activity at a greater rate than higher albedo surfaces. Dark surfaces warm more rapidly in midday insolation and will generate larger near-surface gradients and deeper convective wells.

Local topography plays a significant role in the formation of dust devils at the lower latitude VL-1, VL-2, Pathfinder, and Spirit sites. Midday surface heating produces PBL convection and topography may provide a trigger for the source of vorticity in the form of thermal eddies. Dust devils were imaged by Opportunity and Phoenix on relatively flat smooth surfaces and it is not well understood what the main sources of vorticity are for these dust devils. Past studies indicate that dust devils show no preference in rotation direction (Sinclair, 1969, 1973; Ryan and Lucich, 1983) so dust devils are considered too small to be controlled by planetary rotation and Coriolis effects. Models suggest that dust devils that form on flat surfaces are possibly generated from horizontally aligned vortices that are subsequently twisted into a vertical alignment and raised to a vertical orientation from the surface (Rennó et al., 2004). Large eddy simulations indicate that the martian PBL can rapidly develop horizontal vorticity as a result of free convection due to insolation (Toigo et al., 2003).

3.3 Dust Devil Morphology

Terrestrial dust devils vary from narrow, columnar features to V-shaped plumes with wide tops that taper near the surface (Metzger, 1999). In field studies dust devils had dust-free cores (Sinclair, 1973; Bale et al., 2003) and in others (Metzger, 1999) a distinct dust-free core could not be found. Terrestrial dust devil

diameters are typically smaller than 100 m with heights up to 2500 m (Mattsson et al., 1993; Rennó et al., 2000; Neakrase et al., 2006). Because dust devils are in contact with the surface as they are moved by the ambient wind, their horizontal speeds and directions can be used as an indication of the ambient wind vector (Chamberlain et al., 1976). Terrestrial dust devils observed with defined central columns tilt up to 10º in the direction of motion (McGinnigle, 1966; Sinclair, 1973; Mattsson et al., 1993). Dust devils are generally much higher than they are wide (Sinclair, 1966, 1969; Carroll and Ryan, 1970) and their thermal updraft may be much larger than the visible dust-laden part of the column. Terrestrial dust devils are at least 5 times higher than they are wide and most are densely particle-loaded near the ground (Sinclair, 1966; Hess and Spillane, 1990). Studies have shown that the frequency of dust devil occurrence is inversely related to size and that the distribution is typically skewed toward the smaller sizes.

Similarly to terrestrial dust devil, those devils imaged by Pathfinder, Spirit, Opportunity and Phoenix varied in morphology from narrow tubular columns, to broad V-shaped plumes, and ellipsoidal features with diffuse edges. When the same dust devil was imaged in sequential frames or in multiple filters of the same frame, the upper portions of the columns were seen to tilt in the direction of movement. This is inferred to be a result of stronger wind shear at higher elevations. Height estimates for most dust devils were very difficult to measure because of the difficulty in resolving the upper portion of the dust devil against the brighter atmospheric haze and in many cases the top of the plume extended

beyond the frame. Ranges of core diameters varied greatly from one site to the next are addressed separately below.

MER Spirit

Approximate core diameters of dust devils imaged by Spirit were derived by determining the number of pixels the dust devil spanned in the rover images, and then estimating its distance from the rover based on identification of surface features in orbital HiRISE frames. The range of diameters measured for Spirit's three dust devil seasons were 2 to 276 m in Season One, 5 to 124 m in Season Two, and 5 to 227 m in Season Three (Greeley et al., 2006, 2010). In most cases during the three seasons the direction of column rotation (clockwise or counter clockwise) could not to be determined.

Data from orbital and ground-based studies indicate that the dust devils observed directly by Spirit may represent the smaller size range of dust devils that are generated in the Gusev plains (Verba et al., 2010). MRO HiRISE images have shown that dust devil tracks near the Spirit landing site are formed by the largest dust devils, which were infrequently captured by Spirit's cameras (Verba et al., 2010). Track formation in Gusev crater is rare compared to the number of dust devils imaged from the ground; forming at a rate of less than 1/110 the occurrence of the active dust devils imaged from Spirit's cameras (Verba et al., 2010; Greeley et al., 2006, 2010). Tracks in Gusev crater have widths that peak between 40 and 60 m with a mean of 56 m (***figure 3.1***). Dust devil track widths are much larger than the dust devils imaged in ground-based Navcam frames. Dust devils imaged by Spirit peaked in size between 10 and 20 m for Seasons One and Two

and between 20 and 30 m for Season Three (***figure 3.2***). This may indicate that the large track-forming dust devils did not pass very near to the Spirit rover at the times the surface cameras were imaging the plains. It can be assumed that the smaller more frequent dust devils imaged by Spirit's cameras did not lift enough dust to leave a track visible from orbit (Verba et al., 2010).

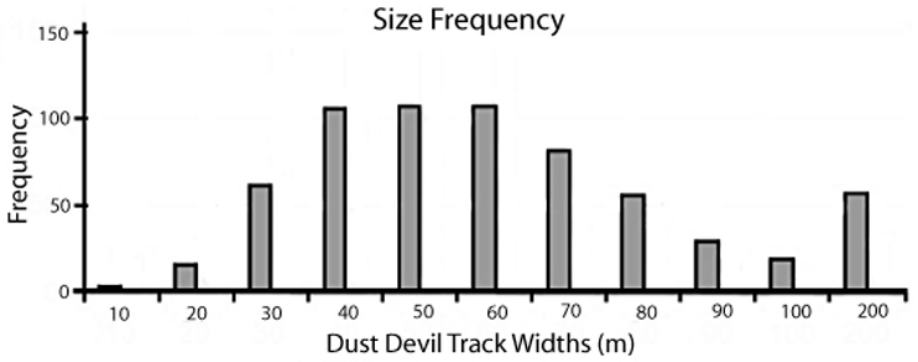

Figure 3.1. Size frequency distributions of Gusev crater from dust devil tracks; after Verba et al., 2010

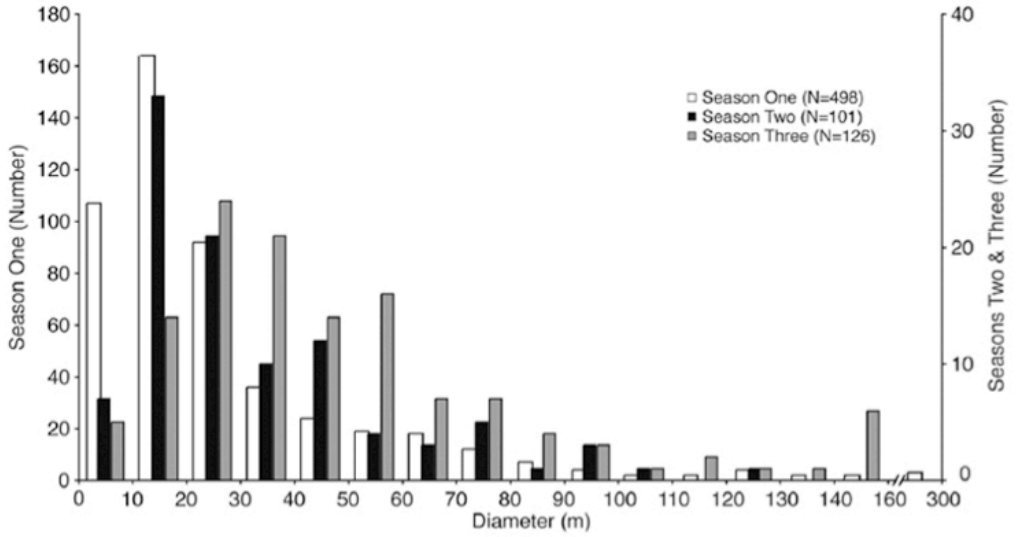

Figure 3.2. Numbers of dust devils imaged for three seasons as a function of diameter; from Greeley et al., 2010

Phoenix Lander and MER Opportunity

Sizes of dust devils imaged by Phoenix and Opportunity were difficult to constrain. Uncertainties in dust devil diameters at the Phoenix site were due to the

inability to pinpoint exact dust devil locations in the flat arctic plains (Ellehoj et al., 2010). Estimates for the 76 dust devils imaged in the arctic plains ranged between 20 and 200 m assuming only that the plumes were in cyclostrophic balance (a condition in which horizontal atmospheric pressure and centrifugal force within the vortex are acting equal and opposite each other).

There is a large uncertainty in the location of the single dust devil imaged by Opportunity due to the lack of prominent topographic features in the image. Therefore, its size was difficult to constrain. The location of the dust devil is difficult to pinpoint because the base of the plume cannot be determined in the Pancam frame. In the Pancam image (***figure 3.3***) ripples can be seen in the foreground and the dust devil is either located at or behind the horizon. If the dust devil's true structure is V-shaped then it can be inferred that a large portion of the bottom of the dust devil is hidden behind the horizon. The near (western) rim of Endeavour (***figure 3.4*** location 1) is located roughly 11 km from the base of the image (which is ~22 m from the rover). From Opportunity's viewing perspective on the sol the dust devil was imaged Endeavor's near rim is not visible. It is uncertain whether the horizon is at the western rim of Endeavor. MOLA elevation data implies that it is not based on the general eastern slope of the region. The prominent dark topographic feature to the left of the dust devil is thought to be a raised portion of the far (eastern) rim of Endeavor crater roughly 27 km from the base of the image (***figure 3.4*** location 2; Timothy Parker, personal communication, 2010).

The Pancam high-resolution stereo pair was used to estimate the distance from the rover to the dust devil. Nearby objects have a larger parallax than more distant objects in the same frame. The left and right Pancam lenses are separated by 30 cm, the largest separation distance possible within engineering restrictions, providing good ranging accuracy for distant targets (Bell et al., 2003). When the Pancam stereo pair was overlapped and parallax was measured, large displacements were seen in the ripples all the way to the horizon, whereas no perceivable shift was seen in the dark topographic rise or in the dust devil. The only movement seen in the dust devil was from slight differences in location of noise (assumed to be dust associated with plume) in the two frames. It was determined that the dust devil was much farther away than previously assumed, and the consensus was that it could be located inside Endeavor crater (Jim Bell, personal communication, 2011). If the Opportunity dust devil was located inside Endeavor crater then it can be argued that it formed as a result of small-scale vorticity by thermal eddies that were generated by spin-off convection from the uneven crater surface.

***Figure 3.3*.** Only dust devil imaged by Opportunity in Meridiani Planum (to date) in a Pancam image (1P332460904RSDALNMP2369L2MZ) taken on sol 2301 (15 July 2010); Pancam is mounted 1.54 m above the surface; center of the frame is oriented due east with a elevation angle of 4º from horizontal; bottom of frame is roughly 22 m from the base of the rover.

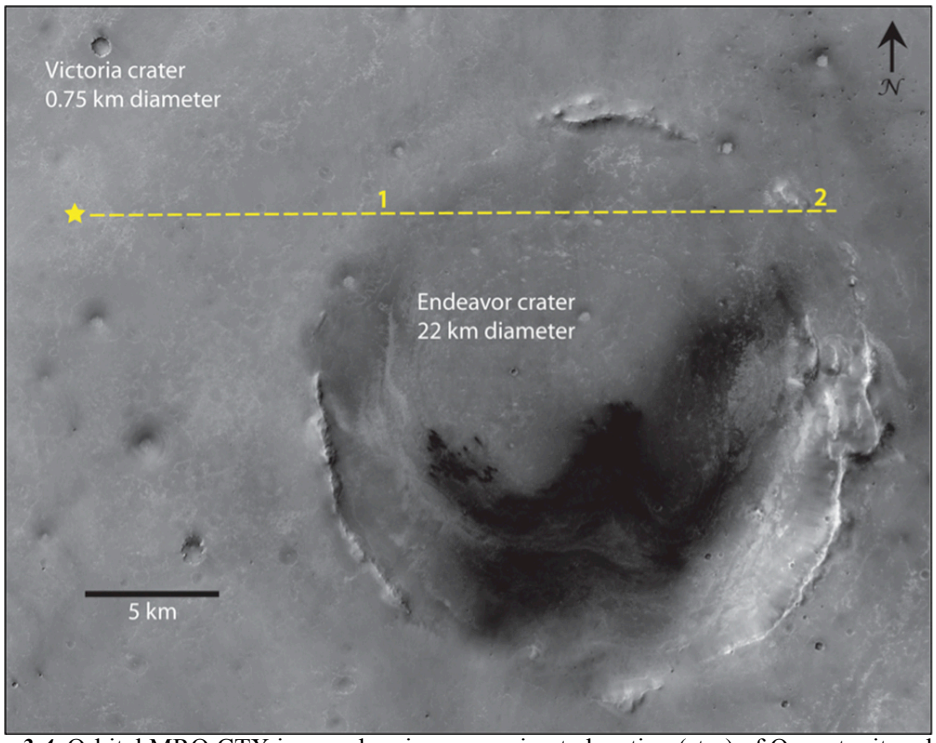

Figure 3.4. Orbital MRO CTX image showing approximate location (star) of Opportunity when it imaged the dust devil and direction the camera was pointed (dotted line) at the time of the observation. Location 1, ~11 km from Opportunity, is the closest distance and location 2, ~27 km from Opportunity, is the farthest distance determined for the location of the dust devil.

The near (western) and far (eastern) Endeavor rims along the line of sight to the dust devil in the Pancam frame (***figure 3.4***, locations 1 and 2) were determined to be the boundaries for the location of the dust devil. Dust devil diameters calculated at 11 km (near rim) and 27 km (far rim) result in 170 m and 410 m diameters, respectively. The smaller diameter falls within the full range of diameters calculated at the Spirit site (2 to 280 m). If the single dust devil imaged at the Opportunity site is located in Endeavor crater and has a diameter within the range observed by Spirit, then it would be between 11 km and 19 km away.

Pathfinder Lander

Three separate studies of dust devils and vortices were conducted at Pathfinder's Ares Vallis site, two of which (Metzger et al., 1999; Ferri et al., 2003) determined the average sizes of detected and imaged dust devils. In the study by Metzger et al. (1999) diameters of five dust devils imaged in optical IMP frames ranged from 14 to 80 m. The IMP images that captured the dust devils were taken at a time when MET data were not collected. The locations of the five dust devils were found in a similar way to those in the Spirit study. Their locations were identified based on their distances to prominent local topographic features. In the study by Ferri et al. (2003) 14 dust devils, including the five found by Metzger et al. (1999), were resolved in IMP images. Dust devil locations and sizes were determined based on results from a geometrical model that assumed all dust devils moved with the ambient wind (a uniform wind of 10 m/s moving toward the NE). Core diameters were determined for 10 of the 14 features and ranged from 11 to 245 m wide with the exception of one very large dust devil

with a diameter of 573 m (Ferri et al., 2003). The 573 m wide dust devil is the largest of all dust devils that have been imaged with surface cameras. The locations of the14 dust devils in the Ferri et al. (2003) study were determined in the same way as at the Spirit site. The locations ranged between 1.5 and 24 km from the lander, with the 573-m diameter dust devil located the farthest distance. Dust devils this large were not imaged in Spirit's cameras but dust plumes up to 1000 m have been imaged from orbit (Thomas and Gierasch, 1985).

Ferri et al. (2003) also detected signatures of 79 vortices by short pressure drops, increases in temperature and a rotating wind vector over period of tens of seconds. The sizes of the vortices were determined based on the duration of their Δ-P as they moved over the Pathfinder pressure sensor and assuming that they also moved with the speed of the ambient wind. The duration of the pressure drop was determined for 19 of the 79 vortices. Pressure drops ranged from 1.1 to 4.9 Pa and lasted between 14 and 51 s. Using the average pressure drop duration of 20 s and assuming that dust devils moved with the ambient wind speed of approximately 10 m/s, the average core diameter was 200 m.

Viking Landers 1 and 2

As stated in Chapter 2, one dust devil detection campaign was carried out using VL-1 data (Ryan and Lucich, 1983) and two studies were conducted using VL-2 data (Ryan and Lucich, 1983; Ringrose et al., 2003). Actual core diameters of vortices detected at the VL sites could not be determined due to the inability to remove the vertical component of the internal wind velocity and lack of knowledge of the precise location of the core center. Therefore all core diameters

represent lower bound values. Core diameters for the 40 vortices detected by VL-1 ranged from 10 to 690 m. Core diameters for the 78 vortices detected by VL-2 in the Ryan and Lucich (1983) study ranged from 10 to 950 m and diameters for the 38 vortices detected by VL-2 in the Ringrose et al. (2003) study ranged from 17 to 450 m. As previously stated, Ryan and Lucich (1983) analyzed a full year of data whereas Ringrose et al. (2003) analyzed only the first 60 sols of activity at the VL-2 site. The range in core diameters derived by Ringrose et al. (2003) were smaller than those determined by Ryan and Lucich (1983) for the period during the summer season that the two data sets overlapped. This may be due to the different methods of detection from the two studies. The core diameters from the Ryan and Lucich (1983) study did not list individual diameters but only provided seasonal ranges. Using these ranges for all 118 vortices detected at both VL sites, the average number density was plotted as a function of core diameter (***figure 3.5***). The results are consistent with the inverse power law relationship of diameter-frequencies produced by the three seasons mapped by Spirit.

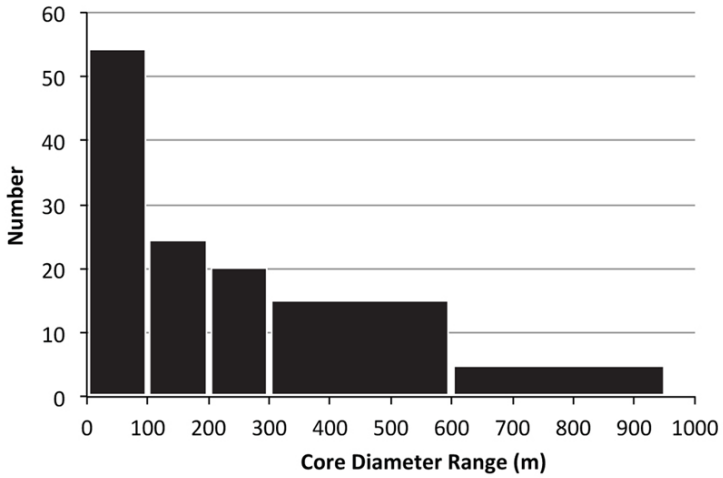

Figure 3.5. Size frequency distribution of vortices detected at both Viking Lander sites. The data were taken from the Ringrose et al. (2003) study.

Visible image studies measure only the visible dusty central column of a passing dust devil, whereas analysis of data from MET instruments detects the full area of disturbance as the vortex passes over the sensors. The disturbed region in a terrestrial vortex has been found to be approximately 10 times the visible core radius (Sinclair, 1973). Therefore, the range of core diameters detected by MET instruments on the Landers can be up to a factor of 10 larger than core as measured in visible camera images. The ratio of the inferred dust devil core to the total disturbed region was verified for a martian vortex detected during the VL-1 and VL-2 vortex study (Ryan and Lucich, 1983). Viking wind vector data were plotted as a function of local time as the vortex passed over the sensors. From the plot, the duration of the total disturbance and the duration of the core passage were determined. Taking the ratio of the duration of the passing core to the duration of the full disturbance, Ryan and Lucich (1983) derived a value very close to one tenth. On Earth the core diameter is sometimes greater than 1/10 the diameter of the disturbance, but always by less than a factor of 2. All martian dust devil diameters imaged in visible data fall within a factor of 10 of the vortices detected with MET data. Therefore, in order to compare diameters measured in all detection campaigns, all diameters derived from vortices were divided by 10 to represent their dust devil equivalent values. ***Table 3.3*** summarizes the ranges of dust devil diameters that have been detected from the six landed spacecraft. ***Figure 3.6*** graphically displays the core diameter ranges. All vortex diameters (highlighted in yellow) are extrapolated to their dust devil equivalent values.

Spacecraft	Dust Devils (#)	Diameters (m) min	median	max	Campaign
Viking 1	40	1	35 *	69	Ryan and Lucich, 1983
Viking 2	78	1	48 *	95	Ryan and Lucich, 1983
Viking 2	38	2	8	45	Ringrose et al., 2003
Pathfinder	4	14	37	80	Metzger et al., 1999
Pathfinder	10	15	115	573	Ferri et al., 2003
Pathfinder	19	-	20 **	-	Ferri et al., 2003
Spirit (S1)	533	2	19	276	Greeley et al., 2006, 2010
Spirit (S2)	101	5	24	124	Greeley et al., 2010
Spirit (S3)	127	5	39	227	Greeley et al., 2010
Opportunity	1	170	-	410	
Phoenix	76	20 **	110 **	200 **	Ellehoj et al., 2010

Table 3.3. Dust devil and vortex diameters from detection campaigns. Diameters highlighted in yellow correspond to detection campaigns that identified vortices from MET data. All vortex diameters (highlighted in yellow) are extrapolated to their dust devil equivalent. A single asterisk (*) denotes averaged diameters calculated from measured min/max values. Double asterisks (**) represent estimated diameters not directly measured.

Figure 3.6. Graphical display of dust devil and vortex diameters listed in Table 3.3. Diameters highlighted in yellow correspond to detection campaigns that identified vortices from MET data. All vortex diameters (highlighted in yellow) are extrapolated to their dust devil equivalent. Median diameters are in red. A single asterisk (*) denotes averaged diameters calculated from measured min/max values. Double asterisks (**) represent estimated diameters not directly measured.

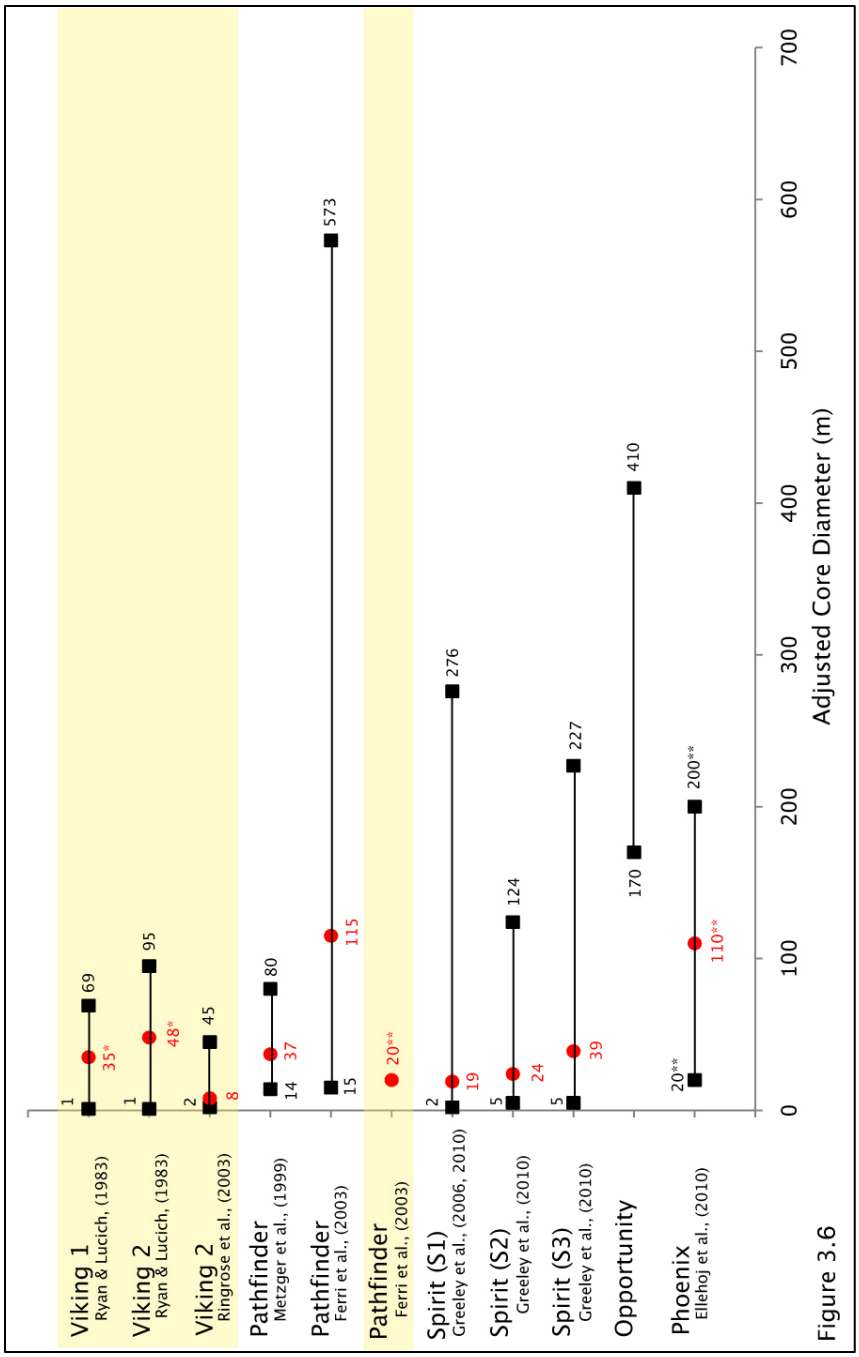

3.4 Dust Devil Speeds

In terrestrial dust devil studies (reviewed by Balme and Greeley, 2006), radial velocities (V) are 5-10 m/s peaking at roughly 20 m/s. Measurements for the total horizontal wind vector (V_h) have been calculated up to 25 m/s. Vertical wind speeds (W) in terrestrial dust devils are typically about a quarter of the peak tangential speed, less than 10 m/s. The results from terrestrial field study (Ryan and Carroll, 1970) that analyzed > 80 dust devils suggest that larger dust devils have greater tangential speeds and therefore typically have greater vertical speeds. Balme and Greeley (2006) conclude that at the center of a dust devil, vertical flow dominates; tangential and vertical flow dominate the dust devil center; just outside the dust devil column, radial and tangential flow dominate; at far distances only a weak radial flow can be detected.

MER Spirit

Assuming that dust devils move roughly with the speed of the ambient winds, dust devil movement can be used to approximate ambient winds speeds and directions. However, because a dust devil is in contact with the surface, the speed at which it moves is believed to be slightly slower than the ambient wind due to drag by surface shear stresses. Speeds of the dust devils imaged at the MER Spirit site were measured by tracking their locations through sequential frames taken within a very short time of each other (Greeley et al., 2006, 2010). The total distance they travelled throughout the frames was then divided by the total time they were observed in sequential frames to estimate an average speed. Speeds for the three seasons that Spirit observed ranged from 0.1 to 27 m/s with

median values 2.5 m/s for Season One, 2.2 m/s for Season Two, 1.5 m/s for Season Three (Greeley et al., 2006, 2010). Vertical velocities were measured based on tracking the location clots of dust through sequential frames in Navcam dust devil sequences. Ranges of vertical velocities for the three seasons range from 0.04 to 17.0 m/s with median values of 1.6 m/s for Season One and 1.0 m/s for Seasons Two and Three.

Viking Landers 1 and 2

To make direct comparisons of speed measured in visible camera sequences of a passing dust devils to those detected by MET wind sensors, measurements of the ambient wind speed just before and after the passage of vortices over MET sensors were compared with wind speeds at the Spirit and Pathfinder sites. At the VL-1 site ambient wind speeds (U_a) ranged from 2 to 12 m/s during the three seasons analyzed (Ryan and Lucich, 1983). Ambient wind speeds averaged 1 to 12 m/s at the VL-2 site (Ryan and Lucich, 1983). The ambient wind speed was generally below 10 m/s (Ringrose et al., 2003) throughout most of the summer season when vortex density was highest. Internal components of the wind vector measured by the MET instruments (tangential, radial and vertical speeds) could not be separated from VL data. The maximum wind speed associated with vortex passage (U_{max}) is an inferred quantity describing the radial and tangential wind components and was not measured directly from MET wind data. The largest ranges for U_{max} occur in the northern winter when ambient wind speeds are largest due to increased dust storm activity associated with perihelion. Six vortices occurred in the dusty period after 1977B

had core diameters of 180 to 580 m and U_{max} speeds between 27 and 44 m/s. These six vortices are assumed to have entrained dust, however, as mentioned in the previous chapter, without further evidence for dust entrainment, there is no way to know for certain that internal speeds are the primary mechanisms for dust entrainment.

Mars Pathfinder Lander

Horizontal speeds for the five dust devils imaged at the Pathfinder site by Metzger et al. (1999) ranged from 0.5 to 4.6 m/s. Average vertical velocities of 7 m/s were used based on terrestrial studies by Sinclair (1966) that assumed that dust devils are in solid rotation. Ferri et al. (2003) used a thermodynamic theory to describe dust devils (Renno et al., 1998, 2000) in which the presence of both convection and a sense of vorticity are necessary to generate vortices. Dust devils were assumed to move with the speed of the ambient wind ~10 m/s. Assuming that vortices are in cyclostrophic balance and the pressure drop determines the magnitude of the tangential wind velocity component, vertical velocity of 20 m/s was derived using an equation by Rennó and Ingersol (1996). These findings agree with past terrestrial results (Sinclair, 1973) indicating that the vertical velocity components can attain magnitudes that approach that of the horizontal component.

MER Opportunity and Phoenix Lander

No velocity information was obtained from the single dust devil imaged in Opportunity's Pancam frame or for the multiple dust devils imaged and inferred at the Phoenix site. An MRAMS mesoscale climate model (Rafkin et al., 2001)

simulated over Opportunity's landing site during the period of EDL (L_s 342º, late southern summer) (***figure 2.17***) predicted erratic convective winds that could reach speeds greater than 10 m/s during daytime hours. The vortex detected at the Phoenix site with the largest pressure drop (Δ-P 3.6 Pa) had tangential wind speeds of 14 m/s (assuming cyclostropic balance within dust devil columns). Midday ambient wind speeds at the Phoenix site ranged from 4 to 10 m/s.

Table 3.4 summarizes the horizontal and vertical speeds that have been detected from the six landed spacecraft. ***Figure 3.7*** is a plot of the horizontal speeds listed in Table 3.4.

Spacecraft	Dust Devils (#)	Horizontal Speed (m/s) min	median	max	Vertical Speed (m/s) min	median	max	Campaign
Viking 1	40	2	7 *	12	-	-	-	Ryan and Lucich, 1983
Viking 2	78	1	6.5 *	12	-	-	-	Ryan and Lucich, 1983
Viking 2	38	4	8	12	-	-	-	Ringrose et al., 2003
Pathfinder	3	0.5	0.8	4.6	-	7**	-	Metzger et al., 1999
Pathfinder	19	-	10**	-	-	20**	-	Ferri et al., 2003
Spirit (S1)	329	0.2	2.5	21.4	0.2	1.6	8.8	Greeley et al., 2006, 2010
Spirit (S2)	66	0.1	2.2	11.2	0.1	1	4.6	Greeley et al., 2010
Spirit (S3)	103	0.1	1.5	26.7	0.3	1	17	Greeley et al., 2010
Opportunity	-	-	-	-	-	-	-	
Phoenix	-	-	-	-	-	-	-	Ellehoj et al., 2010

Table 3.4. Dust devil and vortex speeds from detection campaigns. Speeds highlighted in yellow correspond to detection campaigns that identified vortices from MET data. A single asterisk (*) denotes averaged diameters calculated from measured min/max values. Double asterisks (**) represent estimated speeds not directly measured from detected dust devils.

Figure 3.7. Horizontal speeds from dust devils imaged and detected at several landing sites. Speeds highlighted in yellow correspond to detection campaigns that identified vortices from MET data. Median horizontal speeds are in red. Asterisks (*) indicate values that were averaged from max/min values. Double asterisks (**) represent estimated speeds not directly measured from detected dust devils.

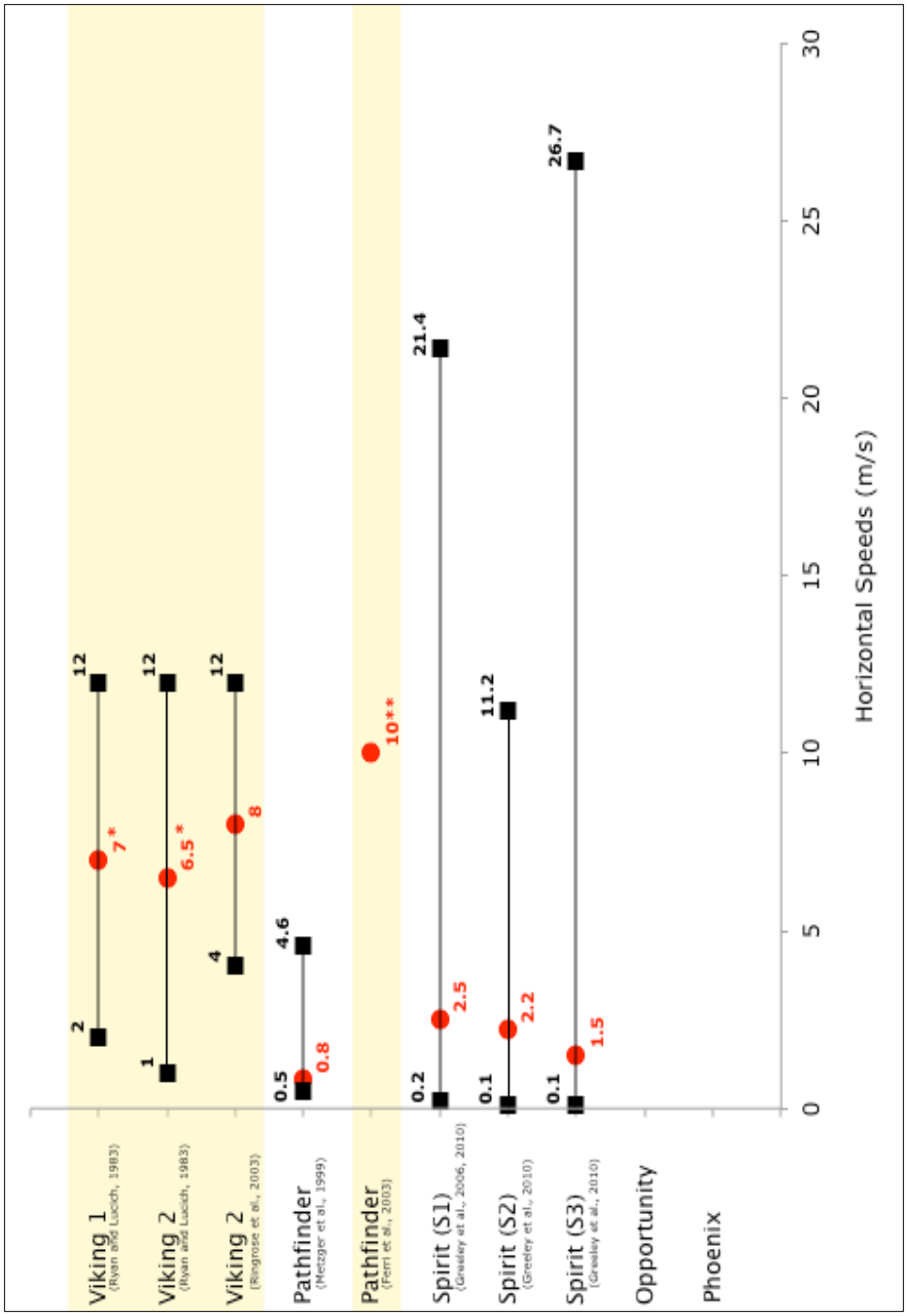

3.5 Diurnal and Seasonal Frequency

Over 70% of the terrestrial dust devils observed formed in the late morning through the early afternoon (Sinclair, 1969; Snow and McClelland, 1990; Mattsson et al., 1993; Metzger, 1999). Results from terrestrial field studies indicated that activity occurred in intense spurts followed by a period with no activity (Sinclair, 1969). It was assumed that the PBL needs time to establish a superadiabatic lapse rate and periods of intense activity may stir up the near-surface environment, requiring sufficient time for the lapse rate to rebuild itself before convection can persist (Sinclair, 1966; Metzger, 1999). Sinclair (1969) found that small dust devils peak in activity earlier than larger ones, reflecting the time necessary for a superadiabatic layer to build.

Dust devils have been imaged with orbital cameras throughout the entire martian year (Cantor et al., 2006) but most were seen in the spring and summer. Insolation-driven activity supports the idea that dust devils are convective. In almost all ground-based dust devil studies in both hemispheres, number frequencies peaked during the warmest times of the day (0900 to 1700 LTST) and during the warm dusty spring and summer seasons. The near-surface thermal gradient is a driving factor in dust devil production, whereas, the absolute ambient temperature is not as significant. Therefore, it seems logical that more dust devil activity would be found at the equatorial landing sites than at higher latitudes because of the larger diurnal temperature gradient during the warm seasons and to peak during the warmest times of day.

MER Spirit

Greeley et al. (2010) noted that all three seasons at the Spirit site began with the onset of southern spring, within 14 sols of L_s 181°. It should be noted that the start of each dust devil season, although initiated very close to the same L_s, occurred progressively later in the season each martian year; L_s 173° for Season One, L_s 181° for Season Two, and L_s 189° for Season Three. It is interesting to note that the shift in the initiation of dust devil season aligns directly with a similar shift in seasonal rover *cleaning events.* A cleaning event is a term used to describe abrupt increases in solar power associated with wind-related events that remove dust from the solar panels. Three major cleaning events were recorded, occurring between late winter (L_s ~170°) and early summer (L_s ~290°) and each was initiated later in the season each martian year (Vaughan et al., 2010; ***figure 3.8***). Although the first of the cleaning events (L_s 173°, between sols 417-420) during Spirit's first spring aligns very closely with the first dust devils imaged during Season One (L_s 173°, sol 421) Vaughan et al., 2010 attributes the cause of this event strong regional wind shear (gusts) rather than interactions with convective vortices.

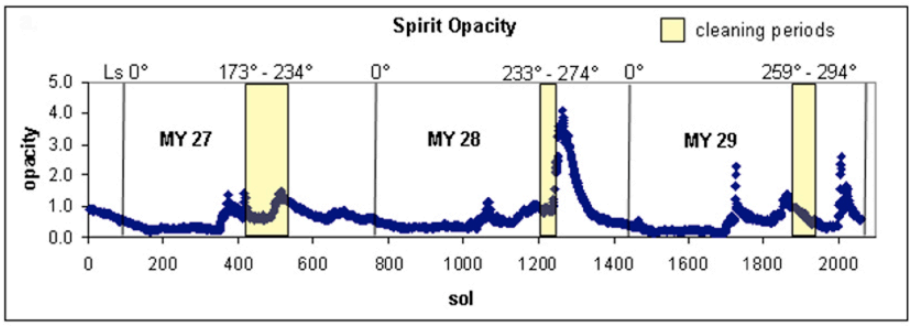

Figure 3.8. Atmospheric dust opacity as a function of sol with the three main periods of cleaning events in yellow; L_s of each block of events is labeled above (from Vaughan et al., 2010)

Dust devil traverses that were mapped onto orbiter images by Greeley et al. (2006, 2010) were oriented on rose diagrams to display the directions of seasonal dust devil movement from the three mapping campaigns (***figure 3.9***). The results reveal inter-seasonal variations in the direction of dust devil movement. Using dust devil movement as a proxy for the direction of ambient wind shear, the rose diagrams can be used to infer the direction of the winds that moved the dust devils across the plains at the time of their observation. During Season One (173º-340º, sols 421-691, MY 27), dust devils generally moved towards the east; the largest number moving towards the NE. During Season Two (181º-267º, sols 1103-1239, MY 28), dust devils moved in a larger range of directions than in Season One. Their directions are generally towards the east with large numbers moving towards the east, SE, and slightly south of west. During Season Three (189º-355º, sols 1785-2058, MY 29), most of the movement was divided between directions toward the NNE and in the opposite direction toward the SSW.

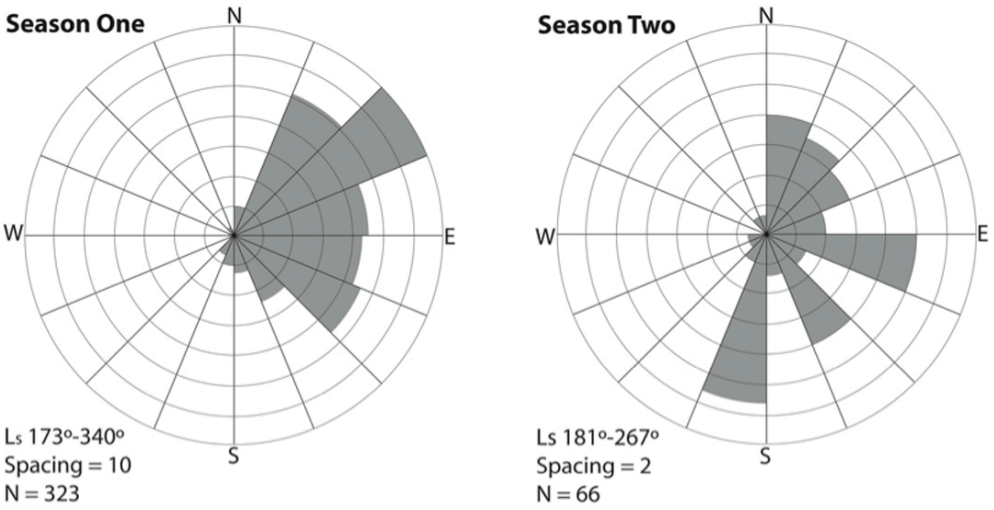

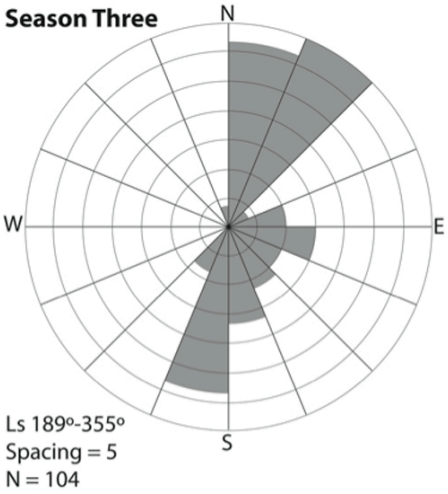

Figure 3.9. Rose diagrams show seasonal trends of dust devil movement at the MER Spirit landing site during the 3 mapping campaigns (Seasons One, Two and Three); the direction of motion is represented by the direction of the gray wedge from center of the diagram out towards the edge; L_s refers to the time of year that the plot spans; the spacing of the concentric circles represents the number of dust devils that moved in a given direction; n refers to the total number of dust devils in each diagram.

To understand large variations in dust devil movement from one season to the next, variations within individual seasons were investigated. ***Figure 3.10*** shows trends in dust devil movement during Season One. The dust devil paths were plotted in rose diagrams divided into four consecutive periods corresponding to patterns of changing dust devil density (DDs/km^2). The density curve for Season One approximates a Gaussian distribution centered about late southern spring. ***Figure 3.10a*** (late southern winter to early southern spring, L_s 173º-230º) corresponds to the period when the dust devil density is very low but steadily increasing. The general trend of dust devil movement was toward the east with most dust devils moving toward the NE. ***Figure 3.10b*** (early to mid southern spring, L_s 230º-251º) corresponds to the period when dust devil density is nearing its maximum. This period corresponds to Mars at perihelion (L_s 250º), when the near-surface temperature gradient is reaching its maximum and near-surface

thermal convection is assumed to be strongest. The trend in dust devil movement continues toward the NE. ***Figure 3.10c*** (mid southern spring to early southern summer, L_s 251º-273º) marks the beginning of the decline in dust devil density even though atmospheric temperatures from daytime solar radiation at the beginning of the southern summer (summer solstice L_s 270º) are at a maximum. The frequency of occurrences decreased monotonically. The near-surface thermal gradient was decreasing and the convective well that fuels dust devil production was weakening. There is a major shift in the direction of dust devil movement during mid spring towards the SE. This roughly 90º change in direction could be a result of changes in the PBL. ***Figure 3.10d*** (early to late southern summer, L_s 273º-340º) corresponds to the period when normalized dust devil production waned. Nearing the end of summer, daytime surface temperatures are relatively low contributing to a very small increasing thermal gradient. This verifies Greeley et al. (2006) that a strong increasing thermal gradient is critical to dust devil formation. Dust devils continued to move toward the SE, until they were so infrequent that the season was determined to be over.

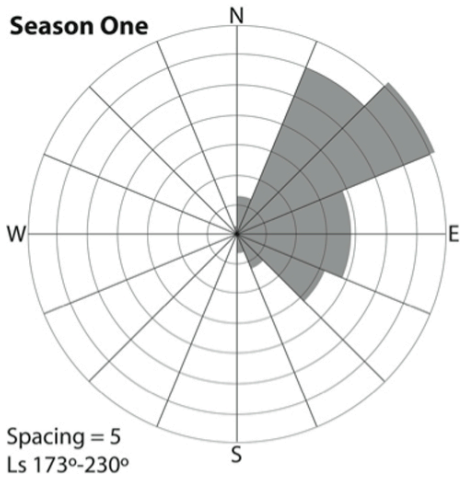

a) Late Winter - Early Spring

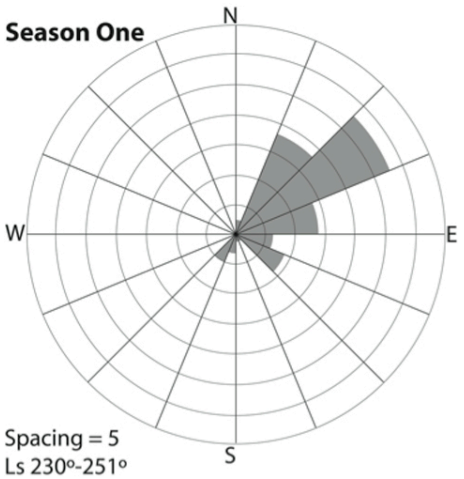

b) Early Spring - Mid Spring

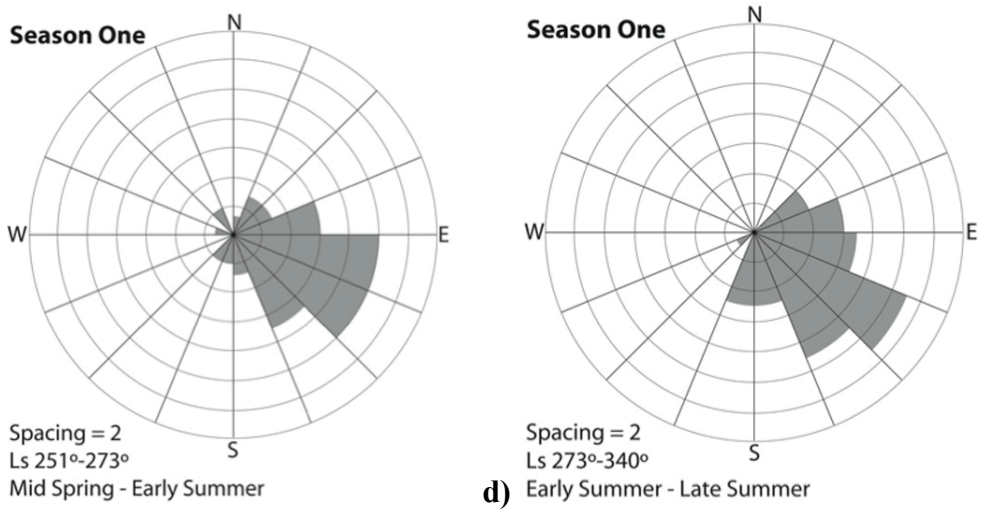

Figure 3.10. Rose diagrams show seasonal trends of dust devil movement at the MER Spirit landing site during Season One. Dust devils were grouped based on patterns in dust devil frequency [See Greeley et al. (2010) Figure 3]; the direction of motion is represented by the direction of the gray wedge from center of the diagram out towards the edge; L_s refers to the time of year that the plot spans; the spacing of the concentric circles represents the number of dust devils that moved in a given direction.

Seasons Two and Three do not follow the same Gaussian density distribution as Season One; therefore, divisions were made somewhat arbitrarily. As described by Greeley et al. (2010), dust devil densities during Season Two showed a gradual increase for about 40 sols, followed by a 10-sol period of very low density, and then about 70 sols of fairly constant frequency, before a final spike in density ends the season. This abrupt halt in activity coincides with the passage of the 2007 dust storm (Greeley et al., 2010). Lack of observed dust devil activity may be due to several factors including systematic imaging at times when dust devils were not active, a lack of available dust for vortices to lift, and/or encountering conditions not conducive to forming an unstable superadiabatic layer. There are significantly fewer dust devils imaged during Season Two as compared to Season One, but the general shape of the density curve in the early spring is similar. ***Figure 3.11a*** (early to mid southern spring, L_s 181º-222º) marks

the start of the season where just as in Season One dust devil density is low but steadily increasing. Dust devils generally trend toward the NE, similar to that seen in Season One, along with some movement toward the SSW. There is much scatter in the movement of dust devils in the second half of spring, as ***figure 3.11b*** (mid to late southern spring, L_s 222º-267º) shows. Some dust devil movement is recorded in almost every direction, with most movement toward the SSW, SE and ESE. Comparing rose diagrams from Season One to Season Two, it is obvious that the general direction of the winds that drive dust devil movement across the plains sometime during the mid spring has shifted from moving towards the NE to moving towards the SE. Dust devil movement in mid to late spring during Season Two shows a more scattered distribution.

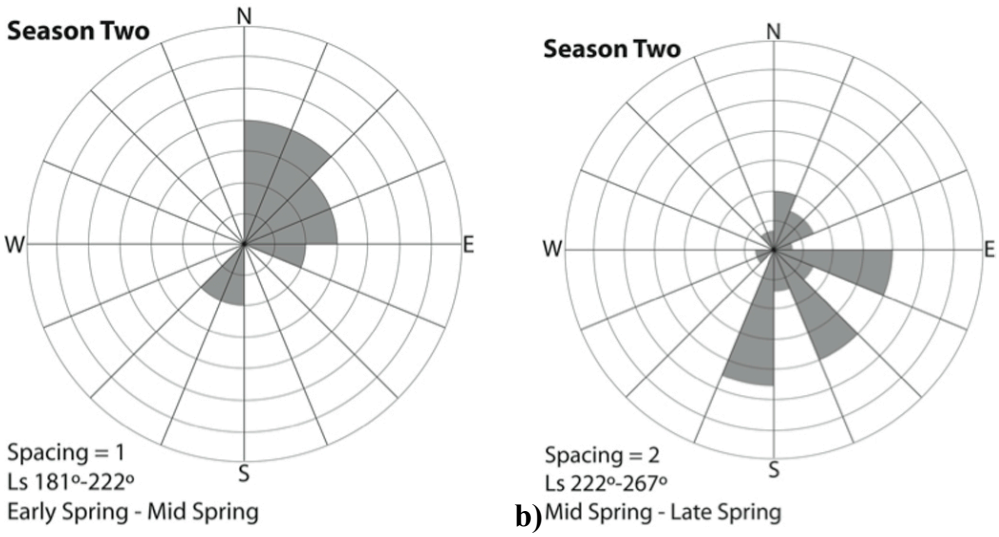

Figure 3.11. Rose diagrams show seasonal trends of dust devil movement at the MER Spirit landing site during Season Two. Dust devils were grouped based on patterns in dust devil frequency [See Greeley et al. (2010) Figure 3]; the direction of motion is represented by the direction of the gray wedge from center of the diagram out towards the edge; L_s refers to the time of year that the plot spans; the spacing of the concentric circles represents the number of dust devils that moved in a given direction.

Dust devil density during Season Three was fairly constant throughout most of the season and exhibited no pronounced peak in activity in late spring like the ones seen in previous seasons. According to Greeley et al. (2010), Season Three is characterized by a gradual increase in activity in the early spring, maintains a fairly constant density well into the late summer (L_s ~323), and then decreases monotonically until the season ends. The season was divided at brief periods of slightly increasing and decreasing density. ***Figure 3.12a*** (early to mid southern spring, L_s 189º-223º) corresponds to the period of gradual increase in activity at the beginning of the season and is similar to what was seen during Seasons One and Two. However, unlike Seasons One and Two when general movement was toward the NE, dust devil movement during this period is mostly toward the north with only some movement toward the NE and SE. As seen in ***figure 3.12b*** (mid southern spring to early southern summer, L_s 223º-275º), a large shift in direction occurs in dust devil movement. However, unlike the shifts seen in Seasons One and to some degree Season Two, during this period when movement is primarily toward the SE, most dust devils during Season Three moved toward the SSW. ***Figure 3.12c*** (early to mid southern summer, L_s 275º-306º) corresponds to the period of highest daytime surface temperatures and a leveling off of the thermal gradient. The directions of dust devil movement are very scattered with the two dominant directions of motion trending toward the NE and toward the SE. Lastly, as Season Three neared its end in the late summer, most dust devils moved towards the NE (***figure 3.12d***; mid to late southern summer, L_s 306º-355º). This is in sharp contrast to the late summer during Season

One when most movement trended SE. It seems that the patterns of seasonal winds changed significantly from Season One to Season Three.

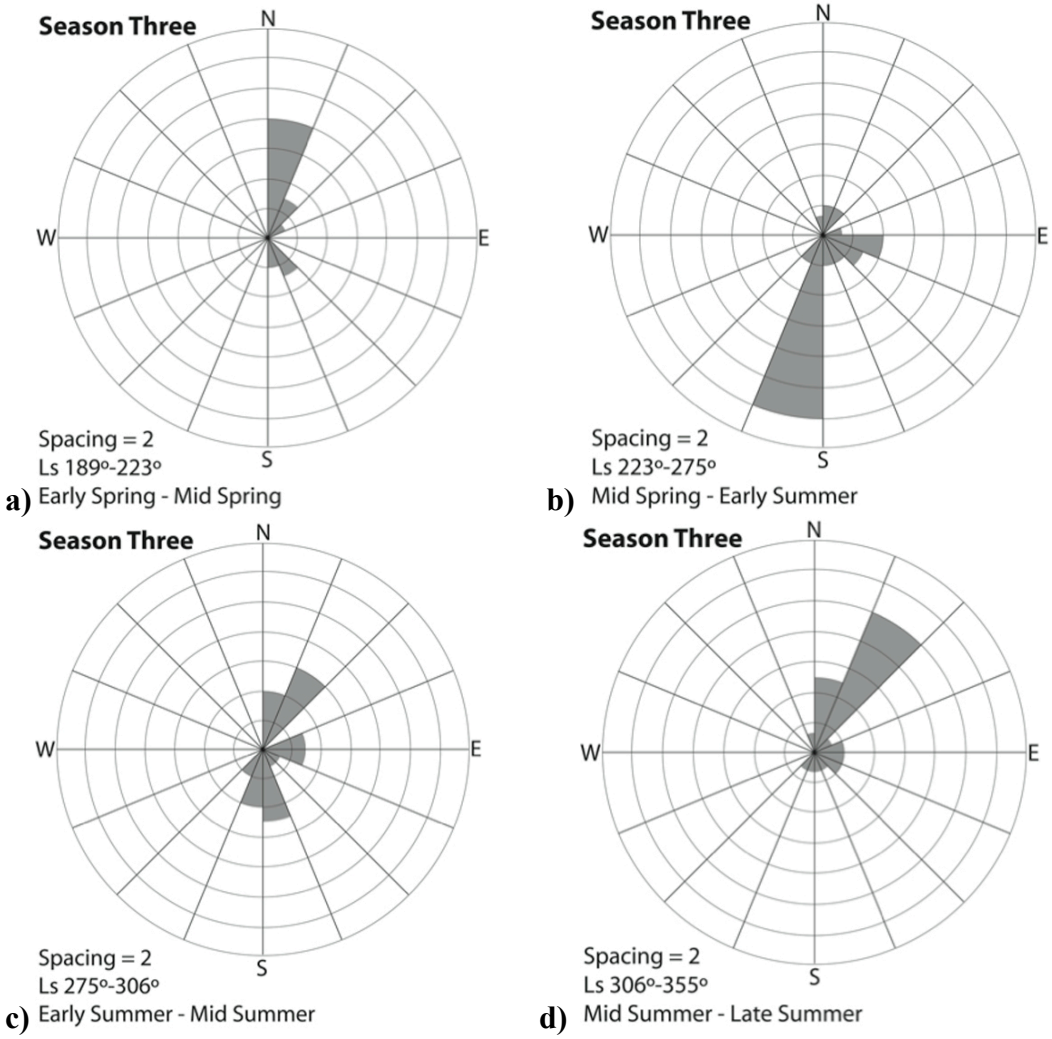

Figure 3.12. Rose diagrams show seasonal trends of dust devil movement at the MER Spirit landing site during Season Three. Dust devils were grouped based on patterns in dust devil frequency [See Greeley et al. (2010) Figure 3]; the direction of motion is represented by the direction of the gray wedge from center of the diagram out towards the edge; L_s refers to the time of year that the plot spans; the spacing of the concentric circles represents the number of dust devils that moved in a given direction.

Viking Landers 1 and 2

The largest vortex densities occurred during the northern summer season and the smallest densities occurred during the winter season at both VL sites

(***table 3.5***). Two of the vortices detected at the VL sites were detected at night on the same sol under very light winds (Ryan and Lucich, 1983). It was assumed that these two events were associated with the lander's acting like a heat island. Ryan and Lucich (1983) did not note the local times over which all the vortex events occurred. However, the 38 vortices detected at the VL-2 site by Ringrose et al. (2003), were detected between 0948-1648, with peaks between 1000-1030 and 1300-1330. The early morning peak was attributed by Ringrose et al. (2003) to lander-generated turbulence because this peak is not seen in terrestrial analog studies documented by Sinclair (1973) or at the MER Spirit site (Greeley et al., 2006, 2010). No vortices were detected immediately following the early afternoon spike in activity at the VL-2 site. Ringrose et al. (2003) recorded the local time that each event occurred, allowing the first frequency distribution of vortices as a function of local time to be constructed from ground-based data. The vortices peaked early in the morning (1000-1030 LST), earlier than those at the Spirit site and no vortices were detected between 1330 and 1400 LST. This is in contrast to terrestrial findings (Sinclair, 1966) when the maximum generally occurs in the afternoon with little activity in the morning.

Table 3.5

	VL-1			VL-2		
	Sols Analyzed (#)	Vortices (#)	Sols with Vortices (%)	Sols Analyzed (#)	Vortices (#)	Sols with Vortices (%)
Summer	15	23	60	55	41	58
Fall	18	12	33	21	7	19
Winter	14	5	36	52	5	8
Spring				23	25	70

Vortices at the Viking 1 and 2 sites; After Ryan and Lucich, 1983

Mars Pathfinder Lander

The 14 dust devils resolved at the Pathfinder site by Ferri et al. (2003), which included the five dust devils found by Metzger et al. (1999), all occurred during the northern summer season between 1116 and 1506 LST. The 79 vortices detected by Murphy and Nelli (2002) and confirmed by Ferri et al. (2003) occurred between 0930 and 1700 LST with peaks in the early afternoon. The 83-sol Pathfinder mission was only able to make measurements at the Ares Vallis site during the spring and summer season so there is no basis to draw conclusions about seasonal density. However, based on data returned from the VL-1 site in Chryse Planitia a couple 100 km to the west, it seems likely that dust devils would peak during the summer seasons at the Pathfinder site as well.

Mars Exploration Rover Opportunity

Most dust devils imaged with optical cameras occurred during the spring and summer seasons. Therefore, it is interesting to note that the Opportunity dust devil was imaged in middle of southern winter, L_s 119º. With only a single data point it is impossible to determine whether this single dust devil represents an outlier not indicative of the other dust devils generated at the Meridiani site, or if the dust devils at the Opportunity site have very different seasonal frequencies compared to the other sites.

Phoenix Mars Lander

The 502 vortices detected at the Phoenix site were occurred about local noon when insolation was strongest (Ellehoj et al., 2010). 29 events were detected during the nighttime hours (between 2100 and 0100 LST) in the first 94 sols (L_s

77º to 120º) at the Phoenix site. However these events were not attributed to passing thermal vortices but were related to air passing over the lander at midnight that passed over the near-by Heimdal crater a couple hours before (Holstein-Rathlou et al., 2010). The sols with the largest peak midday temperatures however, do not correlate with peaks in dust devil activity. Increases in dust devil frequency correspond to a period where the maximum daytime temperatures are starting to decline but when midday near-surface heat fluxes and diurnal temperature ranges are still increasing (Ellehoj et al., 2010).

The initiation of dust devils at the Phoenix site coincided with the formation of volatile condensates, ground fogs, and passing clouds rather than periods of maximum seasonal insolation and thermal gradients (Ellehoj et al., 2010; Holstein-Rathlou et al., 2010). High wind speeds are typically thought to prevent the development of convective cells by disrupting the development of near-surface thermal gradients that are necessary for the formation of convective vortices (Sinclair, 1969; Ryan and Carroll, 1970). General daytime winds were low averaging 4 to 6 m/s throughout the first 60-70 sols (L_s 77º-112º; late northern spring to early northern summer) of the mission and 6-10 m/s during the second half of the mission (after sol 95; L_s 120º early northern summer). This increase in dust devil activity with increased storm events may be a similar mechanism that is seen in the generation of terrestrial gustnados. Gustnados are a colloquial expression for a short-lived, shallow, generally weak, vertically oriented vortex found along a gust front (American Meteorology Society Glossary of Meteorology). They are sometimes generated in association with terrestrial

thunderstorms but have no apparent connection to the storm or overlying clouds. This may imply a completely different formation mechanism at the phoenix site as compared to the other five sites; one driven by passing low- and high-pressure systems not only insolation. All dust devils at the Phoenix site were imaged between 1100 and 1200 LST and between 1300 and 1600 LST. The absence of dust devil activity between 1200 and 1300 LST is most likely due to a period of rebuilding of the superadiabatic lapse rate and thermal gradient.

Figures 3.13 and ***3.14*** compare diurnal and seasonal density, respectively, at each of the six landing sites. It is apparent that all detected dust devils were active during the warmest times of the sol, the majority between 1100 and 1500 LST, and during the warm dusty spring and summer seasons.

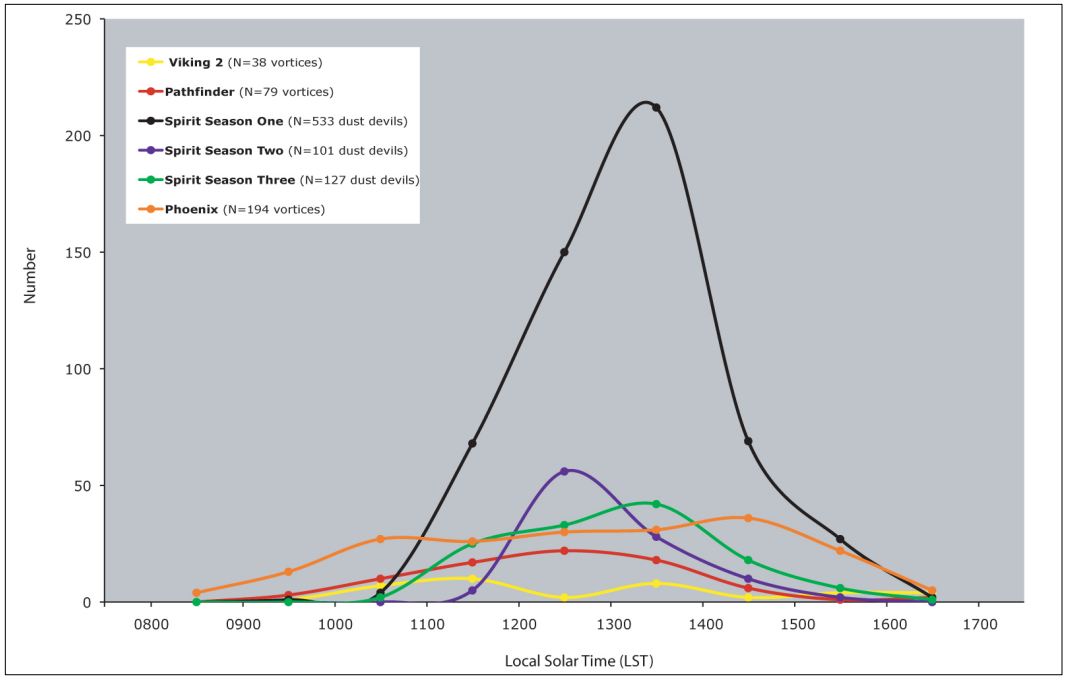

Figure 3.13. Number of dust devils at each site as a function of local time; values are not normalized spatially or temporally.

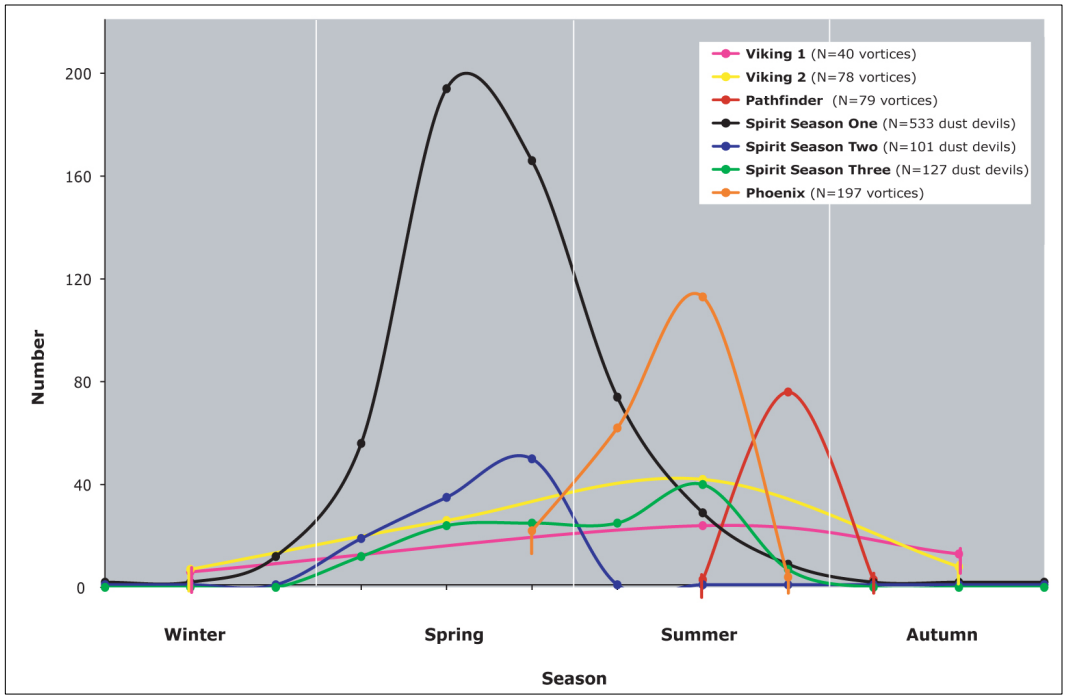

Figure 3.14. Number of dust devils at each site as a function of season; values are not normalized spatially or temporally; the end points of the VL-1 and VL-2 curves represent the end of the dust devil study; the end points of the Pathfinder and Phoenix curves represent the end of the mission; observations were only continuous at the Spirit site.

3.6 Number Frequency

In order to compare dust devils and vortices imaged and detected by the six spacecraft all number frequencies were normalized both spatially and temporally. In order to normalize the number frequencies spatially, the number of dust devils in each study was divided by the *detection area*. In vortex campaigns with MET instruments the detection area is defined as the area surrounding the landers over which the MET sensors could detect a vortex disturbance from normal ambient conditions (***figure 3.15a***). In the optical dust devil campaigns the full detection area is defined as the furthest areal extent to which optical cameras could resolve dust devils (***figure 3.15b***). Detection areas for optical studies were calculated according to the techniques used in the three Spirit dust devil

campaigns (Greeley et al., 2006, 2010). These detection areas were then used to calculate normalized dust devil frequencies.

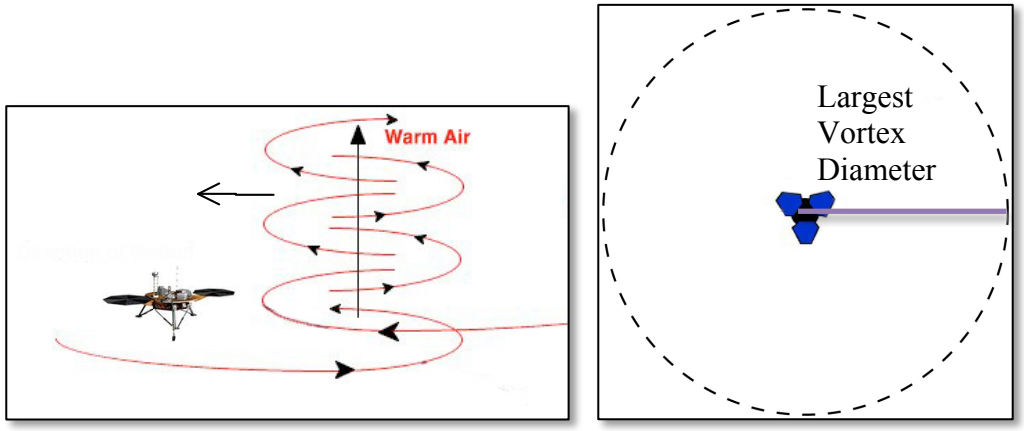

Figure 3.15a. Detection area for vortex studies using MET sensors; see text for description.

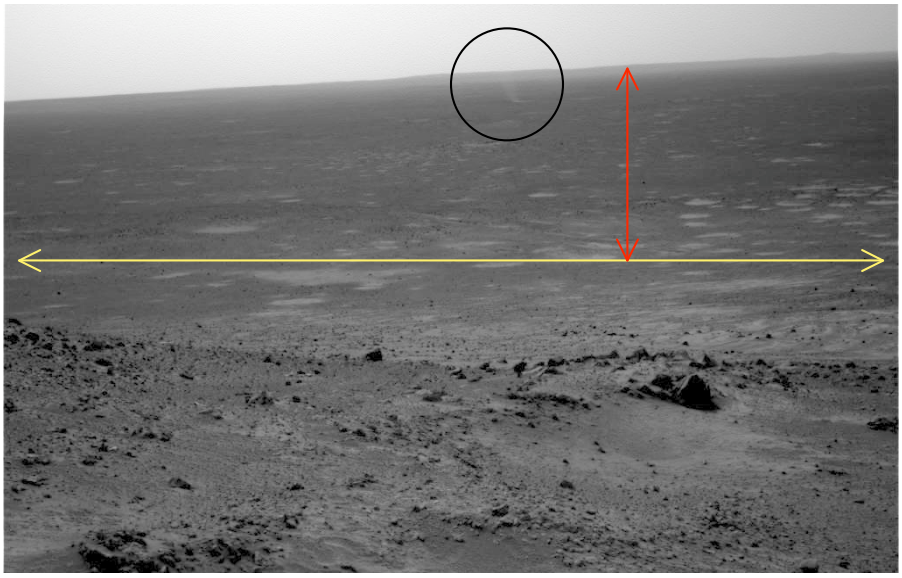

Figure 3.15b. Spirit Navcam frame of detection area for dust devil studies with optical cameras; yellow and red lines represent the extent to which the dust devil (black circle) could be resolved in optical frame.

Seasonal number frequencies derived from landed dust devil studies are listed in ***table 3.6***. The average seasonal number frequency for all seasons where data was available, is ~ 1 dust devils/ km^2/sol. Terrestrial studies have recorded a wide range of number frequencies from less than 1 dust devils/km^2/day to bigger

than 750 dust devils/km^2/day (Sinclair, 1969; Carroll and Ryan, 1970). Seasonal number frequencies at the Spirit site were two orders of magnitude smaller than average at 0.05, 0.02 and 0.03 dust devils/ km^2/sol for Seasons One, Two and Three, respectively. Average detection areas measured for the VL-1 vortices during the northern summer, fall, and winter seasons analyzed are 0.18 km^2, 0.69 km^2, and 1.50 km^2, respectively. Seasonal number frequencies at the Pathfinder site were based on the 2-sol period that dust devils were imaged. There is a large difference in frequency determined from the two Pathfinder detection campaigns of 0.2 dust devils/km^2/sol and 0.004 dust devils/km^2/sol. This is due to the large difference in detection areas derived from each study. Metzger et al. (1999) assumed that the farthest location a dust devil was imaged was 2.2 km, whereas, Ferri et al. (2003) stated that dust devils were imaged as far away as 24 km from the lander. The average number frequency over the three season VL-1 study (Ryan and Lucich, 1983) is 3.2 vortices/km^2/sol. Similarly, average areas of detection calculated at the VL-2 during the northern summer, winter, fall, and spring seasons were 2.84 km^2, 0.02 km^2, 0.58 km^2, and 1.33 km^2, respectively. The average number frequency over the year-long VL-2 study (Ryan and Lucich, 1983) is 5.7 vortices/km^2/sol. Areas of detection and average number frequency calculated for the Ringrose et al. (2003) study are 0.64 km^2 and 1.00 vortices/km^2/sol, respectively.

To take into account bias in spatial and temporal surface imaging for optical studies at the Spirit and Pathfinder sites, extrapolated number frequencies were derived (***table 3.7***). These extrapolated frequencies are calculated using the

inferred number of seasonal dust devils, which is derived assuming all 360º of the detection area were monitored throughout the entire period when dust devils were active at each site. The average extrapolated number frequency over all five optical studies at the Spirit and Pathfinder sites is ~ 19 dust devils/ km^2/sol. There were 51 dust devils/km^2/sol derived in Season One, 11 dust devils/km^2/sol in Season Two and 20 dust devils/km^2/sol in Season Three (Greeley et al., 2010) for the three seasons at the Spirit site. The large decline in frequency from Season One to Season Two is possibly attributed to the passage of the large storm that truncated the second season. Pathfinder's extrapolated number frequencies of 15 dust devils/ km^2/sol and 0.5 dust devils/ km^2/sol are much smaller than average, but fall within an order of magnitude of the values derived for Spirit's dust devils.

Spacecraft	Dust Devils (#)	Detection Area (km^2)	Sols (#)	Seasonal Number Frequency (#/km^2/sol)	Campaign
Viking 1	40	1.5	47	0.6	Ryan and Lucich, 1983
Viking 2	78	2.8	151	0.2	Ryan and Lucich, 1983
Viking 2	38	0.6	60	1	Ringrose et al., 2003
Pathfinder	5	12	2	0.2	Metzger et al., 1999
Pathfinder	13	1811	2	0.004	Ferri et al., 2003
Pathfinder	79	0.1*	83	7	Ferri et al., 2003
Spirit (S1)	533	38	271	0.05	Greeley et al., 2006, 2010
Spirit (S2)	101	28	137	0.03	Greeley et al., 2010
Spirit (S3)	127	28	274	0.02	Greeley et al., 2010
Opportunity	-	-	-	-	
Phoenix	-	-	-	-	

Table 3.6. Seasonal number frequencies derived from dust devil and vortex detection campaigns. Number frequencies highlighted in yellow correspond to detection campaigns that identified vortices from MET data. A single asterisk (*) denotes detection areas derived from estimated diameters. Dashed lines (-) indicate values that cannot be determined from information provided.

Spacecraft	Inferred Dust Devils (#)	Inferred # Dust devils in 669 sols (martian year)	Detection Area (km^2)	Sols (#)	Extrapolated Number Frequency (#/km^2/sol)	Campaign
Viking 1	-	-	-	-	-	Ryan and Lucich, 1983
Viking 2	-	-	-	-	-	Ryan and Lucich, 1983
Viking 2	-	-	-	-	-	Ringrose et al., 2003
Pathfinder	400	123,000	12	2	15	Metzger et al., 1999
Pathfinder	2,000	665,000	1811	2	0.5	Ferri et al., 2003
Pathfinder	-	-	-	-	-	
Spirit (S1)	516,700	1,275,000	38	271	50	Greeley et al., 2006, 2010
Spirit (S2)	40,900	200,000	28	137	11	Greeley et al., 2010
Spirit (S3)	150,000	366,000	28	274	20	Greeley et al., 2010
Opportunity	-	-	-	-	-	
Phoenix	-	-	-	-	-	

Table 3.7. Normalized number frequencies derived from optical dust devil detection campaigns extrapolated spatially and temporally. Number frequencies highlighted in yellow correspond to detection campaigns that identified vortices from MET data. Dashed lines (-) indicate values that cannot be determined from information provided.

3.7 Dust Flux

Dust fluxes were derived from the two visible camera studies at the Pathfinder site and both fall within the ranges calculated for dust devils at the Spirit site. Dust flux is the mass of dust raised by a vortex per unit area per time. Dust fluxes at the Spirit site were calculated based on determination of average dust devil diameters, dust concentration within the vortices, vertical speed of rising dust within the vortices, and the average duration of the dust devils. Average seasonal dust flux ranges at the Spirit site were 4.0×10^{-9} to 4.6×10^{-4} kg/m^2/s during Season One, 5.2×10^{-7} to 6.2×10^{-5} kg/m^2/s during Season Two, and 1.5×10^{-7} to 1.6×10^{-4} kg/m^2/s during Season Three. Seasonal flux values at the Spirit site span up to 5 orders of magnitude.

The dust devils imaged by the Pathfinder IMP have roughly 700 times the dust content of the ambient background (Metzger et al., 1999). The sky near the horizon has a contrast of about 1-4% with concentrated dust devil plumes (Metzger et al., 1999; Ferri et al., 2003). Metzger et al. (1999) estimated the dust concentration across a typical dust devil with 60% the background atmospheric

dust content to be $7x10^{-4}$ kg/m^3. Based on this value, the average dust devil found at the Pathfinder site with a 10-m diameter has an average dust concentration of $7x10^{-5}$ kg/m^3 (Metzger et al., 1999). A vertical dust flux estimate of $5.0x10^{-4}$ kg/m^2/s was determined for the five dust devils imaged at the Pathfinder site based on assumptions determined from terrestrial studies that dust devils have a dust-free core of 50% their outer diameter and average vertical velocities of 7 m/s (Sinclair, 1973; Metzger, 1999). Ferri et al. (2003) applied this information to their calculations and found that for a typical sized dust devil that they detected (~200 m), the corresponding dust content is $3.5x10^{-6}$ kg/m^3. Using average vertical speeds of 20 m/s they obtained an average flux of $7x10^{-5}$ kg/m^2/s an order of magnitude larger than the result given by Metzger et al. (1999). Both values of dust flux derived in the two Pathfinder studies are within the range calculated at the Spirit site.

Terrestrial studies have measured particle fluxes at multiple heights within a dust devil. Fluxes up to ~ $3x10^{-3}$ kg/m^2/s were measured at a heights of ~140 m within terrestrial dust devils (Gillette and Sinclair, 1990). Lidar measurements of dust concentrations have been used to estimate fluxes on the order of ~ $1x10^{-3}$ kg/m^2/s at 100 m above the surface (Renno et al., 2004) and between ~ $0.6x10^{-3}$ kg/m^2/s to $4.4x10^{-3}$ kg/m^2/s in the lower regions of dust devils (Metzger, 1999). These values are an order of magnitude larger than those calculated at the Spirit and Pathfinder sites most likely due to the development of stronger convection on Earth. Dust devils are larger on Mars but are not lifting as much material as their terrestrial counterpart. Laboratory simulations (Neakrase et al., 2004) of dust

devils were used to estimate the rates that they remove dust from the surface and they agree with what was measured in terrestrial field studies ($0.2x10^{-3}$ kg/m^2/s to $5x10^{-3}$ kg/m^2/s).

3.8 Dust Loading

Estimates for dust loading at the Spirit site were extrapolated out to incorporate the Gusev Low Albedo Zone (GLAZ) (Greeley et al., 2006, 2010). GLAZ are the areas within Gusev crater that are dominated by seasonal dust devil tracks. Greeley et al. (2010) sampled the percent coverage of dust devil tracks within GLAZ. It was determined that tracks made up 84% of the GLAZ area (~3000 km^2 area) during Season One, 73% during Season Two, and 59% during Season Three. Dust loading estimates for Spirit's three dust devil seasons were derived from estimates for the total mass of dust injected into the atmosphere each season ($6.6x10^3$ to $7.7x10^8$ kg during Season One, $9.9x10^4$ to $1.2x10^7$ kg during Season Two, and $2.7x10^5$ to $2.8x10^8$ kg during Season Three). Dust loading estimates ranged from $9.5x10^{-3}$ to 1100 kg/km^2/sol during Season One, $3.2x10^{-1}$ to 39 kg/km^2/sol during Season Two, and from $5.5x10^{-1}$ to $5.8x10^2$ kg/km^2/sol during Season Three.

Ringrose et al. (2003) applied the Pathfinder dust concentration estimates to obtain a dust loading estimate for the 6 dust devils inferred from MET data at the VL-2 site. Assuming an average dust concentration within dust devils of $7x10^{-5}$ kg/m^3 (Metzger et al., 1999) and average vertical velocities of 7 m/s, the 6 inferred dust devils raised 800 kg/km^2/sol; a value much larger than at the Spirit site.

CHAPTER 4 DISCUSSION AND PREDICTIONS

4.1 Discussion

Aeolian processes are the primary geological process currently altering the martian surface; however, it is unclear how wind-related processes vary with location. Dust devils, dust-laden convective vortices, are powered by insolation in the presence of atmospheric instability (Sinclair, 1966, 1973; Metzger, 1999). Dust devils were imaged or inferred from meteorological measurements at all six successful Mars landing sites providing a unique opportunity to compare their morphologies, speeds, normalized number frequencies, densities, and dust fluxes. The MER Spirit data are used as the basis of comparison because it is the most extensive data set compiled, spanning 3 martian years (Greeley et al., 2006, 2010). Each landed vehicle had different methods of detecting dust devil activity, making direct comparisons challenging. Therefore, all data were normalized spatially and temporally before making direct comparisons.

In all dust devil studies on Mars and Earth, number frequencies peaked during the warmest times of the day (between 0900 and 1600-1700 LTST) and most were active during the warm dusty spring and summer seasons. Insolation-driven activity supports the idea that dust devils are convective. Terrestrial dust devil activity peaks earlier in the day (1000-1100 LST) than their martian counterparts (1200-1400 LST). Vortices were detected during the night at the Phoenix and Viking Lander sites but were not attributed to turbulence due to near surface thermals, rather turbulent winds generated by interactions with local topography. The single dust devil imaged by Opportunity occurred during mid

southern winter (L_s 119º), which is very uncharacteristic of the other dust devils imaged in optical frames. The Opportunity dust devil may have been generated by thermal eddies that created from convective plumes interacting with the uneven surface of Endeavor crater or represented a dust devil season unlike those at the other landing site. Dust devil activity at the Phoenix landing site intensified with the development and passage of seasonal condensate clouds and storms, possibly indicating a formation mechanism other than from midday insolation. Martian dust devil activity is similar to what was found in terrestrial field studies, periods of intense activity are typically followed by a more quiescent period. This suggests that the dust lifted by dust devils interrupts the adiabatic layer and it must rebuild itself to once again form convective vortices.

Terrestrial dust devils are typically much smaller (typically less than 100 m; Mattsson et al., 1993) than those imaged on Mars. Martian dust devils measured less than 300 m in diameter, with the exception of a single dust devil with a diameter of 573 m imaged at the Pathfinder site (Ferri et al., 2003). Dust devil diameters measured with optical cameras at the Pathfinder, Spirit, and Phoenix sites (Metzger et al., 1999; Ferri et al., 2003; Greeley et al., 2006, 2010; Ellehoj et al., 2010) tend to all be smaller than those derived from the detection of vortices in MET data at the Viking and Pathfinder sites (Ryan and Lucich, 1983; Ringrose et al., 2003; Ferri et al., 2003). Uncertainties in dust devil diameters at the Phoenix site were due to the uncertainty in dust devil locations in the flat arctic plains and were estimated to range from 20 to 200 m, (Ellehoj et al., 2010). The location of the only dust devil imaged by Opportunity was difficult to

constrain making the best estimates for the diameter of the dust devil between 170 and 410 m. Core diameters measured from the detection of vortices in VL-1 MET data range from 10 to 690 m (Ryan and Lucich, 1983) and from 10 to 950 m (Ryan and Lucich, 1983; Ringrose et al., 2003) in VL-2 MET data. However, past terrestrial and martian studies (Sinclair et al., 1973) indicate that typical dust devils display a 1:10 ratio of visible core diameters to the full area of disturbance. All dust devils fall within a factor of 10 of the sizes of vortices.

Horizontal speeds of the dust devils imaged at the Pathfinder, Spirit, and Phoenix sites were measured by tracking their locations through sequential frames taken within a short time of each other. Then the total distance traversed by the dust devils are divided by the amount of time they were observed in images. Because dust devils are in contact with the surface, the speed at which they move is thought to be roughly that of the ambient wind. To make direct comparisons of dust devil speeds measured in visible camera sequences to those detected as vortices move over stationary MET wind sensors, measurements of the ambient wind speed just before and after the passage of vortices over MET sensors were compared with wind speeds at the Spirit and Pathfinder sites. Internal components of the wind vector measured by the MET instruments (tangential, radial and vertical speeds) were ignored. All velocities were within an order of magnitude of each other. The dust devils observed at the Spirit site obtained the highest speeds, but seasonal median values were of the lowest of all dust devils.

In order to normalize number frequencies, the area of dust devil or vortex detection was first derived. Seasonal number frequencies averaged 1 dust

devil/km^2/sol but varied three orders of magnitude for the studies. Number frequencies varied widely for terrestrial studies from < 1 kg/m^2/s to more than 750 kg/m^2/s (Sinclair, 1969; Carroll and Ryan, 1970). Extrapolated number frequencies derived solely for the Pathfinder and Spirit optical campaigns averaged 19 dust devils/km^2/sol and was within an order of magnitude of the values derived from both sites. Dust fluxes were derived for the two visible camera studies of dust devils at the Pathfinder site, and they both fall within the ranges calculated at the Spirit site. Dust fluxes of $5x10^{-4}$ kg/m^2/s and $7x10^{-5}$ kg/m^2/s, are well within the ranges calculated by MER ($4.0x10^{-9}$ to $4.6x10^{-4}$ during Season One, $5.2x10^{-7}$ to $6.2x10^{-5}$ during Season Two and $1.5x10^{-7}$ to $1.6x10^{-4}$ during Season Three (Greeley et al., 2006, 2010), although they fall on the larger end of the Spirit flux range. Terrestrial flux values were an order of magnitude larger than those derived for martian dust devils, possibly due to the development of stronger convection on Earth.

4.2 Mars Science Laboratory

The Mars Science Laboratory (MSL) *Curiosity* is a roving spacecraft that will assess the habitability of the near-surface martian environment when it arrives in August 2012. Mission goals include analyzing the lower atmosphere and surface geology to seek clues as to whether the landing site was, or perhaps still is a habitable environment. The MSL mission will utilize new technology to lower Curiosity to the surface including a powered *sky crane* descent stage. The rover is equipped with a suite of instruments that will allow in-depth analysis of the local geology, atmosphere, and potential biosignatures in the soil and rocks.

Like the Viking Landers before it, Curiosity is equipped with a nuclear battery that will provide power to the rover by converting the heat produced from decay of plutonium isotopes into electricity. This Multi-Mission Radioisotope Thermoelectric Generator (MMRTG) will allow the 900 kg vehicle to operate continuously for a full martian year (about 23 months).

Curiosity's payload includes optical cameras and MET instruments that will be necessary for dust devil detection (***figure 4.1***). Curiosity's main optical camera is the Mast Camera (Mastcam), an RSM-mounted (roughly 2 m above the surface) panoramic, stereoscopic camera, is capable of taking color images and high-definition video (10 frames/sec). One of the Mastcam cameras has a moderate-resolution lens while the other has high-resolution capability to study the surroundings very far from the rover. Its primary function will be to observe the martian terrain and support driving and sampling activities. It will also systematically measure the concentration of condensed volatiles in the lower atmosphere and dust aerosol optical depth. The Mastcam electronics system processes images and video independently of the rover's main computer and has capability of storing thousands of images and several hours of video footage until the data can be downlinked.

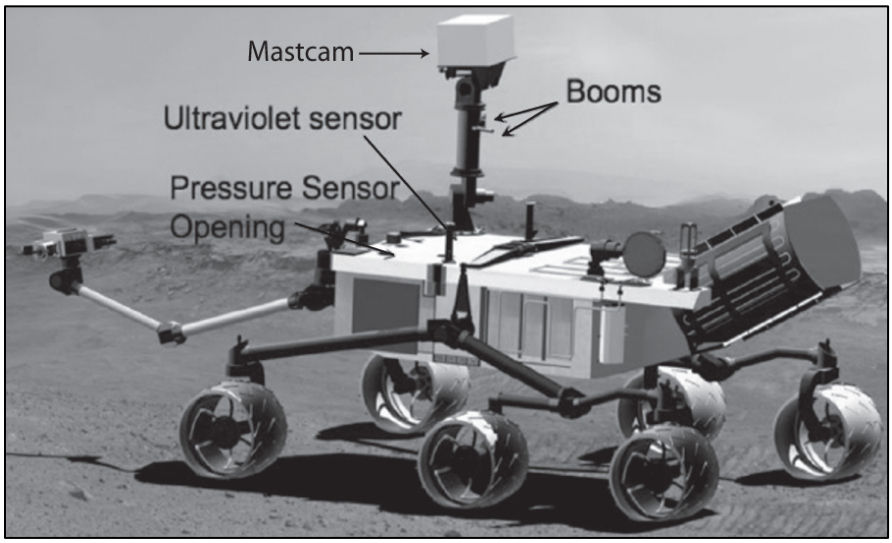

Figure 4.1. Schematic of the Mars Science Laboratory Curiosity with locations of optical camera and MET instruments; from Gomez-Elvira and REMS Team, 2008

Curiosity will be the fifth landed spacecraft equipped with a suite of MET instruments capable of monitoring diurnal weather patterns. Curiosity's payload includes the Rover Environmental Monitoring Station (REMS), a weather station designed by Spain's Centro de Astrobiología. REMS will record six main parameters: wind velocity, pressure, relative humidity, air and ground temperature, and ultraviolet (UV) radiation (Gómez-Elvira et al., 2008, 2009). REMS instruments are housed in four separate units: boom 1 and 2, the UV Sensor (UVS) module, and the Instrument Control Unit (ICU). The booms are mounted 120º to each other on the Remote Sensing Mast (RSM) approximately 1.5 m above the surface (with a 50 mm height difference between them), the UVS is on the top of the rover deck, and the ICU is located within the rover body. Boom 1 is oriented in the rover driving direction and contains one set of wind sensors, the relative humidity sensor, and the air temperature sensor. Boom 2 points to the side of the rover and contains another set of wind sensors, the ground

temperature sensor, and another air temperature sensor. Each set of wind sensors consists of three two-dimensional hot-film anemometers capable of measuring the horizontal and vertical wind speed with 1 m/s accuracy for wind speeds between 0-70 m/s and 0-10 m/s, respectively. Wind direction has an accuracy of 30º. Ground and air temperature is recorded with thermocouples over the range 150 and 300 K with accuracies of 10 K and 5 K, respectively. The ICU houses the ambient pressure sensor and is exposed to the atmosphere via an inlet tube. The pressure sensor measures the ambient pressure in the range 1-1150 Pa. REMS will operate systematically and independent of MSL's other remote sensing activities. The MET sensors will record atmospheric fluctuations every hour each sol for 5 minutes at a sampling rate of 1 Hz for all sensors. The REMS instruments can perform independent of all other rover operations, day and night, whether the rover is asleep or awake.

4.2.1 Dust Devil Detection Campaign

The dust devil detection campaign at the MSL site should be carried out systematically with consistent temporal and spatial sampling of the plains surrounding the rover. The plains surrounding MSL should be imaged multiple times a sol intermittent with Mastcam movies sequences. Sampling should be consistent throughout the day to avoid bias. Thorough imaging of the plains in front of the horizon should be a priority to increase the chances of resolving a dust devil. Image frames can be subframed about the horizon to conserve resources. An autonomous detection algorithm should be implemented into tactical plans make more efficient use of the rover's hard drive space and power. All imaged

should be taken with full color and at 4 bits per pixel to ensure good spatial resolution. Ideally all images should be scanned for presence of dust devil and information on that image frame should be recorded for statistical analysis. A dust devil "movie" sequence similar to the one implemented into Spirit's tactical plans (Greeley et al., 2006, 2010) should be run daily as an alternate sequence to the Mastcam movie sequences. A 21-frame quarter-frame Navcam sequence centered just above the horizon was generated for detection at the Spirit site. The movie sequence used 16.7 Mbits of total data volume and typically ran for 30-40 min. These movie sequences will provide more data for the dust devil detection campaigns at the MSL site and will be used as contingency data if the Mastcam video camera is temporarily not operational or if resources are limited. Coordinated detection activities with the Mastcam and the REMS instruments should be carried out often to ensure simultaneous detection of dust devils that pass very near to the rover.

The following parameters should be recorded for each dust devil imaged and vortex detected at the MSL site:

Table 4.1

Dust Devil Imaging - Mastcam		Vortex Detection - REMS
Preliminary Information		***Preliminary Information***
Sequence Identification Number		Mission Day (sol)
Type of Sequence Run		Local Time of Observation (LST)
Dust Devil Imaged (yes/no)		Solar Longitude (L_s)
Mission Day (sol)		Total Duration of MET Observation (sec)
Local Time of Observation (LST)		Simultaneous Mastcam imaging (yes/no)
Solar Longitude (L_s)		
Simultaneous MET Detection (yes/no)		***Measurements Just Before/After Vortex Passage***
		Average Ambient Pressure (Pa)
Measured Parameters		Average Ambient Temperature (K)
Morphology (V-shaped, columnar etc.)		Average Ambient Wind Speed (m s^{-1})
Tilt Direction (cardinal direction)		Average Ambient Wind Direction (º)
Duration of Activity (sec)		
Diameter (pixels)		***Measurements Associated with Vortex Passage***
Height (pixels)		Pressure Drop (Pa)
Distance Travelled (m)		Duration of Pressure Drop (sec)
Distance from Rover (m)		Temperature Increase (K)
Direction of Motion (cardinal direction)		Duration of Temperature Increase (sec)
Rotation Direction (cw/ccw)		Wind Speed Increase (m s^{-1})
Generation of Track (yes/no)		Shift in Wind Direction (º)
		Duration of Total Disturbance (sec)
Derived Parameters		Duration of Core Passage (sec)
Diameter (m)		Rotation Direction (cw/ccw)
Height (m)		Vortex Tangential Speed (m s^{-1})
Horizontal Speed (m s^{-1})		Vortex Radial Speed (m s^{-1})
Vertical Speed (m s^{-1})		Vortex Vertical Speed (m s^{-1})
Dust Devil Mass (kg)		Core Diameter (m)
Dust Density/Concentration (kg m^{-3})		
Dust Flux (kg m^{-2} s^{-1})		

4.2.2 Candidate Landing Sites and Predictions

Four candidate sites for Mars Science Laboratory (***figure 4.2***):

(1) Holden crater (26.37ºS, 325.16ºE, -2177 m) is a 145-km diameter impact basin in Margaritifer Terra that contains layered sediments with traces of phyllosilicate minerals deposited during periods of sustained aqueous activity (Grant et al., 2008).

(2) Eberswalde crater (23.86ºS, 326.73ºE, -1435 m) is a degraded shallow impact basin located immediately to the SW of Holden crater (Scott and

Tanaka, 1986). The Eberswalde delta system is composed of multiple eroded sinuous distributaries and is interpreted as the remains of a fan delta associated with an ancient lacustrine system (Pondrelli et al., 2008).

(3) Gale crater (4.49°S, 137.42°E, -4444 m) is a 150-km wide impact crater located at the boundary of the northern lowlands and southern highlands in Elysium Planitia. The crater is thought to have contained a standing body of water in the past (Cabrol et al., 1999; Malin and Edgett, 2002). A massive 5-km high terraced sedimentary structure with small exposures of phyllosilicates and sulfate minerals is located in the center of the crater.

(4) Mawrth Vallis (23.99ºN, 341.03ºE, -2245 m) is part of an ancient outflow channel complex in the northern martian tropics just west of Arabia Terra on the border of the northern lowland and southern highland terrain. It is characterized by an ancient channel probably carved by catastrophic floods and contains the largest exposures of phyllosilicates detected on Mars (Poulet et al., 2005).

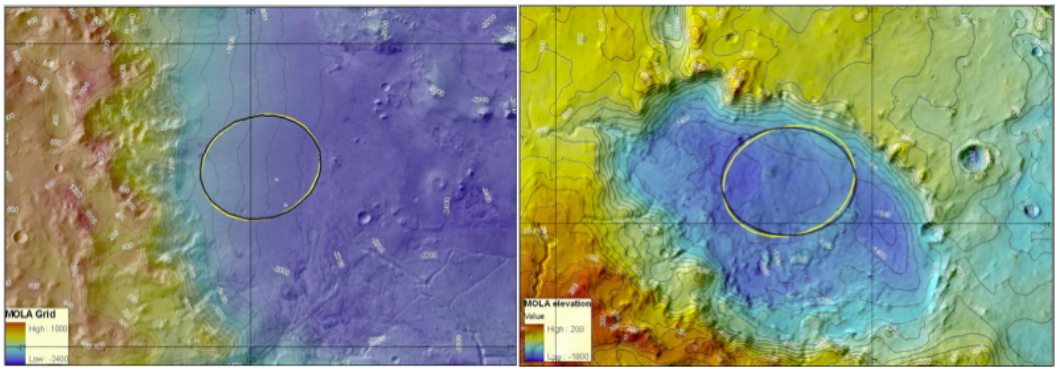

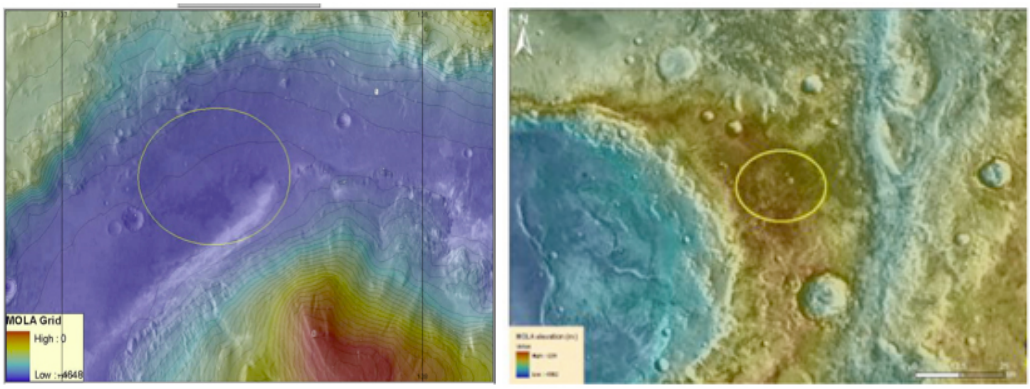

Figure 4.2. Mars Orbiter Laser Altimeter elevation maps of four candidate landing sites proposed for the 2011 Mars Science Laboratory; CW from top left: Holden, Eberswalde, Gale, Mawrth.

The four candidate sites are all in regions with complex topography and meteorological complexity (Rafkin and Rothchild, 2011). With the exception of very dusty surfaces within the Gale crater landing ellipse, the candidate sites are generally dust-free (Rogers and Bandfield, 2009). Holden crater, Mawrth vallis, and Eberswalde crater have relatively low dust cover compared to Spirit's site in Gusev crater, the VL-1 landing site in Chryse Planitia, and the VL-2 landing site in Utopia Planitia. Even if loose surface dust is unavailable for the formation of visible dust devil columns, convective vortices may still persist at each site. Atmospheric modeling studies are necessary to make predictions about pressure, temperature and winds near the surface. Preliminary results from MRAMS models simulated for each candidate site reveal that overall circulation patterns are repeatable and controlled by local topography (Rafkin and Rothchild, 2011). Rock abundance at the four candidate sites was determined from direct optical imaging using HiRISE and determined from IRTM and TES thermal inertia (Golombek et al., 2010). ***Figure 4.3*** compares these values to those determined for the previous six missions. Direct measurements in HiRISE images and

detection from IRTM thermal data show relatively low rock abundances at all four candidate sites (~ 10%).

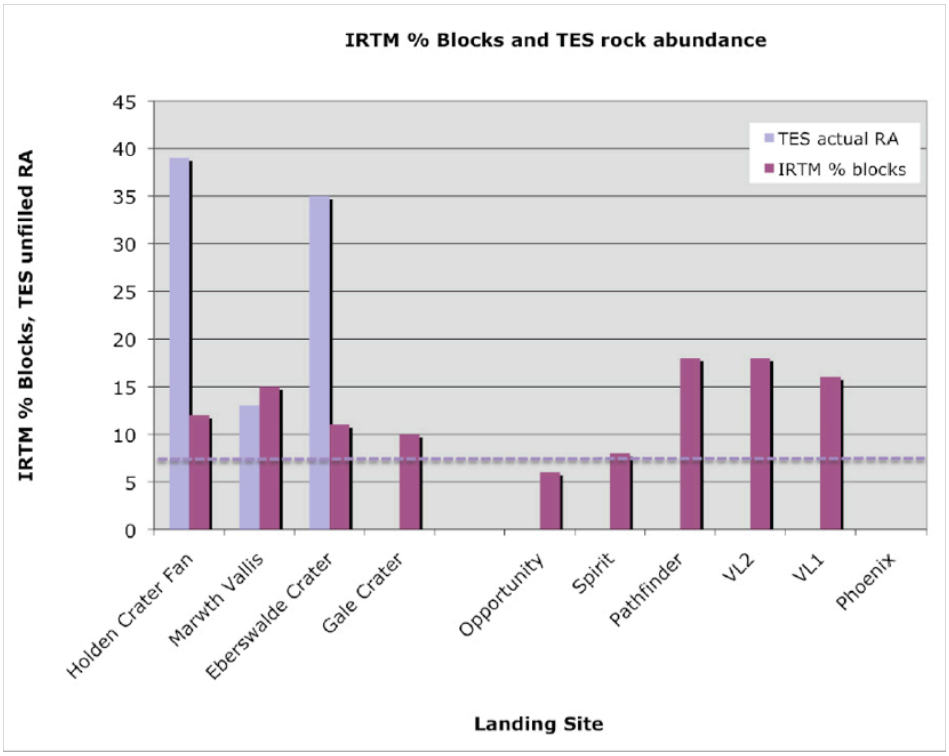

Figure 4.3. Rock abundance at six past spacecraft sites and four MSL candidate landing sites based on IRTM and TES thermal inertia; dotted line at 7% rock abundance represents a ~ 1% chance of encountering a rock more than 0.6 m high and 1.2 m wide; high rock abundance at potential MSL sites based on TES thermal inertia is attributed to detection of exposed outcrop; from Golombek et al., 2010.

All four of the candidate sites have low albedo surfaces. Lower albedo surfaces generally absorb more incident radiation and heat more quickly than high albedo terrains. This may be aid in the generation of dust devils that are driven by very rapid surface heating and large near-surface thermal gradients. Eberswalde and Holden craters are in the southern hemisphere (23-26 ºS) and will provide the first weather measurements at that latitude on Mars. These sites experience much colder diurnal temperatures as compared to Gale crater and Mawrth vallis. There is evidence from circulation models that wind speeds and ambient pressures are

influenced by regional storm activity. Orbital comparisons of dust devil track formation in Russell crater in the higher more temperate midlatitudes (53.3ºS, 12.9ºE) to tracks in Gusev crater indicate that there may be a delay in the initiation and peak activity with the more southerly site (Verba et al., 2010). Therefore, if dust devils and vortices are generated at the Eberswalde and Holden sites then the frequency and behavior of dust devil activity may be similar to that observed at the Phoenix site. Dust devil activity may be enhanced by storm activity and initiated much later in the warm dusty season when compared to the other sites.

All things considered, Gale crater has the most potential for dust devil activity of all MSL candidate sites.

REFERENCES

Anderson, D.L., W.F. Miller, G.V. Latham, Y. Nakamura, M.N. Toksoz, A.M. Dainty, F.K. Duennebier, A.R. Lazarewicz, R.L. Kovach, and T.C.D. Knight (1977), Seismology on Mars, *J. Geophys. Res., 82*, 28, 4524-4546.

Arvidson, R.E. (1974), Wind-blown streaks, splotches, and associated craters on Mars: Statistical analysis of Mariner 9 Photographs, *Icarus, 21*, 12-17.

Arvidson, R.E., R. Anderson, P. Bartlett, J. Bell, D. Blaney, P. Christensen, P. Chu, L. Crumpler, K. Davis, B.L. Ehlmann, R. Fergason, M. P. Golombek, S. Gorevan, J. Grant, R. Greeley, E. Guinness, A. F. C. Haldemann, K. Herkenhoff, J. Johnson, G. Landis, R. Li, R. Lindemann, H. McSween, D.W. Ming, T. Myrick, L. Richter, F.P. Seelos, S. W. Squyres, R. Sullivan, A. Wang, J. Wilson (2004), Localization and physical properties experiments conducted by Spirit at Gusev crater, Science, 305, 821-824.

Arvidson, R.E., F. Poulet, R. V. Morris, J.-P. Bibring, J. F. Bell III, S. W. Squyres, P. R. Christensen, G. Bellucci, B. Gondet, B. L. Ehlmann, W. H. Farrand, R. L. Fergason, M. Golombek, J. L. Griffes, J. Grotzinger, E. A. Guinness, K. E. Herkenhoff, J. R. Johnson, G. Klingelhöfer, Y. Langevin, D. Ming, K. Seelos, R. J. Sullivan, J. G. Ward, S. M. Wiseman, M. Wolff. (2006), Nature and origin of the Hematite-bearing plains of Terra Meridiani based on analyses of orbital and Mars Exploration Rover data sets, *J. Geophys. Res., 111*, E12S08, doi:10.1029/2006JE002728.

Arvidson, R.E., S. W. Ruff, R. V. Morris, D. W. Ming, L. S. Crumpler, A. S. Yen, S. W. Squyres, R. J. Sullivan, J. F. Bell III, N. A. Cabrol, B. C. Clark, W. H. Farrand, R. Gellert, R. Greenberger, J. A. Grant, E. A. Guinness, K. E. Herkenhoff, J. A. Hurowitz, J. R. Johnson, G. Klingelho¨fer, K. W. Lewis, R. Li, T. J. McCoy, J. Moersch, H. Y. McSween, S. L. Murchie, M. Schmidt, C. Schro¨der, A. Wang, S. Wiseman, M. B. Madsen, W. Goetz, and S. M. McLennan (2008), Spirit Mars Rover Mission to the Columbia Hills, Gusev Crater: Mission overview and selection results from the Cumerland Ridge to Home Plate, *J. Geophys. Res., 113*, E12S33, doi:10.1029/2008JE 003183.

Bagnold, R.A. (1941), The Physics of Blown Sand and Desert Dunes, Methuen, London.

Balme, M.R., P.L. Whelley and R. Greeley (2003), Mars: Dust devil track survey in Argyre Planitia and Hellas Basin, *J. Geophys. Res., 108*, 5086, doi:10.1029/2003JE002096.

Balme, M.R. and R. Greeley (2006), Dust devils on Earth and Mars, *Rev. Geophys., 44*, RG3003, doi:10.1029/2005RG000188.

Bell, J.F., III, S.W. Squyres, K.E. Herkenhoff, J.N. Maki, H.M. Arneson, D. Brown, S.A. Collins, A. Dingizian, S.T. Elliot, E.C. Hagerott, A.G. Hayes, M.J. Johnson, J.R. Johnson, J. Joseph, K. Kinch, M.T. Lemmon, R.V. Morris, L. Scherr, M. Schwochert, M.K. Shepard, G.H. Smith, J.N. Sohl-Dickstein, R.J. Sullivan, W.T. Sullivan, and M.

Wadsworth (2003), Mars Exploration Rover Athena Panoramic Camera (Pancam) investigation, J. Geophys. Res., 108, E12, 8063, doi:10.1029/2003JE002070.

Binder, A.B., R.E. Arvidson, E.A. Guinness, K.L. Jones, E.C. Morris, T.A. Mutch, D.C. Pieri, and C. Sagan (1977), The Geology of the Viking Lander 1 Site, J. Geophys. Res., 82, 28, 4439-4451, doi:10.1029/JS082i028p04439.

Bridges, N.T., R. Greeley, A.F.C. Haldemann, K.E. Herkenhoff, M. Kraft, T.J. Parker, and A.W. Ward (1999) Ventifacts at the Pathfinder landing site, *J. Geophys. Res., 104*, E4, 8595-8615, doi:10.1029/98JE02550.

Brooks, H.B. (1960), Rotation of dust devils, *J. Meteorol., 17*, 84-86.

Cabrol, N.A., and E.A. Grin (1999), Distribution, classification, and ages of Martian impact crater lakes, *Icarus, 142*, 1, 160-172.

Cabrol, N.A., E.A. Grin, M.H. Carr, B. Sutter, J.M. Moore, J.D. Farmer, R. Greeley, R.O. Kuzmin, D.J. DesMarais, M.G. Kramer, H. Newsom, C. Barber, I. Thorsos, K.L. Tanaka, N.G. Barlow, D.A. Fike, M.L. Urquhart, B. Grigsby, F.D. Grant, and O. de Goursac (2003), Exploring Gusev Crater with Spirit: Review of science objectives and testable hypotheses, *J. Geophys. Res., 108*, E12, 8076

Cantor, B.A., P.B. James, M. Caplinger and M.J. Wolff (2001), Martian Dust Storms: 1999 Mars Orbiter Camera Observations. *J. Geophys. Res., 106*, E10, doi:10.1029/2000JE001310.

Cantor, B.A., M. Malin and K.S Edgett (2002), Multiyear Mars Orbiter Camera (MOC) observations of repeated Martian weather phenomena during the northern summer season, *J. Geophys. Res., 107*, E3, 5014, doi:10.1029/2001JE001588.

Cantor, B.A., K.M. Kanak and K.S. Edgett (2006), Mars Orbiter Camera observations of Martian dust devils and their tracks (September 1997 to January 2006) and evaluation of theoretical vortex models, *J. Geophys. Res., 111*, doi:10.1029/2006JE002700.

Carr, M.H., R. Greeley, K.R. Blasius, J.E. Guest, and J.B. Murray (1977), Some Martian volcanic features as viewed from the Viking Orbiters, *J. Geophys. Res., 82*, 28, 3985-4015, doi:10.1029/JS082i028p03985.

Carroll, J.J. and J.A. Ryan (1970), Atmospheric vorticity and dust devil rotation, *J. Geophys. Res., 75*, 5179-5184.

Chamberlain, T.E., H.L. Cole, R.G. Dutton, G.C. Greene and J.E. Tillman (1976), Atmospheric measurments on Mars: The Viking meteorology experiment, *Am. Met. Soc. Bulletin, 57*, 1094-1104.

Christensen, P.R. (1982), Martian dust mantling and surface composition: Interpretation of thermophysical properties, *J. Geophys. Res., 87*, 9985-9998.

Christensen, P.R. (1986), The spatial distribution of rocks on Mars, *Icarus, 68*, 2, 217-238.

Christensen, P.R., and H.J. Moore (1992) in Mars (eds Kieffer, H.H. et al.) 686-727, Univ. Ariz. Press, Tucson.

Christensen, P.R., et al. (2000) Detection of crystalline hematite mineralization on Mars by the Thermal Emission Spectrometer: Evidence for near-surface water, *J. Geophys. Res., 105*, 9623-9642.

Christensen, P.R., G.L. Mehall, S.H. Silverman, S. Anwar, G. Cannon, N. Gorelick, R. Kheen, T. Tourville, D. Bates, S. Ferry, T. Fortuna, J. Jeffryes, W. O'Donnell, R. Peralta, T. Wolverton, D. Blaney, R. Denise, J. Rademacher, R.V. Morris, and S. Squyres (2003), Miniature Thermal Emission Spectrometer for the Mars Exploration Rovers, *J. Geophys. Res., 108*, E12, 8064, doi:10.1029/2003JE002117.

Christensen, P.R., et al. (2004), Initial results from the Mini-TES experiment in Gusev crater from the Spirit rover, *Science, 305*, 5685, 824-826.

Christensen, P.R. et al., (2004b), Mineralogy at Meridiani Planum from the Mini-TES Experiment on the Opportunity rover, Science, 306, 5702, 1733-1739.

Crisp, J.A., M. Adler, J.R. Matijevic, S.W. Squyres, R.E. Arvidson, and D.M. Kass (2003), Mars Exploration Rover mission, *J. Geophys. Res., 108*, E12, 8061, doi:10.1029/2002JE002038.

Davy, R., J. A. Davis, P. A. Taylor, C. F. Lange, W. Weng, J. Whiteway, and H. P. Gunnlaugson (2010), Initial analysis of air temperature and related data from the Phoenix MET station and their use in estimating turbulent heat fluxes, *J. Geophys. Res.*, 115, E00E13, doi:10.1029/2009JE003444

Drake, N.B., L.K. Tamppari, R.D. Baker, B.A. Cantor, and A.S. Hale (2006), Dust devil tracks and wind streaks in the North Polar Region of Mars: A study of the 2007 Phoenix Mars Lander sites, *Geophys. Res. Lett., 33*, L19S02, doi:10.1029/2006GL026270.

Ellehoj, M.D. et al. (2010), Convective vortices and dust devils at the Phoenix Mars mission landing site, *J. Geophys. Res., 115*, E00E16, doi:10.1029/2009JE003413.

Ferri, F., P.H. Smith, M.T. Lemmon and N.O. Renno (2003), Dust devils as observed by Mars Pathfinder, *J. Geophys. Res., 108*, E12, 5133, doi:10.1029/2000JE001421.

Fisher, J.A., M.I. Richardson, C.E. Newman, M.A. Szwast, C. Graf, S. Basu, S.P. Ewald, A.D. Toigo, and R.J. Wilson (2005), A survey of Martian dust devil activity using Mars Global Surveyor Mars Orbiter Camera images, *J. Geophys. Res., 110*, E03004, doi:10.1029/2003JE002165.

Gellert, R., R. Rieder, R.C. Anderson, J. Bruckner, B.C. Clark, G. Dreibus, T. Economou, G. Klingelhofer, G.W. Lugmair, D.W. Ming, S.W. Squyres, C. d'Uston, H. Wanke, A. Yen, and J. Zipfel (2004), Chemistry of rocks and soils in Gusev crater from the Alpha Particle X-ray Spectrometer, Science, 305, 5685, 829-832

Gierasch, P.J. and R.M. Goody (1973), A model of a Martian great dust storm, *J. Atmos. Sci., 30*, 169-179.

Golombek, M.P. et al. (1997), Selection of the Mars Pathfinder landing site, *J. Geophys. Res., 102*, 3967-3988.

Golombek, M.P., R.A. Cook, T. Economou, W.M. Folkner, A.F.C. Haldemann, P.H. Kallemeyn, J.M. Knudesen, R.M. Manning, H.J. Moore, T.J. Parker, R. Rieder, J.T. Schofield, P.H. Smith, and R.M. Vaughan (1997), Overview of the Mars Pathfinder Mission and Assessment of Landing Site Predictions, *Science, 278*, 5344, 1743-1748.

Golombek, M.P., N. Bridges (1999), Erosion rates on Mars and implications for climate change: constraints from the Pathfinder landing site, J. *Geophys. Res., 105*, E1, 1841-1853, doi:10.1029/1999JE001043.

Golombek, M.P., J.A. Grant, T.J. Parker, D.M. Kass, J.A. Crisp, S.W. Squyres, A.F.C. Haldemann, M. Adler, W.J. Lee, N.T. Bridges, R.E. Arvidson, M.H. Carr, R.L. Kirk, P.C. Knocke, R.B. Roncoli, C.M. Weitz, J.T. Schofield, R.W. Zurek, P.R. Christensen, R.L. Fergason, F.S., Anderson, and J.W. Rice, Jr., (2003), Selection of the Mars Exploration Rover landing sites, J. Geophys. Res. 108, 8072, 48, doi:10.1029/2003JE002074.

Golombek, M.P., R.E. Arvidson, J.F. Bell, III, P.R. Christensen, J.A. Crisp, L.S. Crumpler, B.L. Ehlmann, R.L. Fergason, J.A. Grant, R. Greeley, A.F.C. Haldemann, D.M. Kass, T.J. Parker, J.T. Schofield, S.W. Squyres, and R.W. Zurek (2005), Assessment of Mars Exploration Rover landing site predictions, *Nature, 436*, 44-48.

Golombek, M. P., J. A. Grant, L. S. Crumpler, R. Greeley, R. E. Arvidson, J. F. Bell III, C. M. Weitz, R. Sullivan, P. R. Christensen, L. A. Soderblom, and S. W. Squyres (2006), Erosion rates at the Mars Exploration Rover landing sites and long-term climate change on Mars, J. Geophys. Res., 111, E12S10, doi:10.1029/2006JE002754

Golombek, M., K. Robinson, A. McEwen, N. Bridges, B. Ivanov, L. Tornabene, and R. Sullivan (2010), Constraints on ripple migration at Meridiani Planum from Opportunity and HiRISE observations of fresh craters, J. Geophys. Res., 115, E00F08, doi:10.1029/2010JE003628.

Golombek, M., Grant, J., Vasavada, A. R., Grotzinger, J., Watkins, M., Kipp, D., Noe Dobrea, E., Griffes, J., and Parker, T. (2011), Final four landing sites for the Mars Science Laboratory (expanded abstract): 42nd Lunar and Planetary Science, Abstract #1520

Gómez-Elvira, J., and the REMS Team (2008), Environmental Monitoring Station for Mars Science Laboratory, Third International Workshop on the Mars Atmosphere: Modeling and observations, held November 10-13, 2008 in Williamsburg, VA, 1447, p. 9052.

Gómez-Elvira, J., L. Castañer, A. Lepinette, J.Moreno, J. Polko, E. Sebastian, J. Torres, M.P. Zorzano and REMS Team (2009), REMS, an instrument for Mars Science

Laboratory rover, 40th Lunar and Planetary Science, Abstract #1540

Grant, J.A. et al. (2004) Surficial geology at the Columbia Memorial Station, Gusev crater, Mars, *Science, 305*, 807-810.

Grant, J. A., S. A. Wilson, B. A. Cohen, M. P. Golombek, P. E. Geissler, R. J. Sullivan, R. L. Kirk, and T. J. Parker (2008), Degradation of Victoria crater, Mars, J. Geophys. Res., 113, E11010, doi:10.1029/2008JE003155.

Grant, J. A., and T. J. Parker (2002), Drainage evolution in the Margaritifer Sinus region, Mars, *J. Geophys. Res.*, 107(E9), 5066, doi:10.1029/2001JE001678.

Greeley, R., B.R. White, J.B. Pollack, J.D. Iverson, and R.N. Leach (1977), Dust storms on Mars: Considerations and simulations, *NASA TM*-78423.

Greeley, R., R. Leach, B.R. White, J.D. Iversen and J.B. Pollack (1980), Threshold windspeeds for sand on Mars: Wind tunnel simulations, *Geophys. Res. Lett., 7*, 2, 121-124.

Greeley, R. (2002), Saltation impact as a means for raising dust on Mars, *Plan. Space Sci. 50*, 2, 151-155, doi:10.1016/S0032-0633

Greeley, R. and J.E. Guest (1987) Geologic map of the eastern equatorial region of Mars, U.S. Depart. Of the Interior, USGS

Greeley, R. and J.D. Iversen (1985), Wind as a geological process on Earth, Mars, Venus and Titan, Cambridge Univ. Press

Greeley, R., and S. D. Thompson (2003), Mars: Aeolian features and wind predictions at the Terra Meridiani and Isidis Planitia potential Mars Exploration Rover landing sites, *J. Geophys. Res.*, 108(E12), 8093, doi:10.1029/2003JE002110

Greeley, R., M. Kraft, R. Sullivan, G. Wilson, N. Bridges, K. Herkenhoff, R.O. Kuzmin, M. Malin, and W. Ward (1999), Aeolian features and processes at the Mars Pathfinder landing site, *J. Geophys. Res., 104*, E4, 8573-8584, doi:10.1029/98JE02553.

Greeley, R., M.R. Balme, J.D. Iversen, S.M. Metzger, R. Mickelson, J. Phoreman and B.R. White (2003), Martian dust devils: Laboratory simulations of particle threshold, *J. Geophys. Res., 108*, E5, 5041, doi:10.1029/2002JE001987.

Greeley, R., S.W. Squyres, R.E. Arvidson, P. Bartlett, J.F. Bell III, D. Blaney, N.A. Cabrol, J. Farmer, B. Farrand, M.P. Golombek, S.P. Gorevan, J.A. Grant, A.F.C. Haldemann, K.E. Herkenhoff, J. Johnson, G. Landis, M.B. Madsen, S.M. McLennan, J. Moersch, J.W. Rice Jr., L. Richter, S. Ruff, R.J. Sullivan, S.D. Thompson, A. Wang, C.M. Weitz, P. Whelley and the Athena Science Team (2004), Wind-Related Processes Detected by the Spirit Rover at Gusev Crater, Mars, *Science, 305*, 5685, 810-813.

Greeley, R., B. H. Foing, H. Y. McSween Jr., G. Neukum, P. Pinet, M. van Kan, S. C. Werner, D. A. Williams, and T. E. Zegers (2005), Fluid lava flows in Gusev crater,

Mars, J. Geophys. Res., 110, E05008, doi:10.1029/2005JE002401.

Greeley, R., P.L. Whelley, R.E. Arvidson, N.A. Cabrol, D.J. Foley, B.J. Franklin, P.G. Geissler, M.P. Golombek, R.O. Kuzmin, G.A. Landis, M.T. Lemmon, L.D.V. Neakrase, S.W. Squyres and S.D. Thompson (2006), Active dust devils in Gusev crater, mars: Observations from the Mars Exploration Rover Spirit, *J. Geophys. Res., 111*, E12S09, doi:10.1029/2006JE002743.

Greeley, R, R.E. Arvidson, P.W. Barlett, D Blaney, N.A Cabrol, P.R. Christensen, R.L. Fergason, M.P. Golombek, G.A. Landis, M.T. lemmon, S.M. McLennan, J.N. Maki, T. Michaels, J.E. Moersch, L.D.V. Neakrase, S.C.R. Rafkin, L. Richter, S. W. Squryes, P.A. de Souza Jr., R.J. Sullivan, S.D. Thompson, and P.L. Whelley (2006b), Gusev crater: Wind-related features and processes observed by the Mars Exploration Rover Spirit, *J. Geophys. Res. 111*, E02S09, doi: 10.1029/2005JE002491.

Greeley, R., D.A. Waller, N.A. Cabrol, G.A. Landis, M.T. Lemmon, L.D.V. Neakrase, M.P. Hoffer, S.D. Thompson, P.L. Whelley (2010), Gusev crater, Mars: Observations of three dust devil seasons, *J. Geophys. Res., 115*, E00F02, doi:10.1029/2010JE003608.

Gunnlaugsson, H.P., C. Holstein-Rathlou, J.P. Merrison, S. Knak Jensen, C.F. Lange, S.E. Larsen, M.B. Madsen, P. Nørnberg, H. Bechtold, E. Hald, J.J. Iversen, P. Lange, F. Lykkegaard, F. Rander, M. Lemmon, N. Renno, P. Taylor, P. Smith (2008), Telltale wind indicator for the Mars Phoenix lander, *J. Geophys. Res., 113*, E00A04, doi:10.1029/2007JE003008.

Haberle R.M., J.B. Pollack, J.R. Barnes, R.W. Zurek, C.B., Leovy, J.R. Murphy, H. Lee and J. Schaeffer (1993), Mars atmospheric dynamics as simulated by the NASA Ames General Circulation Model 1. The zonal-mean circulation. *J. Geophys. Res., 98*, E2, doi:10.1029/92JE02946.

Haberle, R. M., C. P. McKay, J. Schaeffer, N. A. Cabrol, E. A. Grin, A. P. Zent, and R. Quinn (2001), On the possibility of liquid water on present-day Mars, *J. Geophys. Res.*, 106, 23,317–23,326, doi:10.1029/2000JE001360.

Heet, T. L., R. E. Arvidson, S. C. Cull, M. T. Mellon, and K. D. Seelos (2009), Geomorphic and geologic settings of the Phoenix Lander mission landing site, *J. Geophys. Res.*, 114, E00E04, doi:10.1029/2009JE003416

Hess, S.L., R.M. Henry, C.B. Leovy, J.A. Ryan, J.E. Tillman, T.E. Chamberlain, H.L. Cole, R.G. Dutton, G.C. Greene, W.E. Simon, and J.L. Mitchell (1976), Preliminary Meteorological Results on Mars from the Viking 1 Lander, *Science, 193*, 4255, 788-791.

Hess, S.L., R.M. Henry, C.B. Leovy, J.A. Ryan, and J.E. Tillman (1977), Meteorology Results From the Surface of Mars: Viking 1 and 2, *J. Geophys. Res., 82*, 28, 4559-4574, doi:10.1029/JS082i028p04559.

Holstein-Rathlou, C., et al. (2010), Winds at the Phoenix landing site, *J. Geophys. Res.*, 115, E00E18, doi:10.1029/2009JE003411

Huck F.O., G.R. Taylor, H.F. McCall, and W.R. Patterson (1975) The Viking Mars lander camera, *Space Sci. Instru*, vol. 1, 189-241.

Hynek B.M. and R.J. Phillips (2001), Evidence for extensive denudation of the Martian highlands, *Geology, 29*, 5, 407-410.

Hynek, B. M., R. E. Arvidson, and R. J. Phillips (2002), Geologic setting and origin of Terra Meridiani hematite deposit on Mars, *J. Geophys. Res., 107*,E10, 5088, doi:10.1029/2002JE001891

Iversen, J.D., J.B. Pollack, R. Greeley and B.R. White, (1976), Saltation threshold on Mars: The effect of interparticle force, surface roughness, and low atmosphere density, *Icarus, 29*, 381-393.

Iversen, J.D. and B.R. White (1982), Saltation threshold on Earth, Mars and Venus, *Sedimentology, 29*, 111-119.

Jerolmack, D. J., D. Mohrig, J. P. Grotzinger, D. A. Fike, and W. A. Watters (2006), Spatial grain size sorting in eolian ripples and estimation of wind conditions on planetary surfaces: Application to Meridiani Planum, Mars, J. Geophys. Res., 111, E12S02, doi:10.1029/2005JE002544

Kahn, R.A., T.Z. Martin, and R.W. Zurek (1992), The Martian dust cycle, In Mar, edited by Kieffer, HH. Et al., pp. 1017-1053, University of Arizona Press, Tuscon.

Kass, D.M., T. Scholfield, T.I. Michaels, S.C. Rafkin, M.I. Richardson, and A.D. Toigo (2003), Analysis of atmospheric mesoscale models for entry, descent, and landing, *J. Geophys. Res., 108*, E9, 8090-8101.

Kieffer, H. H., S. C. Chase Jr., E. Miner, G. Münch, and G. Neugebauer (1973), Preliminary Report on Infrared Radiometric Measurements from the Mariner 9 Spacecraft, *J. Geophys. Res.*, 78(20), 4291–4312, doi:10.1029/JB078i020p04291

Kieffer, H.H., T.Z. Martin, A.R. Peterfreund, B.M. Jakosky, E.D. Miner, and F.D. Palluconi (1977), Thermal and albedo mapping of Mars during the Viking primary mission, *J. Geophys. Res., 82*, 4249-4290.

Lemmon, M.T., P. Smith, C. Shinohara, R. Tanner, P. Woida, A Shaw, J. Hughes, R. Reynolds, R. Woida, J. Penegor, C. Oquest, S.F. Hviid, M.B. Madsen, M. Olsen, K. Leer, L. Drube, R.V. Morris, D. Britt (2008) The Phoenix Surface Stereo Imager (SSI) Investigation, LPSC XXXIX, 2156.

Leovy, C.B. (1979), Martian meteorology, *Ann. Rev. Astrom. Astrophys., 17*, 387-413.

Leovy, C.B. and R.W. Zurek (1979), Thermal tides and Martian dust storms: Direct evidence for coupling, *J. Geophys. Res., 84*, B6, 2956-2968.

Lowell, P. (1906), Mars and its Canals, London: Macmillan & Co. LTD.

Maki, J.N., J.F. Bell III, K.E. Herkenhoff, S.W. Squyres, A. Kiely, M. Klimesh, M. Schwochert, T. Litwin, R. Willson, A. Johnson, M. Maimone, E. Baumgartner, A. Collins, M. Wadsworth, S.T. Elliot, A. Dingizian, D. Brown, E.C. Hagerott, L. Scherr, R. Deen, D. Alexander, and J. Lorre (2003), Mars Exploration Rover Engineering Cameras, *J. Geophys. Res., 108*, E12, 8071, doi:10.1029/2003JE002077.

Malin, M.C. et al. (2008), Climate, weather, and north polar observations from the Mars Reconnaissance Orbiter Mars Color Orbiter, *Icarus, 194*, 2, 501-512.

Mattsson, J.O., T. Nihlen and W. Yue (1993), Observations of dust devils in a semi-arid district of southern Tunisia, *Weather, 48*, 359-363.

McGinnigle, J.B. (1966), Dust whirls in north-west Libya, *Weather, 21*, 272-276.

McSween, H.Y. et al. (2004), Basaltic rocks analyzed by the Spirit rover in Gusev crater, *Science, 305*, 5685, 842-845.

Mellon, M.T., B.M. Jakosky, H.H. Kieffer, and P.R. Christensen (2000), High-resolution thermal inertia mapping from the Mars Global Surveyor Thermal Emission Spectrometer, *Icarus, 148*, 437-455

Metzger, S.M. (1999), Dust devils as aeolian transport mechanisms in southern Nevada and in the Mars Pathfinder landing site, Ph.D. thesis, Univ. of Nev., Reno.

Metzger, S.M., J.R. Carr, J.R. Johnson, T.J. Parker, and M.T. Lemmon (1999), Dust devil vortices seen by the Mars Pathfinder camera, *Geophys. Res. Lett., 26*, 2781-2784.

Moore, H.J., R.E. Hutton, R.F. Scott, C.R. Spitzer, and R.W. Shorthill (1977), surface Materials of the Viking Landing Sites, *J. Geophys. Res., 82*, 28, 4497-4523, doi:10.1029/JS082i028p04497.

Moore, J.M., A.D. Howard, W.E. Dietrich, and P.M. Schenk (2003), Martian layered fluvial deposits: Implications for Noachian climate scenarios, *Geophys. Res. Letts., 30*, 24, 2292.

Moore, J.M. and A.D. Howard (2005), Large alluvial fans on Mars, *J. Geophys. Res., 110*, E04005.

Moores, J.E., M.T. Lemmon, P.H. Smith, L. Komguem, and J.A. Whiteway (2010), Atmospheric dynamics at the Phoenix landing site as seen by the Surface Stereo Imager, *J. Geophys. Res., 115*, E00E08, doi:10.1029/2009JE003409.

Murphy, J.R. and S. Nelli (2002), Mars Pathfinder convective vortices: Frequency of occurrence, *Geophys. Res. Lett., 29*, 23, 2103, doi:10.1029/2002GL015214.

Mutch, T.A., R.E. Arvidson, J.W. Head, III, K.L, Jones, R.S. Saunders (1976), The geology of Mars, N.J., Princeton Univ. Press

Mutch, T.A., R.E. Arvidson, A.B. Binder, E.A. Guinness, and E.C. Morris (1977), The Geology of the Viking Lander 2 site, *J. Geophys. Res., 82*, 28, 4452-4467, doi:10.1029/JS082i028p04452.

Neakrase, L.D.V. (2009), A laboratory study of sediment flux within dust devils on Earth and Mars, Ph.D. thesis, Ariz. State Univ

Neugebauer, G., G. Munch, H. Kieffer, S.C. Chase Jr., and E. Miner (1971), Mariner 1969 Infrared Radiometer Results: Temperatures and Thermal Properties of the Martian Surface, *The Astron. J., 76*, 8.

Nowicki, S. A., and P. R. Christensen (2007), Rock abundance on Mars from the Thermal Emission Spectrometer, J. Geophys. Res., 112, E05007, doi:10.1029/2006JE002798.

Patterson, W.R., III, F.O. Huck, S.D. Wall, and M.R. Wolf (1977), Calibration and Performance of the Viking Lander Camera, J. Geophys. Res., 82, 28, 4391-4400, doi:10.1029/JS082i028p04391.

Pollack, J.B., D.C. Colburn, R. Kahn, J. Hunter, W. Van Camp, C.E. Carlston, M.R. Wolf (1977), Properties of Aerosols in the Martian Atmosphere, as Inferred from Viking Lander Imaging Data. *J. Geophys. Res., 82*, 28, doi:10.1029/JS082i028p044779.

Pollack, J.B., D.C. Colburn, F.M. Flaser, R. Kahn, C.E. Carlson and D. Pidek (1979), Properties and effects of dust particles suspended in the Martian atmosphere. *J. Geophys. Res., 84*, B6, doi:1029/JB084iB06p02929.

Pollack, J.B., M.E. Ockert-Bell and M.K. Shepard (1995), Viking Lander Image Analysis of Martian Atmospheric Dust, *J. Geophys. Res., 100*, 5235-5250.

Pondrelli, M., A. Pio Rossi, L. Marinandeli, E. Hauber, K. Gwinner, A. Baliva, and S. Di Lorenzo (2008), Evolution and depositional environments of the Eberswalde fan delta, Mars, Icarus, 197, 2, 429-451.

Poulet, F., J-P., Bibring, J.F. Mustard, A. Gendrin, N. Mangold, Y. Langevin, R.E. Arvidson, B. Gondet, and C. Gomez (2005), Phyllosilicates on Mars and implications for early martian climate, *Nature, 438*, 623-627.

Presley, M.A. and P.R. Christensen (1997), Thermal conductivity measurements of particulate materials, 2 Results. J. Geophys. Res., 102, 6551-6566.

Putzig, N.E., M.T. Mellon, K.A. Kretke, R.E. Arvidson (2005), Global thermal inertia and surface properties of Mars from the MGS mapping mission, Icarus, 173, 325-341.

Rafkin, S., B. Haberle, and T. Michaels (2001), The Mars regional atmospheric modeling system: Model description and selected simulations, *Icarus, 151*, 228-256.

Rafkin, S. C. R., and T. I. Michaels, Meteorological predictions for 2003 Mars Exploration Rover high-priority landing sites (2003), J. Geophys. Res., 108, E12,

8091, doi:10.1029/2002JE002027

Rafkin and Rothchild (2011)

Rennó, N.O and A.P. Ingersoll. (1996), Natural convection as a heat engine: a theory for CAPE, *J. of Atmos. Sci., 53*, 4, 572-585.

Rennó, N.O., M.L. Burkett and M.P. Larkin (1998), A simple thermodynamical theory for dust devils, *J. Atmos. Sci., 55*, 3244-3252.

Rennó, N.O., A.A. Nash, J. Lunine and J. Murphy (2000), Martian and terrestrial dust devils: Test of a scaling theory using Pathfinder data, *J. Geophys. Res., 105*, E1, 1859-1865.

Rennó, N.O., V.J. Abreu, J. Kosh, P.H. Smith, O.K. Hartogensis, H.A.R. De Bruin, D. Burose, G.T. Delory, W.M. Farrell, C.J. Watts, J. Garatuza, M. Parker, and A. Carswell (2004), MATADOR 2002: A pilot field experiment on convective plumes and dust devils, *J. Geophys. Res., 109*, doi:10.1029/2003JE002219.

Rieder, R., R. Gellert, J. Bruckner, G. Klingelhofer, G. Dreibus, A. Yen, and S. W. Squyres (2003), The new Athena alpha particle X-ray spectrometer for the Mars Exploration Rovers, *J. Geophys. Res., 108*, E12, 8066, doi:10.1029/2003JE002150

Rieder, R., R. Gellert, R.C. Arvidson, J. Bruckner, B.C. Clark, G. Dreibus, T. Economou, G. Klingelhofer, G.W. Lugmair, D.W. Ming, S.W. Squyres, C. d'Uston, H. Wanke, A. Yen, and J. Zipfel (2004), Chemistry of Rocks and Soil at Meridiani Planum from the Alpha Particle X-ray Spectrometer, *Science, 306*, 5702, 1746-1749.

Ringrose, T.J., M.C. Towner and J.C. Zarnecki (2003), Convective vortices on Mars: a reanalysis of Viking Lander 2 meteorological data, sols 1-60, *Icarus, 163*, 78-87.

Rogers, A.D. and J.L. Bandfield (2009), Mineralogical characterization of Mars Science laboratory candidate landing sites from THEMIS and TES data, *Icarus, 203*, 2, 437-453.

Ruff, S.W. and P.R. Christensen (2002), Bright and dark regions on Mars: Particle size and mineralogical characteristics based on Thermal Emission Spectrometer data, J. Geophys. Res., 107, E12, 5127, doi: 10.1029/2001JE001580.

Ryan J.A. (1964), Notes on the Martian yellow clouds, *J. Geophys. Res*. 69, 3759-3770.

Ryan, J.A. and J.J. Carroll (1970), Dust devil wind velocities: Mature state, *J. Geophys. Res., 75*, 3, 531-541.

Ryan, J.A. and R.M. Henry (1979), Mars Atmospheric Phenomena during major dust storms, as measured at the surface, *J. Geophys. Res., 84*, B6, 2821-2829, doi:10.1029/JB084iB06p02821.

Ryan, J.A. and R.D. Lucich (1983), Possible dust devils, vortices on Mars, *J. Geophys. Res., 88*, C15, 11,005-11,011.

Sagan, C., O.B. Toon, and P.J. Gierasch (1973), Climatic change on Mars, *Science, 181*, 4104, 1045-1049

Sagan, C., D. Pieri, P. Fox, R.E. Arvidson, and E.A. Guinness (1977) Particle motion on Mars inferred from the Viking Lander Cameras, *J. Geophys. Res., 82*, 28, 4430-4438, doi:10.1029/JS082i028p04430.

Schofield, J.T., J.R. Barnes, D. Crisp, R.M. Haberle, S. Larsen, J.A. Magalhães, J.R. Murphy, A. Seiff, and G. Wilson (1997), *Science 278*, 5344, 1752-1758.

Schultz, P. H., R. A. Schultz, and J. Rogers (1982), The Structure and Evolution of Ancient Impact Basins on Mars, *J. Geophys. Res.*, 87(B12), 9803–9820, doi:10.1029/JB087iB12p09803

Scott, D.H. and K.L. Tanaka (1986), Geologic map of the western equatorial region of Mars, NASA USGS

Seiff, A., J.E. Tillman, J.R. Murphy, J.T. Schofield, D. Crisp, J.R. Barnes, C. LaBaw, C. Mahoney, J.D. Mihalow, G.R. Wilson, and R. Haberle (1997), The atmosphere structure and meteorology instrument on the Mars Pathfinder lander, *J. Geophys. Res. 102*, E2, 4045-4056.

Sinclair, P.C. (1964), Some preliminary dust devil measurements, *Mon. Weather. Rev*. 92, 363-367.

Sinclair, P.C. (1966), General characteristics of dust devils, Ph.D. thesis, Univ. of Ariz., Tucson.

Sinclair, P.C. (1969), General characteristics of dust devils, *J. Appl. Meteorol., 8*, 32-45.

Sinclair, P.C. (1973), The lower structure of dust devils, *J. Atmos. Sci., 30*, 1599-1619.

Sinton, W.M. (1959), Further evidence of vegetation on Mars. *Lowell Obs. Bulletin, 103*, 4, 252-258.

Slipher, E.C. (1938), The planets from observations at the Lowell Observatory. *Proc. Amer. Philos. Soc., 79*, No. 3.

Smith, M.D., M.J. Wolff, N. Spanovich, A. Ghosh, D. Bandfield, P.R. Christensen, G.A. Landis, and S.W. Squyres (2006), One Martian year of atmospheric observations using MER Mini-TES, *J. Geophys. Res., 111*, E12S13, doi:10.1029/2006JE002770.

Smith, P.H., J.F. Bell, III, N.T. Bridges, D.T. Britt, L. Gaddis, R. Greeley, H.U. Keller, K.E. Herkenhoff, R. Jaumann, J.R. Johnson, R.L. Kirk, M. Lemmon, J.N. Maki, M.C. Malin, S.L. Murchie, J. Oberst, T.J. Parker, R.J. Reid, R. Sablotny, L.A. Soderblom, C. Stoker, R. Sullivan, N. Thomas, M.G. Tomasko, W. Ward, and E. Wegryn (1997), Results from the Mars Pathfinder camera, *Science, 278*, 1758-1765.

Smith, P.H., R. Reynolds, J. Weinberg, T. Friedman, M.T. Lemmon, R. Tanner, R.J. Reid, R.L. Marcialis, B.J. Bos, and C. Oquest (2001), The MVACS Surface Stereo Imager on Mars Polar Lander, J. Geophys. Res. 106, E8, 17,589-17,607

Smith P.H., L. Tamppari, R.E. Arvidson, D. Bass, D. Blaney, W. Boynton, A. Carswell, D. Catling, B. Clark, T. Duck, E. DeJong, D. Fisher, W. Goetz, P. Gunnlaugsson, M. Hecht, V. Hipkin, J. Hoffman, S. Hviid, H. Keller, S. Kounaves, C.F. Lange, M. Lemmon, M. Madsen, M. Malin, W. Markiewicz, J. Marshall, C. McKay, M. Mellon, D. Michelangeli, D. Ming, R. Morris, N. renno, W.T. Pike, U. Staufer, C. Stoker, P. Taylor, J. Whiteway, S. Young, and A. Zent (2008), Introduction to special section on the Phoenix Mission: Landing site characterization experiments, mission overviews, and expected science, *J. Geophys. Res., 113*, E00A18, doi:10/1029/2008JE003083.

Smith, P.H. et al. (2009), H_2O at the Phoenix Landing Site, *Science, 325*, 5936, 58-61.

Snow J.T. and T.M. McClelland (1990), Dust devils at White Sands Missile Range, New Mexico: 1. Temporal and spatial distributions, *J. Geophys. Res., 95*, 13,707-13,721.

Soffen, G.A. (1977), The Viking Project, *J. Geophys. Res., 82*, 28, 3959-3970, doi;10.1029/JS082i028p0359.

Squyres, S.W., R.E. Arvidson, E.T. Baumgartner, J.F. Bell, III, P.R. Christensen, S. Gorevan, K.E. Herkenhoff, G. Klingelhöfer, M.B. Madsen, R.V. Morris, R. Rieder, and R.A. Romero (2003), Athena Mars rover science investigation, J. Geophys. Res., 108, E12, 8062, doi:10.1029/2003JE002121.

Stanzel, C., M. Patzoid, R. Greeley, E. Hauber and G. Neukum (2006), Dust devils on Mars observed by the High Resolution Stereo Camera, *Geophys. Res. Lett., 33,* L11202, doi:10.1029/2006GL025816.

Stanzel, C., M. Patzoid, D.A. Williams, P.L. Whelley, R. Greeley, G. Neukum and the HRSC Co-Investigator Team (2008), Dust devil speeds, directions of motion and general characteristics observed by the Mars Express High Resolution Stereo Camera, *Icarus*, *197*, 1, 39-51.

Sullivan, R., R. Greeley, M. Kraft, G. Wilson, M. Golombek, K. Herkenhoff, J. Murphy, and P. Smith (2000), Results of the Imager for Mars Pathfinder windsock experiment, *J. Geophys. Res.*, 105(E10), 24,547–24,562, doi:10.1029/1999JE001234

Sullivan R., D. Bandfield, J.F. Bell III, W. Calvin, D. Fike, M. Golombek, R. Greeley, J. Grotzinger, K. Herkenhoff, D. Jerolmack, M. Malin, D. Ming, L.A. Soderblom, S.W. Squyres, S. Thompson, W.A. Watters, C.M. Weitz, and A. Yen (2005), Aeolian processes at the Mars Exploration Rover Meridiani Planum landing site, *Nature, 436*, 58-61.

Sullivan, R. et al. (2008), Wind-driven particle mobility on Mars: Insights from Mars Exploration Rover observations at “El Dorado” and surroundings at Gusev Crater, *J. Geophys. Res*., *113*, E06S07, doi:10.1029/2008JE003101.

Tamppari, L.K., M.D. Smith, D.S. Bass, and A.S. Hale (2008), Water-ice cluds and dust in the north polar region of Mars using MGS TES data, *Plan. and Space Sci., 56*, 2, 227-245.

Taylor, P.A., D.C. Catling, M. Daly, C.S. Dickinson, H.P. Gunnlaugsson, A.-M. Harri, and C.F. Lange (2008), Temperature, pressure, and wind instrumentation in the Phoenix meteological package, *J. Geophys. Res., 113*, E00A10, doi:10.1029/2007JE003015.

Thomas, P., J. Veverka, S. Lee, and A. Bloom (1981), Classification of wind streaks on Mars, *Icarus, 45*, 124-153.

Thomas P., and P.J. Gierasch (1985), Dust devils on Mars, *Science, 236*, 175-177.

Tillman, J.E., R.M. Henry, S.L. Hess (1979), Frontal systems during passage of the Martian north polar hood over the Viking Lander 2 site prior to the first 1977 dust storm, *J. Geophys. Res., 84*, B6, 2947-2955, doi:10.1029/JB084iB06p0294.

Tillman, J.E., L. Landberg, and S.E. Larsen (1994), The boundary layer of Mars: Fluxes, stability, turbulent spectra, and growth of the mixed layer, *J. Atmos. Sci., 51*, 12, 1709-1727.

Titus, T.N. (2005), Mars polar cap edges tracked over 3 full Mars year, *36th LPSC*, March 14-18

Toigo, A.D., M.I. Richardson, S.P. Ewald, and P.J. Gierasch (2003), Numerical simulation of Martian dust devils, *J. Geophys. Res., 108*, E6, 5047, doi:10.1029/2002JE002002.

Tomasko M.C., L.R. Doose, M. Lemmon, P.H. Smith, and E. Wegryn (1999), Properties of Dust in the Martian Atmosphere from the Imager on Mars Pathfinder, *J. Geophys. Res*., *104*, 8987-9007.

Towner, M.C. (2009), Charateristics of large Martian dust devils using Mars Odyssey Thermal Emission Imaging System visual and infrared images, *J. Geophys. Res., 114*, E02010, doi:10.1029/2008JE003220.

Tyler, D., Jr., J.R. Barnes, and R.M. Haberle (2002), Simulation of surface meteorology a the Pathfinder and VL1 sites using a Mars mesoscale model, *J. Geophys. Res., 107*, E4, 5018, doi:10.1029/2001JE001618.

Verba, C.A., P.E. Geissler, T.N. Titus, D. Waller (2010), Observations from the High Resolution Imaging Science Experiment (HiRISE): Martian dust devils in Gusev and Russell craters, *J. Geophys. Res*. *115*, E09002, doi:10.1029/2009JE003498.

Ward, A.W., L.R. Gaddis, R.L. Kirk, L.A. Soderblom, K.L. Tanaka, M.P. Golombek, T.J. Parker, R. Greeley, and R.O. Kuzmin (1999), General geology and geomorphology of the Mars Pathfinder landing site, *J. Geophys. Res., 104*, E4, 8555-8571, doi:10.1029/1998JE900021.

Whelley, P.L. and R. Greeley (2008), The distribution of dust devil activity on Mars. *J. Geophys. Res., 113*, E07002, doi:10.1029/2007JE002966.

White, B.R., B.M. Lacchia, R. Greeley, and R.N. Leach (1997), Aeolian behavior of dust in a simulated Martian environment, *J. Geophys. Res., 102*, E11, 25,629-25,640, doi:10.1029/97JE01753.

Whiteway, J., M. Daly, A. Carswell, T. Duck, C. Dickinson, L. Komguem, and C. Cook (2008), Lidar on the Phoenix mission to Mars, *J. Geophys. Res. 113*, E00A08, doi:10.1029/2007JE003002.

Wolff M.J., M.D. Smith, R.T. Clancy, N. Spanovich, B.A. Whitney, M.T. Lemmon, J.L. Bandfield, D. Bandfield, A Ghosh, G. Landis, P.R. Christensen, J.F. Bell III and S.W. Squyres (2006), Constraints on dust aerosols from the Mars Exploration Rovers using MGS overflights and Mini-TES. *J. Geophys. Res*., *111*, E12S17, doi:10.1029/2006JE002786.

Zent, A.P., M.H. Hecht, C.R. Cobos, S.E. Wood, T.L. Hudsen, S.M. Milkovich, L.P. DeFlores, and M.T. Mellon (2010), Initial results from the thermal and electrical conductivity probe (TECP) on Phoenix, *J. Geophys. Res*., *115*, E00E14, doi: 10.1029/2009JE003420.

Zuber, M.T., D.E. smith, S.C. Soloman, D.O. Muhleman, J.W. Head, J.B. Garvin, J.B. Abshire, and J.L. Bufton (1992), The Mars Observer Laser Altimeter Investigation, *J. Geophys. Res., 97*, E5, 7781-7797, doi:10.1029/92JE00341.